Correcting the rotation curve of spiral galaxies for the non-circular motions induced by a bar

Toky Herimandimby RANDRIAMAMPANDRY

Student number: RNDTOK001

A thesis submitted to the University of Cape Town
in fulfillment of the requirements
for the degree of Doctor of Philosophy

in the

Faculty of Science
University of Cape Town

Supervisor:
Prof. Claude CARIGNAN

Date of Submission: June 2017

Department of Astronomy

Declaration of Authorship

The work presented in this thesis is partly based on collaborations with my supervisor Claude Carignan together with Nathan Deg, Francoise Combes and Kristine Spekkens. This thesis contains research that has already been published:

1. Chapter III (Paper I) entitled " Estimating non-circular motions in barred galaxies using numerical N-body simulations " have been published in the Monthly Notices of the Royal Astronomical Society Journal; Randriamampandry, T. H., Combes, F., Carignan, C. and Deg, N. MNRAS, Volume 454, Issue 4, p.3743-3759 (2015).

   In this peer-reviewed publication, we show the effect of the non-circular motions on the mass models of galaxies inferred from neutral hydrogen rotation curves. My contribution to this work includes the analysis and reduction of the data and the simulation, the writing of the text and the discussions.

2. Chapter IV (paper II) entitled " Exploring the GalMer database: bar properties and non-circular motions " has been published in Astronomy & Astrophysics, Randriamampandry T. H., Deg N., Carignan C., Combes F. and Spekkens K., Astronomy & Astrophysics, Volume 594, id.A86, 10 pp (2016).

   This chapter is a continuation of chapter III but in a more elaborate manner. We used all the galaxy types from the GalMer database (Chilingarian et al. 2010).

3. Chapter IV (paper III) is entitled " Simulating non-axisymmetric flows in disc galaxies ". The paper version of this chapter is submitted to the Monthly Notices of the Royal Astronomical Society Journal, T. H. Randriamampandry, N. Deg, C. Carignan and L. Widrow, MNRAS, submitted

   In this chapter, we perform new simulations of strongly barred galaxies and compared the results with observations.

I, Toky Herimandimby RANDRIAMAMPANDRY, hereby declares that this thesis entitled, " Correcting the rotation curve of spiral galaxies for the non-circular motions induced by a bar" and the work presented in it are my original work (except where acknowledgements indicate otherwise) and that neither the whole work nor any part of it has been, is being, or is to be submitted for another degree in this or any other university.

I empower the university to reproduce for the purpose of research either the whole or any portion of the contents in any manner whatsoever.

Signed: _____

Date: _____

"If you can't fly then run, if you can't run then walk, if you can't walk then crawl, but whatever you do you have to keep moving forward."

Martin Luther King, Jr.

Name: Toky Randriamampandry
Student number: RNDTOK001
Supervisor: Prof. Claude Carignan

Title: Correcting the rotation curve of spiral galaxies for the non-circular motions induced by a bar

Abstract

The mass distribution of disk galaxies is usually determined through the use of rotation curves. This determination relies on two key assumptions; that the gas moves on circular orbits and that this motion traces the underlying gravitational potential. In the case of barred spiral galaxies the first assumption is false as the bar induces non-circular streaming motions in the gas. Therefore, the rotation curves of barred galaxies need to be corrected for the non-circular motions before being used for mass model analysis.

In this dissertation, we use numerical simulations to quantify and correct for the non-circular flows induced by a bar. The aim is to investigate and quantify the effect of the bar properties on the amplitude of the non-circular motions. This is done by comparing the observational data such as rotation curves and bar properties with the kinematics and bar properties obtained from mocked galaxies.

In chapter III, we examine the performance of ROTCUR and DISKFIT for deriving rotation curves from velocity maps of barred spiral galaxies using mock observations. Our results confirm that ROTCUR under-/overestimates measured rotation curves if the bar is aligned with one of the symmetry axes. The DISKFIT algorithm, which is specifically designed for barred galaxies only works for galaxies of intermediate bar orientations.

In chapter IV, we quantify the magnitude of the non-circular flows and constrain the range of bar orientation angles where DiskFit fails by using Tree-SPH simulations from the GalMer database by Chilingarian et al . (2010). We find that the rotation curve obtained from ROTCUR was 40% smaller/larger than the expected velocities calculated from the gravitational potential when the bar is aligned with the major/minor axis. For the DISKFIT analysis, we find that DiskFit produces unrealistic values for all the models when the bar is within ten degrees of the symmetry axes.

New hydrodynamic simulations of three disc galaxies (NGC 1300 , NGC 1530 and NGC 3621) are presented in chapter IV. Our objective is to create more realistic simulated galaxies that replicate the bar properties and velocity fields of the galaxies of our sample. The initial conditions for our simulations are determined through a Bayesian analysis of the azimuthally averaged rotation curve, the stellar surface brightness, and the gas surface density. The parameters posterior distribution functions (PDFs) combine with the disc stability parameters PDFs are used as criteria to select the model parameters. The velocities of the gas particles are transformed into velocity maps and compared with the observed galaxies. We are able to reproduce the bar properties and kinematics of the three galaxies in our sample. These findings imply that a tailored simulation is an effective way of investigating non-circular flows in disc galaxies especially when the bar orientation is close to the minor or major kinematical axis of the galaxy.

Acknowledgements

It is with immense gratitude that I salute the support and the favors that my supervisor Professor Claude CARIGNAN have offered me for the last 6 years. I have had the privilege to come to his office every time I was trapped in my mind. I have been given the opportunity to go abroad to deepen my knowledge yet to strengthen a collaboration with other astronomers. I have also been fortunate to be part of the KAT7 early science team from which I have acquired enormous experiences. It is without doubt that Claude's influence plays a huge role on who I am today: a proud scientist and a decent man.

I also wish to extend my thank you to the following collaborator in no particular order:

- Professor Francoise Combes at the Observatoire de Paris in France; un grand grand merci pour l'accueil chaleureux, pareil pour les étudiants ainsi que le personnel de LERMA à Paris.

- Professor Phillip Amram at the Laboratoire d' Astrophisique de Marseille (LAM); avec tous mes respects, MERCI!, my visit in Marseille back in 2015 was very pleasant and fruitful.

- Dr Kristine Spekkens at the Royal Military College of Canada (RMCC); I acknowledge the incredible value of having a chance to collaborate or just to discuss with someone who has a very busy schedule as you do.

- Dr Danielle Lucero; AIPS and other HI data reduction packages are more than familiar to me now because of you and your passion. Moreover, based on your encouragement and your sincere comments you truly are the big sister I never had.

- Dr Nathan Deg; the embodiment of hard work and awesomeness. Your work ethic and positivity is epidemic that I am roughly inspired to work harder and harder everyday.

On behalf of my parents and myself, I would like to express my gratitude to all the staff members and students at the department of astronomy for creating a jovial vibe, for inventing a place that I called home for the past six years.

I acknowledge the financial support from the SKA SARChI fellowship, the National Research Foundation (NRF) of South Africa and the Postgraduate Funding Office at UCT. I would also like to acknowledge the Center for High Performance Computing (CHPC) and its staff, in particular Dr. Sean February and Prof. Catherine Cress for allowing us to use this facility under the program ASTR0858.

Finally, to my dearest friend, the love of my life, thank you for everything.

...

Contents

List of Figures

List of Tables

Dedicated to My Family and Friends

Chapter 1

Introduction

Galaxies are the building blocks of the large scale structure in the universe. They are composed of stars, gas, dust and a large amount of unseen "dark matter". Unfortunately, dark matter does not interact with ordinary matter and its presence is only known by its gravitational effect on ordinary matter (eg. Zwicky 1933; Freeman 1970). The rotation curves of most spiral galaxies stay flat up to large radii (Bosma 1978), which implies a large amount of unseen matter. The amount of dark matter in galaxies is inferred by the difference between the observed rotation curve due to the dynamical mass and the contribution from the visible mass (eg de Blok et al. 2008). For more than four decades, astronomers have been deriving rotation curves of spiral galaxies and using them to study their mass distribution, and, more importantly, the parameters of their dark halo component (Carignan 1983; Carignan & Freeman 1985). The assumption underlying this type of work is that the rotation velocities trace the gravitational potential of both the luminous and dark parts of the galaxy. While we can make this assumption for normal, unbarred, isolated spiral galaxies, this is surely not the case for barred galaxies since the measured velocities are a combination of the signatures of the gravitational potential and of the streaming motions of the gas along the bars. Accurate modeling has shown that the estimated mass of barred spiral galaxies may be wrong

by up to 20% depending on the strength of the bar and of its orientation relative to the major axis of the galaxy (e.g. Dicaire et al. 2008). It is very important to tackle this problem since more than two-thirds of spiral galaxies are barred (eg. de Vaucouleurs et al. 1991; Masters et al. 2011).

Non-circular motions cause dynamical perturbations and limit the usefulness of the observed rotation curves. Rotation curves are usually derived from two-dimensional velocity maps that contain information about both the circular velocities and the non-circular flows. Several techniques have been proposed in the literature to correct for non-circular motions in galaxies. As an example, Weiner et al. (2001) used fluid dynamic models of the gas flow (see also section 2.5.2 and 2.5.3). They combined information from the distribution of light and the velocity field to constrain the dynamical properties of the disk. However, this method is complex and computationally expensive.

The main objective of this dissertation is to correct the rotation curve of barred galaxies for these non-circular motions before using them for mass model analysis. We propose to use results from numerical simulations to estimate and correct for the non-circular flows. The dissertation is organized as follows. Theoretical background and a literature review are given in Chapter 2. In chapter 3 we use mock galaxies obtained from numerical simulations to test the current tools that are used to derive galaxies' rotation curves. We also correct the observed rotation curve of NGC 3319 and perform a mass model analysis using the corrected and uncorrected rotation curves to show the importance of such corrections if we want to derive accurately the masses of barred spiral galaxies. In Chapter 4, we use hydrodynamic simulations from the GalMer database to investigate the correlation between the properties of the bar and the amplitude of the non-circular flows. New simulations of strongly barred galaxies are presented in chapter 5. We reproduce the properties of the galaxies in the sample and compare the simulated galaxies with observational data. Finally, a general summary and future prospects are given in chapter 6.

Bibliography

Bosma, A. 1978, Ph.D. Thesis, Rijksuniversiteit, Groningen, The Netherlands.

Carignan, C., 1983, Ph.D. Thesis, Australian National University, Canberra, Australia

Carignan, C., & Freeman, K. C. 1985, ApJ, 294, 494

de Blok, W. J. G., Walter, F., Brinks, E., et al. 2008, AJ, 136, 2648-2719

de Vaucouleurs G., de Vaucouleurs A., Corwin, Jr. H. G., Buta R. J., Paturel G., Fouqué P., 1991, Third Reference Catalogue of Bright Galaxies. Volume I: Explanations and references. Volume II: Data for galaxies between 0^h and 12^h. Volume III: Data for galaxies between 12^h and 24^h.

Dicaire, I., Carignan, C., Amram, P., et al. 2008, MNRAS, 385, 553

Freeman, K. C. 1970, ApJ, 160, 811

Masters, K. L., Nichol, R. C., Hoyle, B., et al. 2011, MNRAS, 411, 2026

Weiner, B. J., Sellwood, J. A., & Williams, T. B. 2001, ApJ, 546, 931

Zwicky, F. 1933, Helvetica Physica Acta, 6, 110

Chapter 2

Background and literature review

2.1 Classification of galaxies

Galaxies exhibit a broad range of morphological types and physical properties. Therefore, a classification scheme is needed to study these objects. The most widely used classification scheme is the one proposed by Hubble (1936), which classifies galaxies into four major classes: elliptical, spiral, lenticular and irregular. A revised version of the Hubble classification scheme is presented in figure 2.1.

- A spiral galaxy consists of a flat disk with spiral arms and a central concentration of stars known as the bulge. They are further subdivided into Sa (prominent central bulge, closed spiral arms), Sb, Sc, Sd (prominent disk, more open spiral arms) and Sm (for Magellanic type).

  About two-third of spiral galaxies also host a bar-shaped stellar structure in addition to the spiral arms (see de Vaucouleurs et al. 1991). The spiral arms inhabit ongoing star formation activities that make the arms look brighter than the rest of the disk.

- An elliptical galaxy is a smooth and almost featureless object. It does not host an obvious disc or a spiral arm. Ellipticals are generally gas poor and

have small or no star formation activities. They are generally dominated by an old stellar population. The sizes of elliptical galaxies vary from a few kpc to hundreds of kpc, and their masses range from 10^7 to 10^{13} solar masses. Ellipticals are generally found in a dense environment particularly in clusters of galaxies. They are sub-classified into E1 through 7 according to their apparent ellipticity,

$$\epsilon = 1 - \frac{b}{a},$$

where b and a are the minor and major axis of the ellipse respectively.

- Lenticular galaxies are located at the center of the Hubble tuning fork diagram. Lenticular galaxies have a disk without spiral arms, a central bulge and often a bar.

- Irregular galaxies are apparently disorganized and asymmetrically shaped. The stars and gas move randomly with slower rotation than spiral galaxies. Also, irregular galaxies contain a large amount of gas and have a large star formation rate.

2.2 Barred spiral galaxies

Barred spiral galaxies host a central bar in addition to the spiral arms and bulge. They are located at the lower right part of spirals on the Hubble tuning fork diagram (see Figure 2.1). Nearly two-thirds of spiral galaxies have a bar-like structure in their center; one third are strongly barred and one third weakly barred (see eg. de Vaucouleurs et al. 1991; Eskridge et al. 2000). Figure 2.2 shows an optical image of the grand design barred galaxy NGC 1300 with a prominent stellar bar and spiral arm structure. The fraction of barred galaxies is much higher in the near-infrared band compared to the optical because of the absence of obscuration by dust (see Menéndez-Delmestre et al. 2007; Sheth et al. 2010).

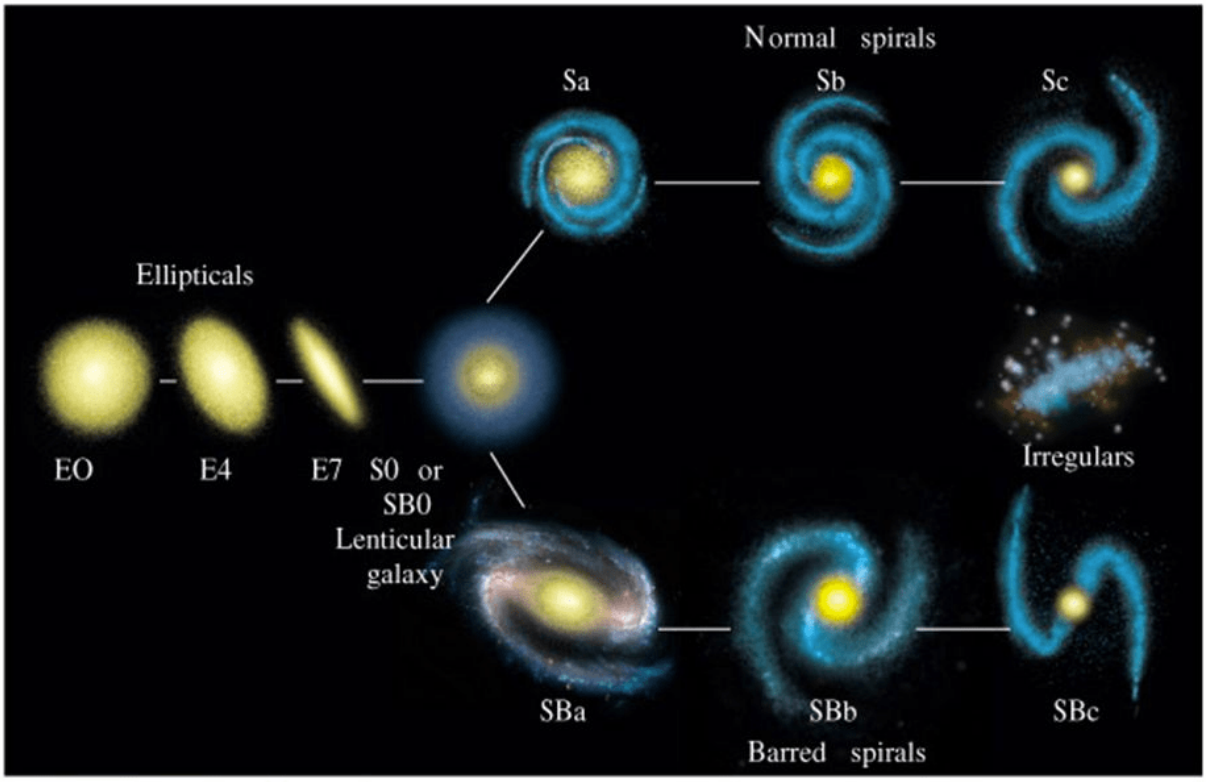

FIGURE 2.1: The Hubble tuning fork diagram showing the four main classes: elliptical on the left, lenticular on the middle, spiral and irregulars on the right (credit: NASA/ESA).

FIGURE 2.2: Grand design barred galaxy NGC 1300 (credit: NASA/ESA).

FIGURE 2.3: Composite HST image (top) and 2MASS JHK image (bottom) of NGC 253 (credit: HST/2MASS).

Figure 2.3 compares a combined JHK image from Jarrett et al. (2003) and an optical HST composite image of NGC 253. This figure clearly shows that the bar is better resolved in the near-infrared image than in the optical image. Bars also play an important role in a galaxy's dynamic evolution; they fuel star formation activity by channeling the gas from the disk towards the center and transfer angular momentum throughout the disk (Lynden-Bell & Kalnajs 1972; Weinberg 1985; Athanassoula & Misiriotis 2002; Marinova & Jogee 2007). The presence of the bar forces the gas to deviate from circular flows, which complicates the dynamical studies of barred galaxies(see Sellwood & Wilkinson 1993 for a review).

2.3 Mass discrepancies

The dynamical mass of galaxies and other gravitationally bound systems inferred from their rotation velocities are found to be much larger than the observed luminous mass (Zwicky 1933, 1937). This is known as the mass discrepancy or the missing mass problem. F. Zwicky was among the first to point out that the gravitational mass inferred using the virial theorem was larger than the luminous mass in the Coma cluster, implying the presence of a large undetected mass. Babcock (1939) found a few years later that a very large mass-to-light ratio is required to explain the dynamical mass of M31 which was also reported by Oort (1940) for NGC 3115 and NGC 4494. These findings were later confirmed by other authors (Schwarzschild 1954; de Vaucouleurs 1959; Rubin & Ford 1970; Freeman 1970). Bosma (1978) also found that almost all the spiral galaxies in his sample have flat rotation curves. The more recent analysis by de Blok et al. (2008) shows that most of the spiral galaxies selected from The HI Nearby Galaxies Survey (THINGS, Walter et al. 2008) have flat rotation curves.

The missing mass problem of spiral galaxies is commonly explained by the presence of a dark matter halo (eg. Carignan 1985; Carignan & Freeman 1985). The dark matter component is obtained by comparing the observed rotation curve with the

quadratic sum of the contributions from the luminous mass (e.g. de Blok et al. 2008). The observed rotation curve is decomposed into,

$$V_{rot}^2 = V_{gas}^2 + V_*^2 + V_{halo}^2, \tag{2.1}$$

where V_{gas} is the contribution from the gas, V_* from the stars and V_{halo} from the dark matter halo component. The stellar contribution is obtained by converting the luminosity profile into density profile through a mass-to-light ratio (eg., de Blok et al. 2008). On the other hand, the gas contribution is obtained from the density profile of the HI neutral hydrogen gas and corrected for the Helium contribution.

The dark matter halo contribution is often described by a theoretical or experimental density profile. Several dark matter density profiles are proposed in the literature. The two most commonly used are the isothermal profile (ISO) (eg. Carignan 1985; Carignan & Freeman 1985; Begeman 1987) and the Navarro Frenk and White (NFW) profile (Navarro et al. 1996). The ISO density profile is defined as

$$\rho_{ISO}(R) = \frac{\rho_0}{1 + (\frac{R}{R_c})^2} \tag{2.2}$$

where ρ_0 is the central density and R_c is the core radius of the halo.

The NFW DM halo profile was derived from cosmological simulations and is commonly accepted in the ΛCDM framework. The NFW halo density profile is described by:

$$\rho_{NFW}(R) = \frac{\rho_i}{\frac{R}{R_S}(1 + \frac{R}{R_S})^2} \tag{2.3}$$

where $\rho_i \approx 3H_0^2/(8\pi G)$ is the critical density for closure of the universe and R_S is the halo scale radius. The Einasto profile has also been proposed to model the distribution of dark matter halo in galaxies as an alternative to the NFW profile

(Hayashi et al. 2004). The Einesto profile is given as (Einasto 1965):

$$\rho(\mathrm{r}) = \rho_{-2} \exp\left(-2\mathrm{n}[(\frac{\mathrm{r}}{\mathrm{r}_{-2}} - 1)]\right) , \tag{2.4}$$

where r_{-2} and ρ_{-2} are the radius and density at which $\rho(\mathrm{r}) = \mathrm{r}^{-2}$. Chemin et al. (2011) found that the Einasto profile provides much better fits to the rotation curves of seventeen galaxies from the THINGS sample than the ISO or NFW profiles.

The broader family of density profiles by Zhao (1996) and Kravtsov et al. (1998) has also been used in the literature (e.g., Blais-Ouellette et al. 2001). This density profile has a double-power law with three additional parameter (α, β, γ). The density profile is defined as

$$\rho(\mathrm{r}) = \frac{\rho_0}{(\mathrm{r}/\mathrm{r}_\mathrm{o})^\gamma [1 + (\mathrm{r}/\mathrm{r}_0)^\alpha]^{(\beta-\gamma)/\alpha}}, \tag{2.5}$$

where ρ_0 is the central density and r_0 is the scale radius. The slope of the density profile is defined by the parameters α, β and γ (see also Blais-Ouellette et al. 2001).

The Modified Newtonian Dynamics proposed by Milgrom (1983) is an alternative explanation for the missing mass problem. MOND stipulates that there is no need for dark matter if the Newton's laws of gravity are modified below a critical acceleration threshold a_0. Sanders & McGaugh (2002) gives an extensive review on MOND.

2.4 Rotation curves

Rotation curves are either measured from long slit spectra or from two dimensional velocity fields. For long slit data the observed line-of-sight velocities are interpreted

as

$$V_{obs} = V_{sys} + V_c \sin(i) \ , \tag{2.6}$$

where i is the inclination angle of the disk, v_{sys} is the systemic velocity and V_c is the circular velocity. However, this technique does not give any information about the non-circular motions. A two dimensional velocity field provides information about the circular and non-circular components. A 2D velocity map is usually obtained from Fabry-Perot observations of the H_α emission lines in the optical bands (e.g., Epinat et al. 2008) or from interferometric observations of the 21 cm Hydrogen line (e.g., Walter et al. 2008).

A velocity field is a map representing the mid-plane recession velocity of the disk (Begeman 1987; Józsa 2007). A list of the methods used to construct velocity field of galaxies are given in de Blok et al. (2008). The commonly used method is the intensity-weighted velocity or first moment map. It involves taking the first moment or intensity-weighted mean along the velocity axis of the data cube. This method has several disadvantages despite being straightforward. For example, the velocities are biased towards the longest tail of the velocity profile if the velocity distribution is asymmetric and the channels affected by noise could largely affect the resulting velocity maps if not avoided Carignan et al. 1990; de Blok et al. 2008. According to de Blok et al. (2008), simple and multiple Gaussian profile fitting provides better results than the standard intensity-weighted method. This method consists of fitting Gaussian functions to the velocity profile, and is less affected by noise and systematic effects than the intensity-weighted velocity method.

2.5 Determining rotation curves from velocity maps

The velocity of a particular point in the plane of the disk can be expressed as a Fourier expansion of the radial, V_r, and tangential, V_t, components. These

components are defined as,

$$V_r(r,\theta) = \overline{V_r}(r) + \sum_{m=1}^{\infty} V_{m,r}(r)\cos[m\theta + \theta_{m,r}(r)] \ , \tag{2.7}$$

$$V_t(r,\theta) = \overline{V_t}(r) + \sum_{m=1}^{\infty} V_{m,t}(r)\cos[m\theta + \theta_{m,t}(r)] \ , \tag{2.8}$$

where $V_{m,t}(r)$ and $V_{m,r}(r)$ are the tangential and radial Fourier mth velocity moments respectively and θ, $\theta_{m,t}(r)$ and $\theta_{m,r}(r)$ are the angular phases. On the other hand, the observed line of sight velocity is the combination of the projected azimuthal and radial velocities

$$V_{obs} = V_{sys} + \sin(i)(V_t\cos\theta + V_r\sin\theta) \tag{2.9}$$

where V_{sys} is the systemic velocity, i is the inclination angle and V_t and V_r are the tangential and radial components given by Equation 2.7 and 2.8 respectively.

2.5.1 The tilted ring method

The tilted ring method was first used by Rogstad et al. (1974) to model the warped disk of M83. This method divides the velocity maps into concentric rings and derives the rotation velocities and other parameters for each ring. It has been implemented in the GIPSY task ROTCUR (Begeman 1989). The tilted-ring technique fits the following function to the velocity field

$$V_{obs} = V_{sys} + V_C\sin i\cos\theta + V_R\sin i\cos\theta, \tag{2.10}$$

where V_{sys}, V_C and V_R are the systemic velocity, the circular velocity and the radial velocity respectively; i and θ are the inclination angle and the azimuthal angle in the plane of the galaxy.

The azimuthal angle is related to the position angle (Φ), the kinematic center (x_c, y_c) and the inclination angle by:

$$\cos(\theta) = \frac{-(x - x_c)\sin(\Phi) + (y - y_c)\cos(\Phi)}{R} \tag{2.11}$$

$$\sin(\theta) = \frac{-(x - x_c)\cos(\Phi) + (y - y_c)\sin(\Phi)}{R\cos(i)} \tag{2.12}$$

The tilted ring method assumes axi-symmetry and does not correct for non-circular motions. Therefore it is not suitable for galaxies with large scale non-circular flows. On the other hand, it is efficient for modeling warp disks since the position angle and inclination can be left free to vary for each ring (Begeman 1987).

Software packages such as TIRIFIC (Józsa et al. 2007) and BAROLO (Di Teodoro & Fraternali 2015) apply the tilted ring method to velocity cubes instead of velocity fields. These packages create model cubes and apply the tilted ring technique to the velocity maps derived from the modeled cubes.

2.5.2 Harmonic decomposition

The harmonic decomposition method decomposes the line-of-sight velocities as a series of cosine and sine terms (Schoenmakers et al. 1997; Schoenmakers 1999). It uses epicycle theory to derive the harmonic terms of a mildly distorted potential. This method has been implemented in the GIPSY task RESWRI. This task performs harmonic expansion of the radial velocity along each ring and estimates the non-circular motions using the higher harmonic terms.

Following Schoenmakers (1999) , the line of sight velocity is defined as

$$V_{los} = V_{sys} + \sin(i) \sum_{m=1}^{N} C_m \cos\ m\psi + S_m \sin\ m\psi\ , \tag{2.13}$$

where N is the order of the harmonic term, C_m and S_m are the amplitudes of the harmonic terms, V_{sys} is the C_0, S_0 is the radial expansion velocity and ψ is the phase. The non-circular motion components are given by the higher harmonics terms.

Schoenmakers et al. (1997) noticed that expansion up to N=3 is enough to describe the perturbations in the velocity field. The amplitude of the non-circular motion is given by

$$A(r) = \sqrt{S_1^2 + C_2^2 + S_2^2 + S_3^2 + C_3^2}\ . \tag{2.14}$$

For a purely circular motion, the line-of-sight velocity is given by the m=0 and m=1 terms,

$$V_{los} = V_{sys} + \sin(i)(C_0 \cos\ \psi + S_0 \sin\ \psi)\ , \tag{2.15}$$

where C_0 is the circular rotation velocity and S_0 is the expansion velocity.

Trachternach et al. (2008) applied the harmonic decomposition on the velocity field of 19 galaxies selected from the THINGS sample (Walter et al. 2008) to quantify the systematic non-circular motions in these galaxies. They reported an average non-circular motions of 6.7 km s^{-1} for the galaxies in their sample. They also noticed that fixing the kinematic centers did not affect the results. Oh et al. (2008) also found similar results when modeling non-circular motions of dwarf galaxies, also from THINGS, by comparing the rotation curve derived using the bulk flow velocity field with the rotation curve derived from intensity-weighted velocity maps.

Sellwood & Sánchez (2010)) listed the limitations of the harmonic decomposition technique. This method assumes a small departure from circular flows. The derived Fourier coefficients are not easy to interpret backwards in terms of physical models (Wong et al. 2004). Several studies have shown that the magnitude of the non-circular motions rival the circular velocity component in some cases (e.g. Swaters et al. 2003).

2.5.3 The DiskFit algorithm

Spekkens & Sellwood (2007) introduced a new technique that models the radial and tangential components of the velocity of a particle at a given position in the plane of the disk. They assume that the disk is flat, and that the line of sight is the combination of axisymmetric rotation and a bi-symmetric flow in the disk plane with a fixed azimuthal phase. This technique has been embodied in the publicly available code DiskFit, which fits the observed velocity field with the following equation:

$$\begin{aligned} V_{\rm model} = V_{\rm sys} + \sin(i)[&V_{\rm t}\cos(\theta) - V_{2,\rm t}\cos(2\theta_{\rm b})\cos(\theta) \\ &-V_{2,\rm r}\sin(2\theta_{\rm b})\sin(\theta)] \end{aligned} \tag{2.16}$$

where V_t is the circular velocity, $V_{2,t}$ and $V_{2,r}$ are the amplitudes of the tangential and radial components of the noncircular motions for a bi-symmetric flow model and θ_b is the angle relative to the bar axis Spekkens & Sellwood (2007). DiskFit can also model a pure radial motion (m=0), a lopsided galaxy (m=1) or a warped disk (see `http://www.physics.rutgers.edu/~spekkens/diskfit/` for further information).

DiskFit uses the Levenberg Marquardt χ^2 minimization method to estimate the parameters for a given model:

$$\chi^2 = \sum_{n=1}^{N} \left(\frac{V_{obs}(x, y) - \sum_{k=1}^{K} \omega_{k,n} V_k}{\sigma_n} \right)^2 \tag{2.17}$$

where $V_{obs}(x,y)$ is the observed velocity at the position (x,y) on the sky, the K elements of V_k are the values of the tabulated velocity profiles in the model, σ_n is the uncertainty in the measurements, $\omega_{k,n}$ is a weighting function which includes the trigonometric factors and also defines an interpolation scheme for the projected model (Sellwood & Sánchez 2010).

The advantages of DiskFit, such as its ability to discern weak bar are listed in Sellwood & Sánchez (2010). However, recent studies have shown that DiskFit fails when the bar is within ±10 degrees of the minor or major axis (e.g., Randriamampandry et al. 2016).

2.6 Numerical simulations of barred galaxies

2.6.1 N-body and hydrodynamic simulations

Part of the advancement of modern astrophysics is largely due to numerical simulations, which is made possible because of the ever increasing computational capabilities combined with sophisticated algorithms. Simulations fill the gap between theory and observations, which help us to interpret complex systems (see Bertschinger 1998 for a review). In particular, they have largely contributed to our understanding of the dynamics and structural properties of disk galaxies (see Sellwood & Wilkinson 1993). They have also increased our understanding of galaxy formation and evolution (e.g. Athanassoula 2002). Various numerical methods exist to simulate a system that involves the interaction between large number of particles (for earlier reviews see Hockney & Eastwood (1981) and Sellwood (1987)).

Most of the numerical simulations made in the 1960s and 1970s are based on direct summation of the gravitational force (e.g. Miller et al. 1970; Quirk 1970). Later, the particle mesh algorithm was introduced in order to reduced the computation cost (Hockney & Eastwood 1981; Klypin & Shandarin 1983; Efstathiou et al. 1985; Bouchet & Hernquist 1988 and references herein). This method discretized the space into a mesh and assigns the particles to the nearest vertices of the mesh. The gravitational field is found by computing the Poisson equation using Fourier transform. However, this method is limited by the size of the mesh. A more sophisticated version of the PM algorithm has also been used in the literature (see Sellwood 1987). The tree algorithm (Appel 1985) uses a grid, which devides particles into cells and assuming the cells as particles (see also Barnes & Hut 1986). This method significantly reduces the computational cost (see Springel et al. 2001 and references therein). However, the spatial resolution is limited to the size of the cells. More realistic simulations usually include a gas component. The gas is usually described as a smoothed particle hydrodynamic (SPH), in which the gas is partitioned into fluid elements represented by particles (Lucy 1977; Gingold & Monaghan 1977; Monaghan 1992). The gas particles obey the equations of motion similar to the collisionless component, but contain additional terms describing pressure gradients, viscous forces and radiative effects in gas. The simulation code GADGET (GAlaxies with Dark matter and Gas intEracT) (Springel et al. 2001; Springel 2005) is commonly used to study a self-gravitating system or a cosmological N-body/SPH simulation. SPH is a powerful Lagrangian technique to solve hydrodynamical problems with an ease that is unmatched by grid based fluid solvers (see Monaghan 1992, for an excellent review). In particular, SPH is very well suited for three-dimensional astrophysical problems that do not crucially rely on accurately resolved shock fronts.

N-body/hydrodynamic simulations of barred galaxies have significantly improved during the last few decades (see e.g. Athanassoula et al. 2013). It is now possible to produce realistic model in which the observable properties such as bar properties

and kinematics calculated from the simulations could be directly compared with those measured from observations (e.g. Rautiainen et al. 2002, 2004; Chequers et al. 2016). Early simulations of isolated galaxies have shown that a purely self-gravitating disk is susceptible to disk instability and eventually will form a bar (e.g. Ostriker & Peebles 1973; Combes & Sanders 1981, see also Athanassoula 2002). The disk stability is quantified using the Toomre parameter Q (Toomre 1964) and the disk self gravity X (Goldreich & Tremaine 1978, 1979). The Toomre parameter Q indicates the local stability of the disk, and X quantifies whether a non-circular perturbation will grow even if the disk is stable.

The disk self gravity is

$$X = \frac{V_t^2(2.2R_d)}{V_d^2(2.2R_d)} \ . \tag{2.18}$$

where V_t and V_d are the total circular velocity and the circular velocity due to the disk respectively.

The parameter Q for the stellar disk is defined by

$$Q_d = \frac{\sigma_r \kappa}{3.36 G \Sigma_d} \ , \tag{2.19}$$

where σ_r is the radial velocity dispersion, κ is the epicyclic frequency, G is the gravitational constant and Σ_d is the stellar surface density. For the gas disk the Q is given by

$$Q_g = \frac{c_s \kappa}{\pi G \Sigma_g} \ , \tag{2.20}$$

where c_s is the sound speed of the gas and Σ_g the gas surface density (Wang et al. 2010). These two parameters are inter-dependent, therefore a galaxy with $Q \gtrsim 1$ and large $X \gtrsim 1$ will eventually form a bar in its lifetime (Spinoso et al. 2016). However, the formation of a bar could be prevented or delayed if the disk is dispersion-dominated or if the galaxy hosts a large fraction of gas (Athanassoula 2002).

2.6.2 Initial conditions

An equilibrium initial condition is necessary for a N-body or hydrodynamic simulation. Here we focus only on initial conditions that produce equilibrium models for disk galaxies. There are currently five methods that are used to construct equilibrium models (the reader is referred to Yurin & Springel 2014 for the full list). Most of these methods are based on Jean's theorem, which states that, "any steady-state solution of the collisionless Boltzmann equation depends on the phase space coordinates only through integrals of motion in the given potential, and conversely any function of the integrals is a steady-state solution" (e.g., Zang 1976; Athanassoula & Sellwood 1986; Kuijken & Dubinski 1995; Widrow & Dubinski 2005; McMillan & Dehnen 2007). Other techniques such as the Schwarzschild method (Schwarzschild 1979) or the interactive method by Rodionov et al. (2009) has been proposed to construct equilibrium model that can be used as initial conditions for N-body and hydrodynamic simulations. However, these methods are computationally expensive. In this work, we adopted the method pioneered by Kuijken & Dubinski (1995) and Widrow & Dubinski (2005) to generate the initial conditions that include a gas disk component. This method constructs multi-component axisymmetric galaxy models based on distribution functions. This method is now implemented into the Galactic Initial Conditions (GalactICs) code Widrow (2008). More information on the new version of GalactICs models that includes a gas disk component are given in Deg et al. (2017) (see also, chapter 5).

2.7 Conclusion

This section gives a brief background on galaxies and describes how rotation curves are used to study the distribution of dark matter. It also highlights the strengths and weaknesses of the current methods that are used to derive rotation curves and the different techniques that are currently available to estimate and correct the

non-circular flows such as those induced by bars. The different algorithms that are used to perform numerical simulations of barred galaxies are also described.

Bibliography

Appel, A. W. 1985, SIAM Journal on Scientific and Statistical Computing, vol. 6, no. 1, January 1985, p. 85-103., 6, 85

Athanassoula, E., & Sellwood, J. A. 1986, MNRAS, 221, 213

Athanassoula, E. 2002, Ap&SS, 281, 39

Athanassoula, E., Machado, R. E. G., & Rodionov, S. A. 2013, MNRAS, 429, 1949

Babcock, H. W. 1939, Lick Observatory Bulletin, 19, 41

Barnes, J., & Hut, P. 1986, nature, 324, 446

Begeman, K. G. 1987, Ph.D. Thesis,

Begeman, K. G. 1989, A&A, 223, 47

Bertschinger, E. 1998, ARA&A, 36, 599

Bosma, A. 1978, Ph.D. Thesis,

Bosma, A. 1981, AJ, 86, 1791

Bosma, A. 1981, AJ, 86, 1825

Bouchet, F. R., & Hernquist, L. 1988, ApJS, 68, 521

Blais-Ouellette, S., Amram, P., & Carignan, C. 2001, AJ, 121, 1952

Carignan, C. 1985, ApJ, 299, 59

Carignan, C., & Freeman, K. C. 1985, ApJ, 294, 494

Carignan, C., Beaulieu, S., & Freeman, K. C. 1990, AJ, 99, 178

Chemin, L., de Blok, W. J. G., & Mamon, G. A. 2011, AJ, 142, 109

Chequers, M. H., Spekkens, K., Widrow, L. M., & Gilhuly, C. 2016, MNRAS, 463, 1751

Combes, F., & Sanders, R. H. 1981, A&A, 96, 164

de Blok, W. J. G., Walter, F., Brinks, E., et al. 2008, AJ, 136, 2648-2719

Deg, N., Widrow, L, Randriamampandry, T. H., & Carignan, C., 2017 in prep

de Vaucouleurs, G. 1959, ApJ, 130, 718

de Vaucouleurs G., de Vaucouleurs A., Corwin, Jr. H. G., Buta R. J., Paturel G., Fouqué P., 1991, Third Reference Catalogue of Bright Galaxies. Volume I: Explanations and references. Volume II: Data for galaxies between 0^h and 12^h. Volume III: Data for galaxies between 12^h and 24^h.

Di Teodoro, E. M., & Fraternali, F. 2015, MNRAS, 451, 3021

Du, M., Debattista, V. P., Shen, J., & Cappellari, M. 2016, ApJ, 828, 14

Eskridge, P. B., Frogel, J. A., Pogge, R. W., et al. 2000, AJ, 119, 536

Einasto, J. 1965, Trudy Astrofizicheskogo Instituta Alma-Ata, 5, 87

Efstathiou, G., Davis, M., White, S. D. M., & Frenk, C. S. 1985, ApJS, 57, 241

Epinat, B., Amram, P., & Marcelin, M. 2008, MNRAS, 390, 466

Hayashi, E., Navarro, J. F., Power, C., et al. 2004, MNRAS, 355, 794

Hockney, R. W., & Eastwood, J. W. 1981, Computer Simulation Using Particles, New York: McGraw-Hill, 1981,

Hubble, E. P. 1936, Realm of the Nebulae, by E.P. Hubble. New Haven: Yale University Press, 1936. ISBN 9780300025002,

Goldreich, P., & Tremaine, S. 1978, ApJ, 222, 850

Goldreich, P., & Tremaine, S. 1979, ApJ, 233, 857

Gingold, R. A., & Monaghan, J. J. 1977, MNRAS, 181, 375

Lucy, L. B. 1977, AJ, 82, 1013

Navarro, J. F., Frenk, C. S., & White, S. D. M. 1996, ApJ, 462, 563

Menéndez-Delmestre, K., Sheth, K., Schinnerer, E., Jarrett, T. H., & Scoville, N. Z. 2007, ApJ, 657, 790

McMillan, P. J., & Dehnen, W. 2007, MNRAS, 378, 541

Milgrom, M. 1983, ApJ, 270, 365

Miller, R. H., Prendergast, K. H., & Quirk, W. J. 1970, ApJ, 161, 903

Monaghan, J. J. 1992, ARA&A, 30, 543

Oh, S.-H., de Blok, W. J. G., Walter, F., Brinks, E., & Kennicutt, R. C., Jr. 2008, AJ, 136, 2761-2781

Oort, J. H. 1940, ApJ, 91, 273

Jarrett, T. H., Chester, T., Cutri, R., Schneider, S. E., & Huchra, J. P. 2003, AJ, 125, 525

Józsa, G. I. G., Kenn, F., Klein, U., & Oosterloo, T. A. 2007, A&A, 468, 731

Józsa, G. I. G. 2007, A&A, 468, 903

Krajnović, D., Cappellari, M., de Zeeuw, P. T., & Copin, Y. 2006, MNRAS, 366, 787

Kravtsov, A. V., Klypin, A. A., Bullock, J. S., & Primack, J. R. 1998, ApJ, 502, 48

Kormendy, J. 1983, ApJ, 275, 529

Klypin, A. A., & Shandarin, S. F. 1983, MNRAS, 204, 891

Kuijken, K., & Dubinski, J. 1995, MNRAS, 277, 1341

Ostriker, J. P., & Peebles, P. J. E. 1973, ApJ, 186, 467

Quirk, W. J. 1970, Ph.D. Thesis,

Randriamampandry, T. H., & Carignan, C. 2014, MNRAS, 439, 2132

Randriamampandry, T. H., Combes, F., Carignan, C., & Deg, N. 2015, MNRAS, 454, 3743

Randriamampandry, T. H., Deg, N., Carignan, C., Combes, F., & Spekkens, K. 2016, A&A, 594, A86

Rautiainen, P., Salo, H., & Laurikainen, E. 2002, MNRAS, 337, 1233

Rautiainen, P., Salo, H., & Buta, R. 2004, MNRAS, 349, 933

Rogstad, D. H., Lockhart, I. A., & Wright, M. C. H. 1974, ApJ, 193, 309

Rodionov, S. A., Athanassoula, E., & Sotnikova, N. Y. 2009, MNRAS, 392, 904

Rubin, V. C., Burstein, D., Ford, W. K., Jr., & Thonnard, N. 1985, ApJ, 289, 81

Rubin, V. C., Ford, W. K., Jr., Thonnard, N., & Burstein, D. 1982, ApJ, 261, 439

Rubin, V. C., & Ford, W. K., Jr. 1970, ApJ, 159, 379

Sanders, R. H., & McGaugh, S. S. 2002, ARA&A, 40, 263

Schwarzschild, M. 1954, AJ, 59, 273

Schwarzschild, M. 1979, ApJ, 232, 236

Schoenmakers, R. H. M., Franx, M., & de Zeeuw, P. T. 1997, MNRAS, 292, 349

Schoenmakers, R. H. M. 1999, Ph.D. Thesis,

Sheth, K., Regan, M., Hinz, J. L., et al. 2010, PASP, 122, 1397

Sellwood, J. A. 1987, ARA&A, 25, 151

Sellwood, J. A., & Wilkinson, A. 1993, Reports on Progress in Physics, 56, 173

Sofue, Y. 2016, PASJ, 68, 2

Sofue, Y. 2013, PASJ, 65,

Sofue, Y., & Rubin, V. 2001, ARA&A, 39, 137

Spekkens, K., & Sellwood, J. A. 2007, ApJ, 664, 204

Spinoso, D., Bonoli, S., Dotti, M., et al. 2016, arXiv:1607.02141

Springel, V. 2005, MNRAS, 364, 1105

Springel, V., Yoshida, N., & White, S. D. M. 2001, New Astronomy, 6, 79

Slipher, V. M. 1914, Popular Astronomy, 22, 19

Swaters, R. A., Verheijen, M. A. W., Bershady, M. A., & Andersen, D. R. 2003, ApJL, 587, L19

Trachternach, C., de Blok, W. J. G., Walter, F., Brinks, E., & Kennicutt, R. C., Jr. 2008, AJ, 136, 2720-2760

Toomre, A. 1964, ApJ, 139, 1217

Volders, L. M. J. S. 1959, Bulletin of the Astronomical Institutes of the Netherlands, 14, 323

Walter, F., Brinks, E., de Blok, W. J. G., et al. 2008, AJ, 136, 2563-2647

Weiner, B. J., Sellwood, J. A., & Williams, T. B. 2001, ApJ, 546, 931

Widrow, L. M., & Dubinski, J. 2005, ApJ, 631, 838

Widrow, L. M. 2008, ApJ, 679, 1232-1238

Wong, T., Blitz, L., & Bosma, A. 2004, ApJ, 605, 183

Yurin, D., & Springel, V. 2014, MNRAS, 444, 62

Zang, T. A. 1976, Ph.D. Thesis,

Zhao, H. 1996, MNRAS, 278, 488

Zwicky, F. 1933, Helvetica Physica Acta, 6, 110

Zwicky, F. 1937, ApJ, 86, 217

Chapter 3

Paper I: Estimating non-circular motions in barred galaxies using numerical N-body simulations

This chapter have been published in the Monthly Notices of the Royal Astronomical Society (MNRAS): T. H. Randriamampandry, F. Combes, C. Carignan and N. Deg, MNRAS 454, 3743-3759 (2015)

Abstract

The observed velocities of the gas in barred galaxies are a combination of the azimuthally averaged circular velocity and non-circular motions, primarily caused by gas streaming along the bar. These non-circular flows must be accounted for before the observed velocities can be used in mass modelling. In this work, we examine the performance of the tilted-ring method and the DISKFIT algorithm for transforming velocity maps of barred spiral galaxies into rotation curves (RCs) using simulated data. We find that the tilted-ring method, which does not account for streaming motions, under-/overestimates the circular motions when the bar is parallel/perpendicular to the projected major axis. DISKFIT, which does include streaming motions, is limited to orientations where the bar is not aligned with either the major or minor axis of the image. Therefore, we propose a method of correcting RCs based on numerical simulations of galaxies. We correct the RC derived from the tilted-ring method based on a numerical simulation of a galaxy with similar properties and projections as the observed galaxy. Using observations of NGC 3319, which has a bar aligned with the major axis, as a test case, we show that the inferred mass models from the uncorrected and corrected RCs are significantly different. These results show the importance of correcting for the non-circular motions and demonstrate that new methods of accounting for these motions are necessary as current methods fail for specific bar alignments.

3.1 Introduction

The rotational velocities obtained from gas observations are one of the most commonly used tools to study the mass distributions of spiral galaxies. It is often assumed that the gaseous motions are purely circular due to their low velocity dispersions. However, the presence of a galactic bar will induce non-circular motions due to the streaming along the bar. Since bars account for two-thirds of nearby galaxies (eg. de Vaucouleurs et al. 1991; Eskridge et al. 2000; Knapen et al. 2000; Whyte et al. 2002; Marinova & Jogee 2007; Menéndez-Delmestre et al. 2007; Barazza et al. 2008; Aguerri et al. 2009; Marinova et al. 2009; Méndez-Abreu et al. 2010; Masters et al. 2011), it is important to properly account for these motions.

The study of the mass distribution is done by comparing the observed RC with the expected contributions from the gas, stars and dark matter, assuming axisymmetry, and that the gas is in circular motions (e.g. de Blok et al. 2008). For the dark matter component, an empirical or theoretical density profile is used. There are several dark matter density profiles suggested in the literature. The two most commonly used are the NFW profile (Navarro, Frenk & White 1996) derived from cosmological simulations with a central cusp and the isothermal (ISO) model (see e.g: Carignan 1985; Carignan & Freeman 1985) with a central flat core (see also: Einasto 1969; Burkert 1995; Kravtsov et al. 1998), a more general form of the dark matter density profile is also given by Blais-Ouellette et al. (2001). Alternative model such as the Modified Newtonian Dynamics (MOND) (Milgrom 1983a,b,c) do not have a dark matter component. Milgrom (1983b) stipulated that there is no need for a dark matter halo to explain the flatness of galaxies' rotation curves (RCs) if the law of gravity is modified below a critical acceleration a_0. A comparison between ISO dark matter models and MOND models, for a sample of dwarf and spiral galaxies, is given in Randriamampandry & Carignan (2014) but a larger sample is needed before a final conclusion can be made.

In order to distinguish between both these and other models, RCs that represent the gravitational potential are necessary. RCs are often derived from observed velocity maps of gas using the tilted ring method (Rogstad et al. 1974). This method divides the velocity map into co-centered rings and infers a variety of kinematic parameters, including the circular velocities. It has been implemented in the GIPSY (Allen et al. 2011) task ROTCUR (Begeman 1989). Unfortunately, ROTCUR does not correct for the non-circular motions. There are other methods that have been developed to account for these motions, including the publicly available DiskFit code (Spekkens & Sellwood 2007). DiskFit creates physical models from the observed rotation velocities and extract the non-circular motions using a χ^2 minimization technique (for more details see : [1]). DiskFit has proven to be able to detect weak bars (Kuzio de Naray et al. 2012). It was specifically designed to fit a non-axisymmetric flow pattern to two-dimensional velocity maps (Spekkens & Sellwood 2007). However, it is well known that the DiskFit bar flow algorithm fails when the bar is almost parallel to the major or minor axis because of the degeneracy of the velocity components (Sellwood & Sánchez 2010).

Dicaire et al. (2008) used numerical models with pure rotation and compared the known circular velocities with the observed rotational velocities. They found that if a bar is perpendicular to the major axis of a galaxy, the measured rotational velocities and thus the mass is over estimated and the contrary if the bar is parallel to the major axis.

We propose an alternate method to account for non-circular motions using N-body simulations. A grid of models with different bar orientations, strengths, and bulge-disk-halo compositions is generated. RCs from images of these models are made using ROTCUR, which are then compared to the RCs calculated from the gravitational potential and its derivatives. This comparison gives the corrections necessary for non-circular motions. To get the corrected RC for a real galaxy, the best corresponding model from the grid of simulations is selected and the

[1] `http://www.physics.rutgers.edu/~spekkens/diskfit/`

corrections derived from the simulation are applied to the actual galaxy's RC derived from ROTCUR.

The paper is organised as follow: Section 3.2 describes the details of both the numerical simulations and the ROTCUR and DiskFit algorithms. Section 3.3 compares the RCs derived from the simulations using ROTCUR and DiskFit to the RC obtained from the gravitational potential. In Section 3.4 we describe our new method of correcting RCs and use NGC 3319 as a test case to show the importance of properly accounting for non-circular motions in mass models. Finally, in Section 5 we present our conclusions.

3.2 Data analysis

3.2.1 N-body simulations

We use a series of spiral galaxy simulations, with different Hubble types, Sa, Sb, Sd, fitted to observed rotation velocities (cf Chilingarian et al. 2010) and different radial distributions of dark matter, with either a core or a cusp in the center, and different dark-to-visible mass ratios (maximum disk or not). They give a range of rotation velocities with various shapes, rising more or less slowly with radius. We do not vary the total mass of the galaxies, since only the shapes of the rotation velocities are important, and masses can be varied by a change of units. It is acknowledged that there is a mass and size evolution along the Hubble sequence (see e.g. van der Wel et al. 2014), and that late-type spiral galaxies are lighter and smaller, but these can be taken into account afterwards through rescaling. For all galaxy models, the total mass inside 35 kpc is 2.4 10^{11} $M_{\odot}$, with 75% in dark matter and 25% in baryons, for the standard model (based on the ΛCDM cosmology) and equality between baryons and dark matter for the maximum disk model.

Model	M_b 10^{10} $M_\odot$	r_b kpc	M_d 10^{10} $M_\odot$	r_d kpc	M_h 10^{10} $M_\odot$	r_h kpc	M_{gas} 10^{10} $M_\odot$	r_{gas} kpc
gSa	4.6	2.	6.9	4.	11.5	10.	1.3	5.
gSb-st	1.1	1.	4.6	5.	17.2	12.	0.9	6.
gSb-dmx	2.2	1.	9.2	5.	11.4	12.	0.9	6.
gSb-nfw	1.1	1.	4.6	5.	17.2	12.	0.9	6.
gSd-st	0.	–	5.7	6.	17.2	15.	1.7	7.
gSd-dmx	0.	–	11.4	6.	11.4	15.	1.7	7.
gSd-nfw	0.	–	5.7	6.	17.2	15.	1.7	7.

TABLE 3.1: Initial conditions for the various components (bulge, disk, halo, and gas) of the different models used. All models are normalized to giant galaxies to explore the different shapes. Dwarfs can be obtained through rescaling (see text).

We have used two different simulation codes, in order to test that our assumptions are not biasing the results. In both kinds of simulations, the runs are fully self-consistent, with live dark haloes. The first code is based on a 3D particle-mesh and the Fast-Fourier Transform (FFT) technique to solve the Poisson equation, and the gas is represented by sticky particles (FFT-sticky particles). We also ran a set of simulations using the Tree-SPH code used in the Galmer project (Di Matteo et al. 2007). More details on these simulations including the hydrodynamics, star formation, and feedback can be found in Appendix A. The total number of particles is 240k in the FFT-sticky code and 480k in the Tree-SPH code.

These produced different outputs for the gas particle distributions, but the effects of the bar on the observed velocity maps were the same. Since the conclusions are the same, we will primarily examine the results for the FFT-stickly particles simulations and the results for the Tree-SPH runs can be found in Appendix B.

For the initial conditions of the galaxies of different Hubble types, we have followed the procedure described by Di Matteo et al. (2007). The halo and the optional bulge are modeled as a Plummer sphere, and the stellar and gaseous disks follow a Miyamoto-Nagai density profile.

The mass and characteristic radii of all components in the seven initial conditions, are displayed in Table 3.1. The standard model (-st) has a disk dominated by dark matter, with a central core. A NFW model, with a cusp and a central concentration of c = 8 has been run (-nfw), then a maximum disk model (-dmx) with equal mass between baryons and dark matter within the optical disk. The initial rotational velocities, corresponding to the main variations of the parameters, are displayed in figure 3.1.

The expected velocities ($V_{expected}$) were calculated from the gravitational potential and its derivatives. More specifically, the potential derived from the disk is averaged out azimuthally, to obtain $\Phi(r)$, and the circular velocity V_{circ} is

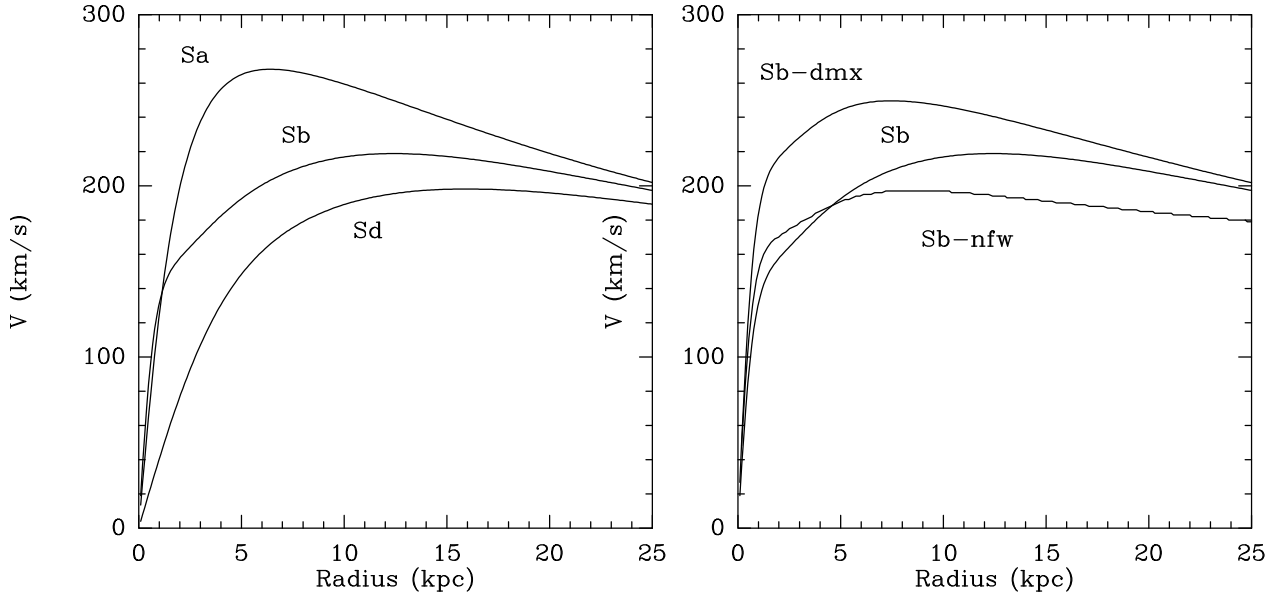

FIGURE 3.1: Initial RCs of the various models, described in table 3.1. The left plot compares the various morphological types, and the right plot the various dark matter distributions.

$$V_{circ}^2 = -r\frac{d\langle\Phi\rangle}{dr} \tag{3.1}$$

3.2.2 Snapshots

The snapshots from the FFT-sticky particles simulation were extracted from the data using a projection code specifying the inclination angle and the position angle and deriving the radial velocity of the gas particles at each point of a data cube. The data cube have three axes, the first and second axis are the right ascension and declination and the third axis is the velocity in km/s. Each cubes have 50 channels with a 12.5 km/s velocity resolution. The cube is then transformed into a fits file. The projection angle PA was varied between 10 to 180 degrees in order to cover a wide range of intrinsic bar orientations for all the snapshots.

We select the snapshots where the bar has reached a quasi-stationary state (most of the gas have been converted into stars), but is still strong enough, and there is enough gas remaining in the disk to sample the rotation velocities with gas only. Indeed, the simulations do not take into account gas accretion form the cosmic filaments, and the gas density is progressively reduced by star formation.

3.2.3 Measuring rotation curves

3.2.3.1 Using the tilted-ring method with ROTCUR

ROTCUR uses the tilted-ring method (Rogstad et al. 1974), which divides the observed velocity field into concentric rings and estimates the circular velocities and other kinematical parameters such as position angle (PA) and inclination using a χ^2 minimization technique. This method assumes that the gas is moving purely along circular orbits. Each ring is characterized by the rotation center x_c and y_c, the systemic velocity V_{sys}, the expansion velocity V_{exp} (assumed here to be zero),

the inclination angle and PA. These parameters can be fixed or let free to vary depending on the user. The line of sight velocity at any position in the ring is then given by:

$$V(x, y) = V_{sys} + V_C sin(i) cos(\theta), \tag{3.2}$$

where θ is the position angle with respect to the receding major axis measured in the plane of the sky, V_{sys} the systemic velocity and i the inclination angle.

θ is related to the actual PA by the following equations:

$$cos(\theta) = \frac{-(x - x_c)sin(PA) + (y - y_c)cos(PA)}{R} \tag{3.3}$$

$$sin(\theta) = \frac{-(x - x_c)cos(PA) + (y - y_c)cos(PA)}{Rcos(i)} \tag{3.4}$$

The data cubes extracted from the simulation snapshots were analyzed with the Groningen Image Processing System (GIPSY: `http://www.astro.rug.nl/~gipsy/`) software. The task RFITS was used to convert the fits file into a GIPSY format, then the fits headers were changed using FIXHED. The following parameters were modified in the header; the axis and the pixel size which is necessary before extracting the velocity fields. The task MOMNT was used to produce the moment maps, and the rotation velocities were derived using ROTCUR. The expansion velocity is fixed to zero for all the models. We choose an inclination angle of 60 degrees which is suitable for the kinematical studies. The systemic velocity (V_{sys}) and position angle (PA) are fixed using the following values: V_{sys} = 0.0 km s^{-1} and PA = 0.0 degree during the fitting procedures.

The process of deriving the rotation curves includes three steps; firstly, the PA and inclination are held fixed using the optical values and the systemic velocity and position centre (Xpos and Ypos) are allowed to vary; secondly, the systemic velocity and the kinematic centre are held fixed and the PA and inclination are let free to vary; finally, all the above parameters are fixed and the average values are used to derive the rotation curves.

3.2.3.2 Using the DiskFit bisymmetric model

DiskFit (Spekkens & Sellwood 2007) is specifically designed to correct the non-circular flows due to bars. It creates physical models from the observed velocity fields and extracts sthe velocities and other parameters from the model velocity map. DiskFit also uses a bootstrap method to estimate the uncertainty on the parameters and uses all to data during the fitting procedures.

DiskFit compares the observed velocity field with the following equation:

$$V_{model} = V_{sys} + \sin(i)[V_t\cos(\theta) - V_{2,t}\cos(2\theta_b)\cos(\theta) - V_{2,r}\sin(2\theta_b)\sin(\theta) \tag{3.5}$$

where V_t is the circular velocity, $V_{2,t}$ and $V_{2,r}$ the amplitudes of the tangential and radial component of the noncircular motions for a bisymmetric flow model. This form of the equation is for bisymmetric flows from bars. Moreover, DiskFit can also deal with warped galaxies. Regardless, if the gas is moving on purely circular orbits, this equation reduces to the key equation of the tilted-ring method.

DiskFit estimates the rotational velocities and the other parameters using a χ^2 minimization technique:

$$\chi^2 = \sum_{n=1}^{N}\left(\frac{V_{obs}(x,y) - \sum_{k=1}^{k}\omega_{k,n}V_k}{\sigma_n}\right)^2 \tag{3.6}$$

where $V_{obs}(x,y)$ is the observed velocity at the position (x,y) on the sky, σ_n is the uncertainty, $\omega_{k,n}$ is a weighting function which includes the trigonometric factors and also defines an interpolation scheme for the projected model (Sellwood & Sánchez 2010). Some of the advantages of DiskFit are listed in Sellwood & Sánchez (2010). DiskFit uses all the data in a single fit, which is necessary to detect mild distortion and also gives a better estimate of the uncertainty using a bootstrap method (Spekkens & Sellwood 2007).

3.3 Results and discussions

3.3.1 Results using ROTCUR

The results for the FFT-sticky particles code for three different bar orientations are shown in figures 3.2, 3.3 and 3.4 for the gSa, gSb and gSd models respectively. The snapshots were taken at the following epoch T=700 Myrs for gSa, T = 700 Myrs for gSb and T = 900 Myrs for gSd. The intensity maps of the particles, which show the orientations of the bar (MOMENT0 maps) are shown in the left panels and the velocity fields with iso-velocity contours (ΔV = 50 km s^{-1}) (MOMENT1 maps) are shown in the middle. The axes of the moment maps are in arcsec. A distance of 16.5 Mpc is adopted to convert from arcsec to parsec scale for all the models. Comparison between the expected RCs and the measured RCs using ROTCUR are shown in the right panels. The expected RCs are presented as continuous lines and the RCs derived using ROTCUR as black circles.

ROTCUR over-estimates the rotation when the bar is perpendicular to the major axis except for the gSa model for which most of the mass comes from the bulge component. The top panels of figure 3.2 shows that the measured rotation velocities using ROTCUR and the expected rotation velocities are in good agreement even if the bar is perpendicular with the major axis. This is probably because the higher velocity due to the gas streaming motion along the bar is compensated by the contribution from the bulge. The differences between the measured rotation velocities and those expected from the gravitational potential are the largest when the bar is aligned with the major axis. Figure 3.5 shows a comparison between the expected rotation velocities from the total mass of the galaxy and the average rotation velocities (obtained using ROTCUR) for four snapshots. The rotation velocities of 12 simulated galaxies with different bar orientations were extracted and averaged for each snapshot (P.A. varies between 0 and 180 in steps of 15 degrees). The error-bars are the 1-σ standard deviations that indicate the possible spread

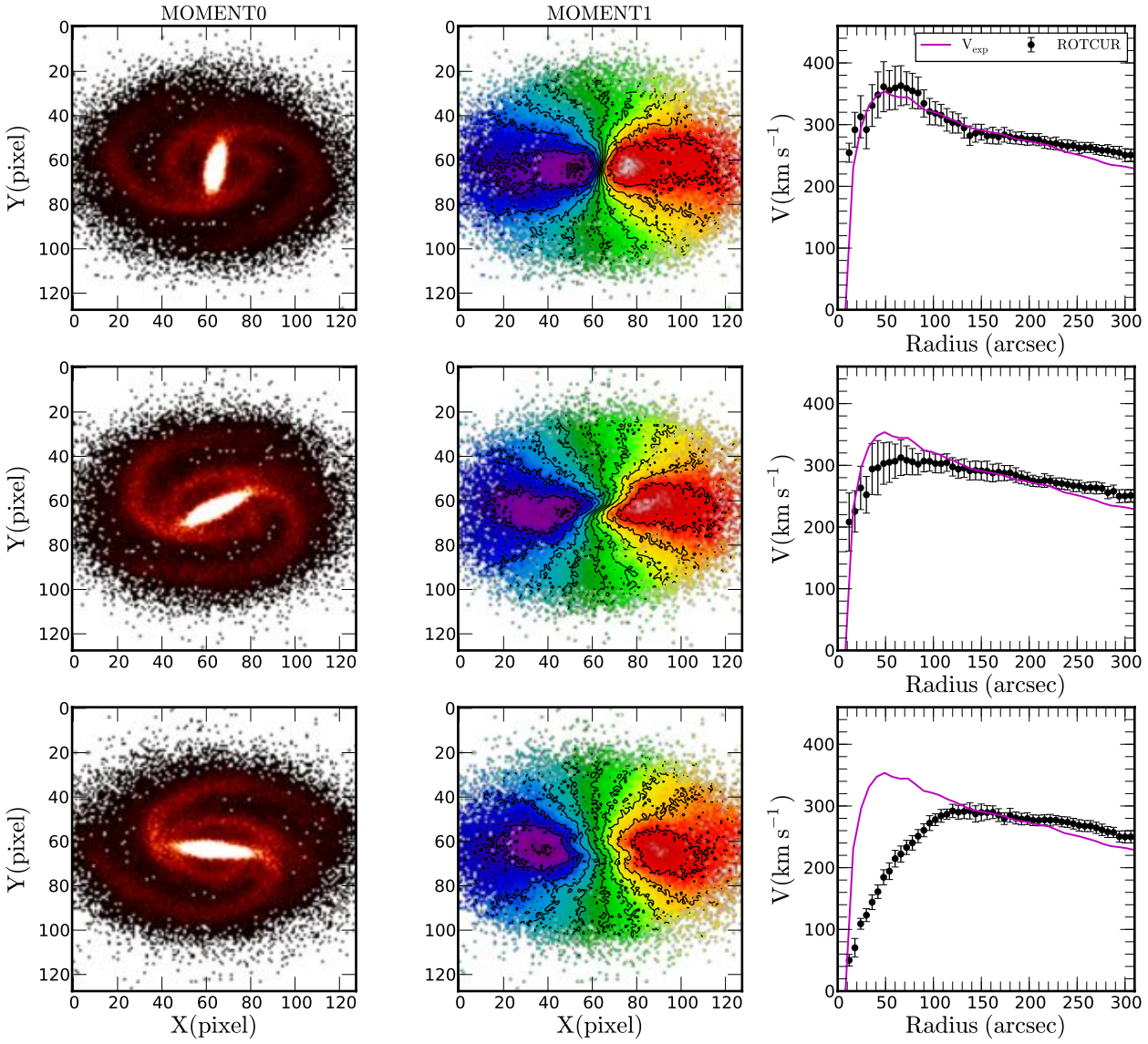

FIGURE 3.2: Three different bar positions for the model gSa (FFT-Sticky particles, T= 700 Myrs) Top panel: the bar is perpendicular to the major axis, middle panel: intermediate position and bottom panel: parallel to the major axis. The first column is the moment0 map, second column the moment 1 map superposed with the iso-velocity contours and the third column the comparison between the expected velocities shown as a continuous line and the measured rotation velocities derived using ROTCUR (black points). The axes of the moment maps are in pixels (1 pixel = 5 arcsec).

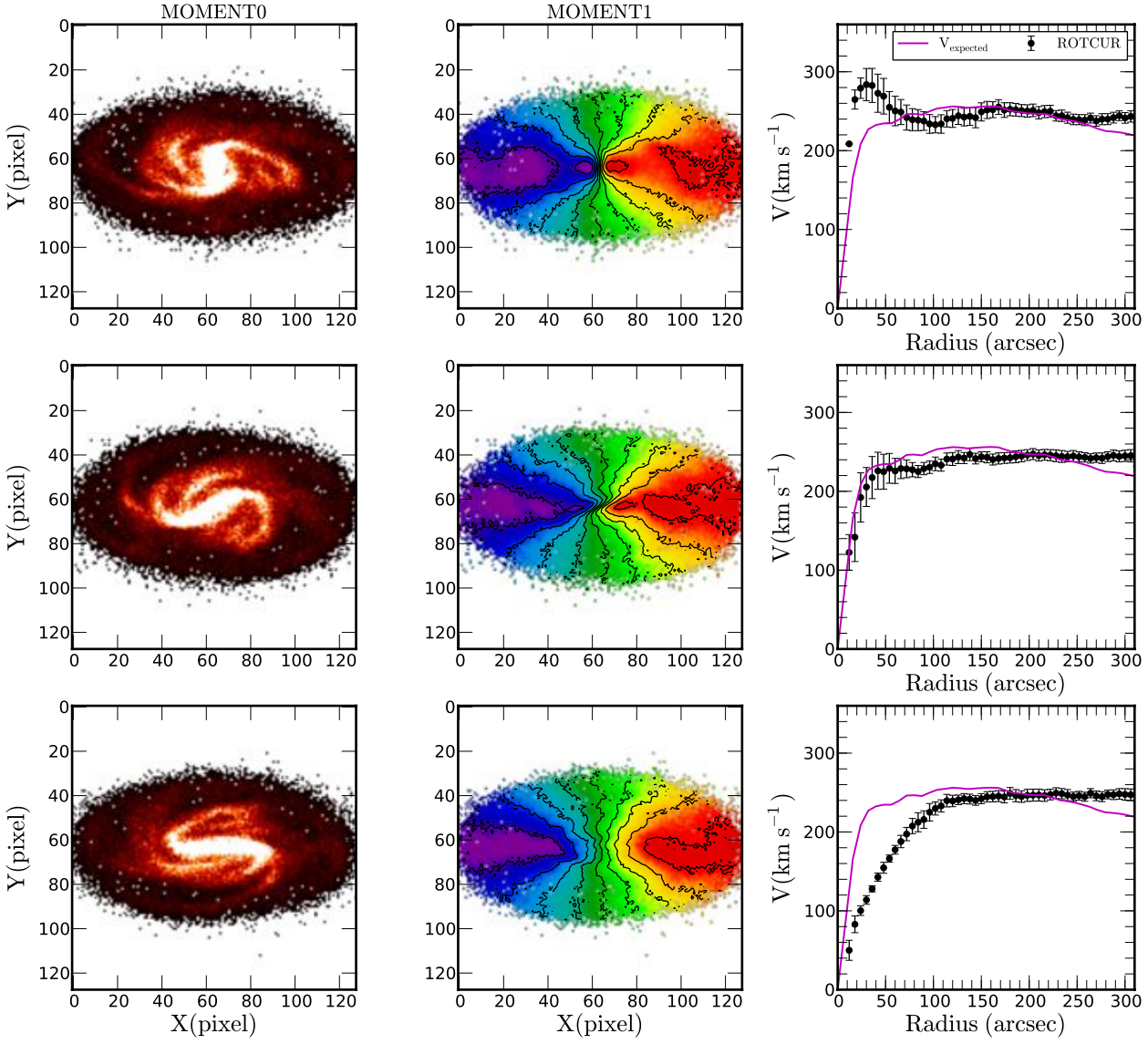

FIGURE 3.3: Three different bar positions for the model gSb (FFT-sticky particles , T = 700 Myrs see figure 3.2 for details).

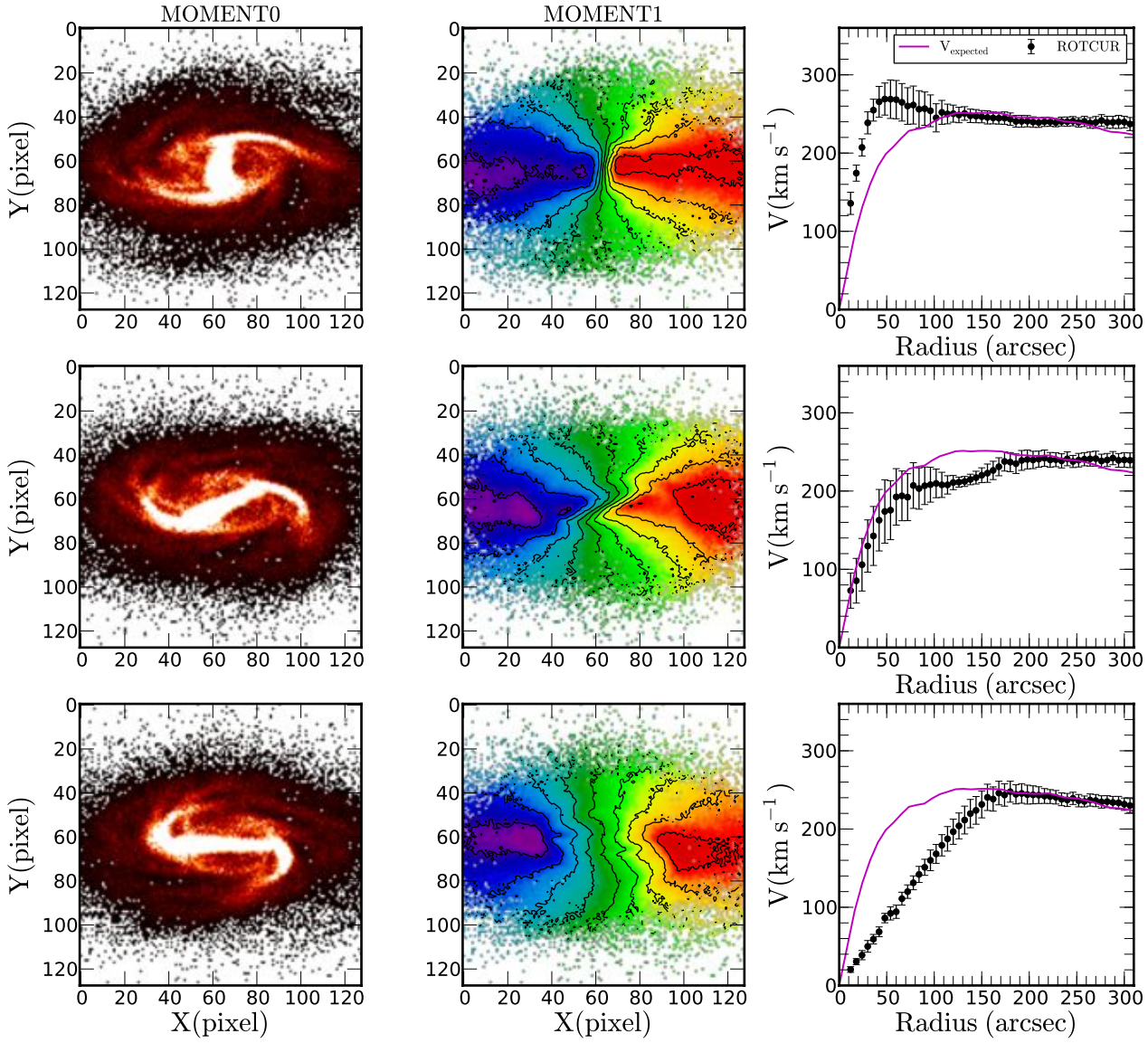

FIGURE 3.4: Three different bar positions for the model gSd (FFT-sticky particles, T = 900 Myrs see figure 3.2 for details).

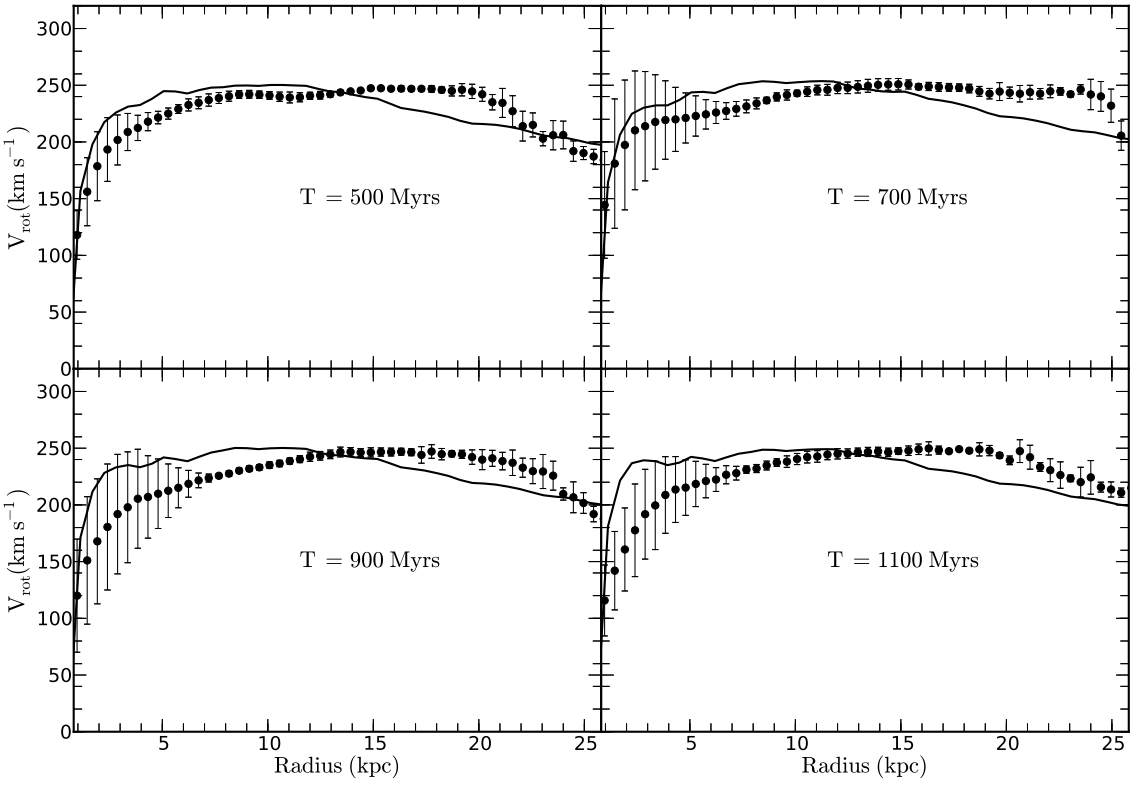

FIGURE 3.5: Standard gSb galaxy model: comparison between the expected RCs calculated from the gravitational potential as continuous lines and the average RCs for different bar orientations as filled circles with the 1-σ error bars (here the error-bars indicate the possible spread for the different projections). The RCs of 12 simulated galaxies with different bar orientations were extracted and averaged for each snapshot (PA varies between 0 and 180 degrees with a step of 15 degrees). The epochs of the snapshots are shown on the graph.

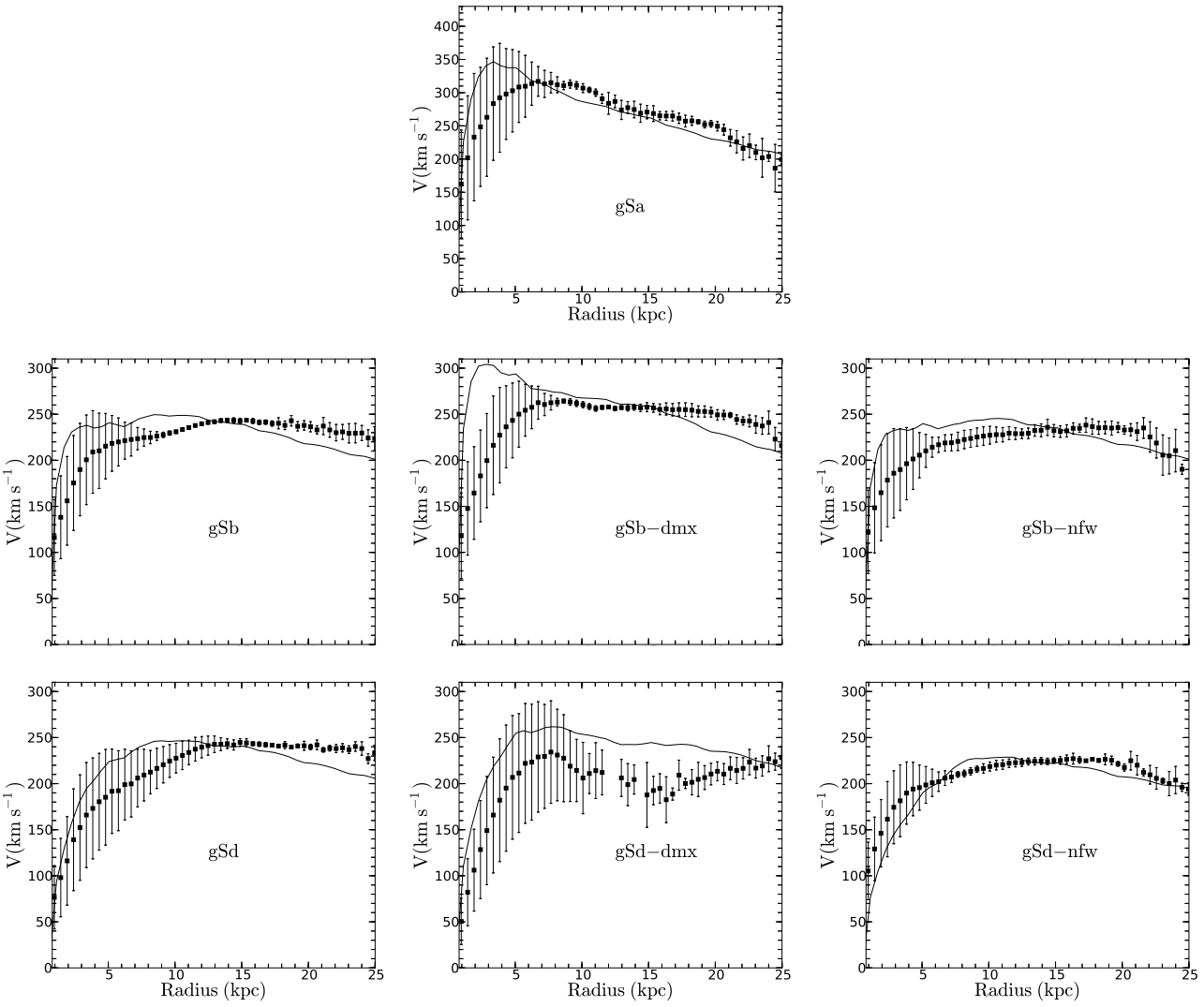

FIGURE 3.6: This figure shows the comparison between measured and calculated RCs for all the models listed in table 3.1 for the snapshots with the strongest bar (the epochs are given in table 3.2). Lines and symbols are the same as in figure 3.5.

Model	Epochs Myr	maximum deviation km s^{-1}
gSa-st	800	60.72
gSb-st	1000	51.45
gSb-dmx	600	53.45
gSb-nfw	900	52.09
gSd-st	1000	57.27
gSd-dmx	700	68.48
gSd-nfw	900	25.80

TABLE 3.2: Maximum departure from the average velocity (i.e maximum deviation) for the snapshots with the strongest bars.

for the different projections. In the top-left panel, the bar starts to form but its effect on the derived rotation velocities is small. The two bottom panels present larger errorbars, with a maximum of 60 km s^{-1} in the inner regions.

The average RCs derived from the snapshots with the strongest bars (see Table 2 for the epochs) for all the models are shown in figure 3.6. The top panel is the gSa model with an isothermal dark matter halo. The average of the measured RCs seems to be lower compared to the expected rotation velocities calculated from the gravitational potential. The errorbars are larger in the inner parts of the modeled galaxies which implies that the differences between the rotation velocities are only due to the bar orientations. These errorbars represent the variation of the derived RCs compared to the mean RCs. The gSb model (FFT-sticky) is shown in the middle panel. On the left is the model with the isothermal dark matter halo, in the middle the maximum disk model and on the right the NFW model. The gSd model is presented in the bottom panel; the standard model on the left, the maximum disk model in the middle and the NFW model on the right.

The maximum departure from the average rotation velocities (maximum standard deviation) for each model, are given in table 3.2. The first column is the name of the model, the second column the epoch corresponding to the strongest bar and the last column the maximum deviation from the mean velocity.

3.3.2 Bisymmetric model results using DiskFit

An input parameter file is used to run DiskFit. This file includes the following: a fits file that contains the velocities which are used to derive the kinematics; the initial values for the position angle of the disk and bar, the systemic velocity, the axis ratio and the kinematic center. These parameters can be fixed or let free to vary. For a complete list of parameters the reader is advised to look at the original paper of Spekkens & Sellwood (2007) and the DiskFit manual.

The results for the gSb model (T= 700 Myrs) using the bisymmetric model is shown in figure 3.7 for three different bar orientations. Top panel shows the bar perpendicular to the major axis, middle panel shows the bar in an intermediate position and on the bottom panel the bar is parallel to the major axis. The first column is the moment0 map, second column the moment 1 map superposed with the iso-velocity contours and the third column the comparison between the expected velocities shown as a continuous lines and the DiskFit results. The mean circular velocity V_t is shown as black circles, the tangential component of non-circular motion $V_{2,t}$ as blue diamonds, radial components of the non-circular motion $V_{2,r}$ as red squares and the expected circular velocity $V_{expected}$ as a continuous magenta lines. Φ_b is the bar position angle in degrees obtained from DiskFit. DiskFit is able to reproduce the expected velocities calculated from the gravitational potential and its derivatives when the bar is in intermediate positions but runs into difficulties when the position angle of the bar Φ_b is parallel or perpendicular to the major axis. This shows that DiskFit produces very large values for the rotation velocities and the errorbars when the bar is perpendicular with the major axis because of the degeneracy in the model parameters (Sellwood & Sánchez 2010).

Figure 3.8 compares the projected position angle of the bar $\Phi_{b,projected}$ and those obtained using DiskFit. DiskFit gives higher values as compared to the expected position angle of the bar Φ_b and run into difficulty when the bar is close to 90 degrees.

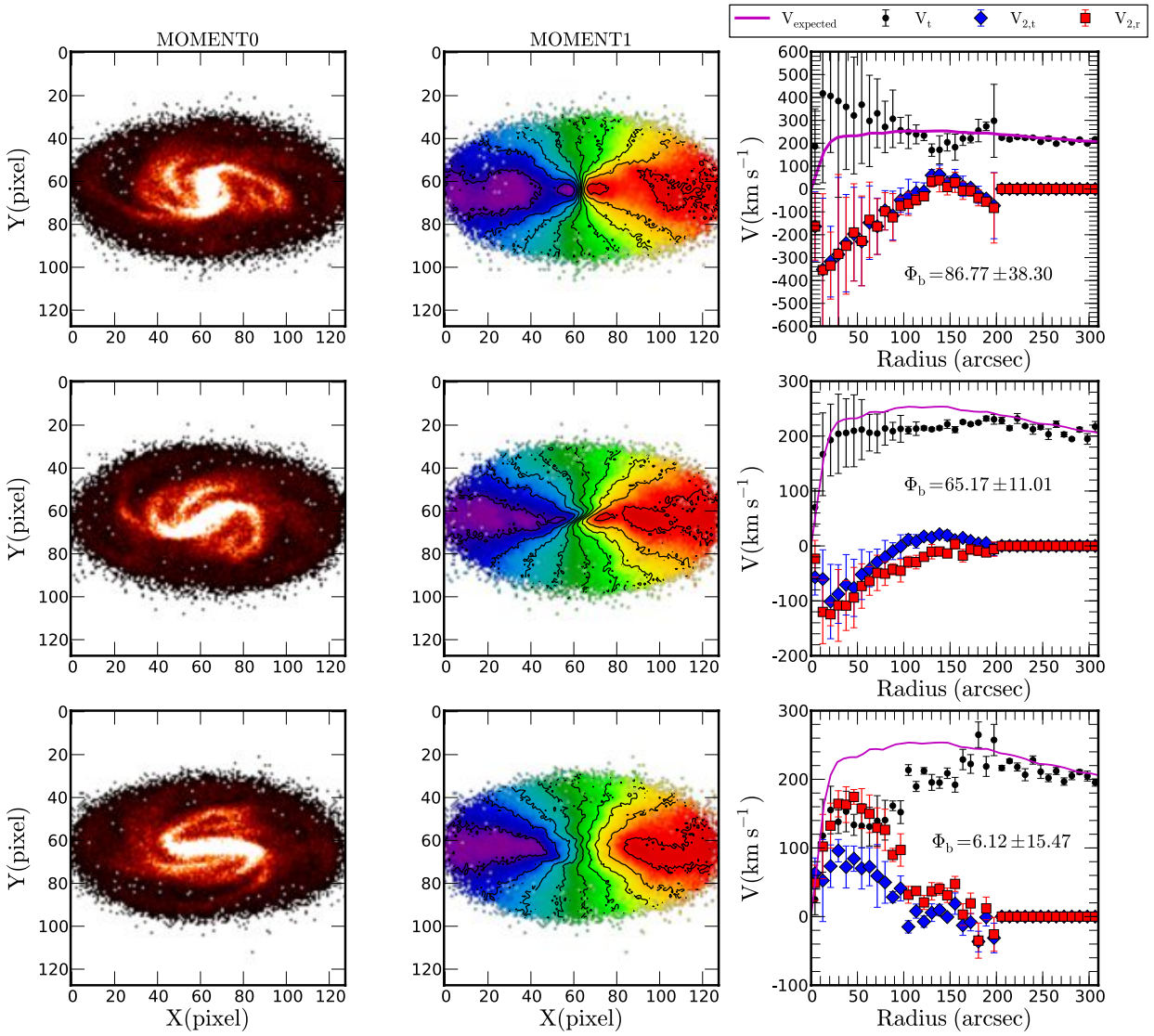

FIGURE 3.7: DiskFit results using the bisymmetric model (m=2) for the gSb model (T = 700 Myrs). Top panel: the bar is perpendicular to the major axis, middle panel: intermediate position and bottom panel: parallel to the major axis. The first column is the moment0 map, second column the moment 1 map superposed with the iso-velocity contours and the third column the comparison between the expected velocities shown as a continuous line and the and the DiskFit results. The mean circular velocity V_t is shown as black circles, the tangential component of non-circular motion $V_{2,t}$ as diamonds, radial components of the non-circular motion as squares and the expected circular velocity $V_{expected}$ as a continuous lines. Φ_b is the bar position angle in degrees obtained from DiskFit. The axes of the moment maps are in pixels (1 pixel = 5 arcsec).

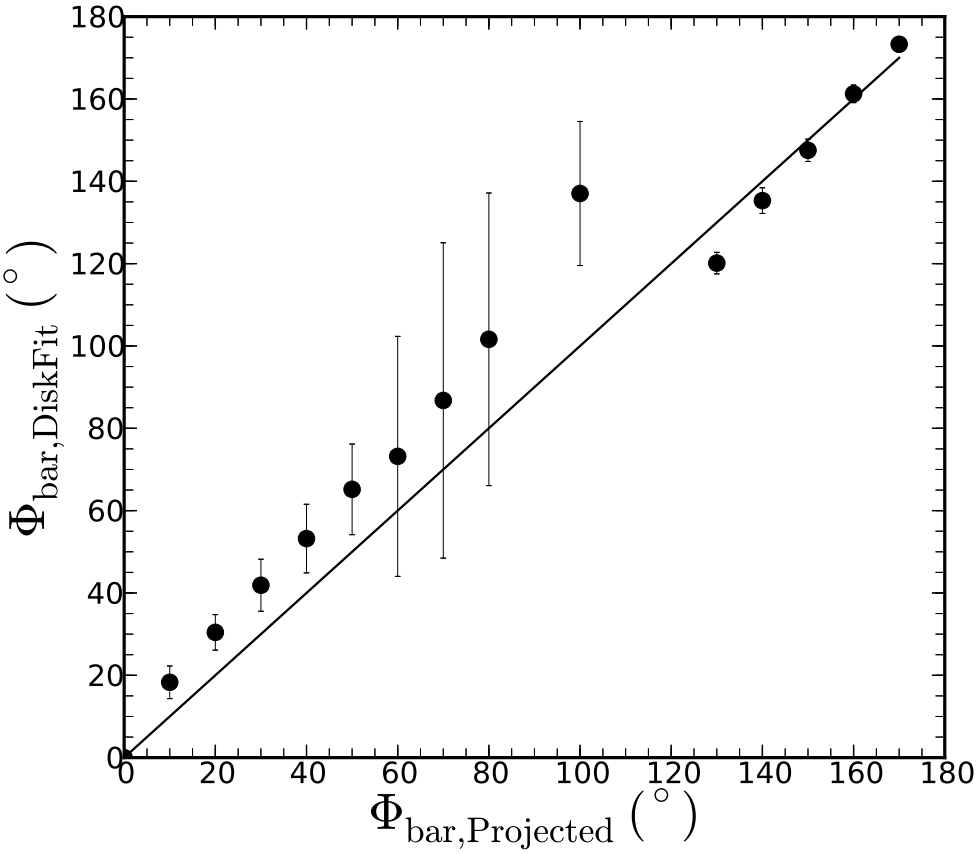

FIGURE 3.8: Comparison between the projected bar position angles and those obtained from DiskFit.

This is the reason why a different approach is needed when the bar is aligned with the major or minor axis. Here we propose to use N-body simulations of barred galaxies to estimate the non-circular motions.

3.4 Test case : NGC 3319

DiskFit and ROTCUR are both very successful methods for deriving RC s from velocity maps. However, Section 3 uses simulations to show that both methods fail at recovering the true RC when a bar is aligned with the major or minor axis of an image. An alternate approach may be to use simulations to correct the RCs for non-circular motions. This will avoid many of the issues with either ROTCUR or DiskFit. We illustrate this method using NGC 3319, which has its bar aligned with the major axis, as a test case. NGC 3319 is a gas-rich barred spiral galaxy classified as SBcd(rs) by de Vaucouleurs et al. (1991) at a distance of 14.3 Mpc (Sakai et al. 1999). We compare the inferred mass profile for the uncorrected and corrected RCs and show that the conclusions about the dark halo structure vary greatly. While our method still needs refinement, this result clearly demonstrates the importance of taking into account non-circular motions.

3.4.1 Observations and data reduction

The HI observations were obtained using the C configuration of the Very Large Array (VLA) for a total observing time of 5.75h on-source. Details of the observations are presented in Moore & Gottesman (1998). The raw data were retrieved from the archive, edited and calibrated using the standard NRAO Astronomical Image Processing System (AIPS) packages. Data cubes were then obtained and cleaned with the AIPS task IMAGR using robust0 weighting, which optimizes sensitivity and spatial resolution. 1031+561 is the phase and amplitude calibrator and 3C286 the flux calibrator. The C array data provide the proper spatial resolution

for mass model analysis. The data cubes have 64 channels with 10.33 km s^{-1} velocity resolution and 16 arcsecs angular resolution, which corresponds to a linear physical resolution of ∼1 kpc at the adopted distance of 14.3 Mpc. The moment maps were extracted from the data cubes using the AIPS task MOMNT. Figure 3.9 shows four different maps for NGC 3319. The WISE W1 image is shown at the top left. This band is essentially free from dust extinction and gives the best representation of the stellar content of the galaxy. The moment 0 map (HI gas distribution) is at the top right, the moment1 map (velocity field) at the bottom left and the moment2 map (velocity dispersion) in the bottom right panel.

The tilted ring method, implemented in the GIPSY task ROTCUR, is used to derive the RC . The moment1 velocity map was used as input for ROTCUR. The tilted ring analysis was done in three steps:

- First, the position angle (P.A.) and inclination angle (i) were fixed using the values of 37° and 58° found by Moore & Gottesman (1998) in order to estimate the systemic velocity and the kinematical centre. Our measured rotation centre and systemic velocity of 742 ± 2 km s^{-1} are consistent with Moore & Gottesman (1998) (see their table 3).

- Second, the systemic velocity and the rotation centre were kept fixed using the values obtained in the first step and the position angle and inclination were allowed to vary to investigate their variation as a function of radius.

- Finally in the final step, the projection parameters were all fixed and only the rotation velocities were derived.

The results from the tilted ring analysis are presented in figure 3.10. The variation of the inclination as a function of radius is shown in the top panel, the position angle in the middle panel and the RCs in the bottom panel. The results from the receding half is presented as red squares, those from the approaching half as blues circles and those obtained using both halves as black diamonds.

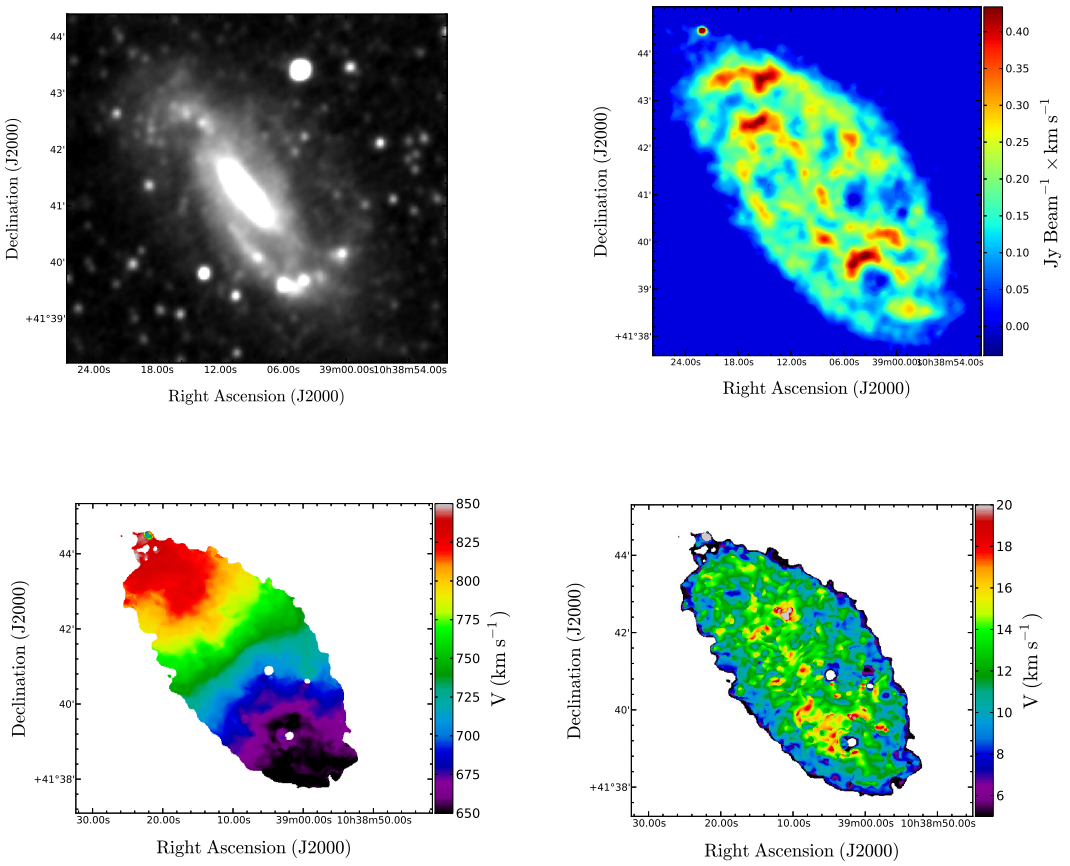

FIGURE 3.9: This figure shows several maps of NGC 3319. The top left panel shows the WISE W1 band (3.4 microns) image, where the bar and spiral arms are clearly seen; the moment0 map (HI distribution) is shown in the top right panel, the moment1 map (HI velocity field) in the bottom left panel and the moment2 map (HI velocity dispersion) in the bottom right corner.

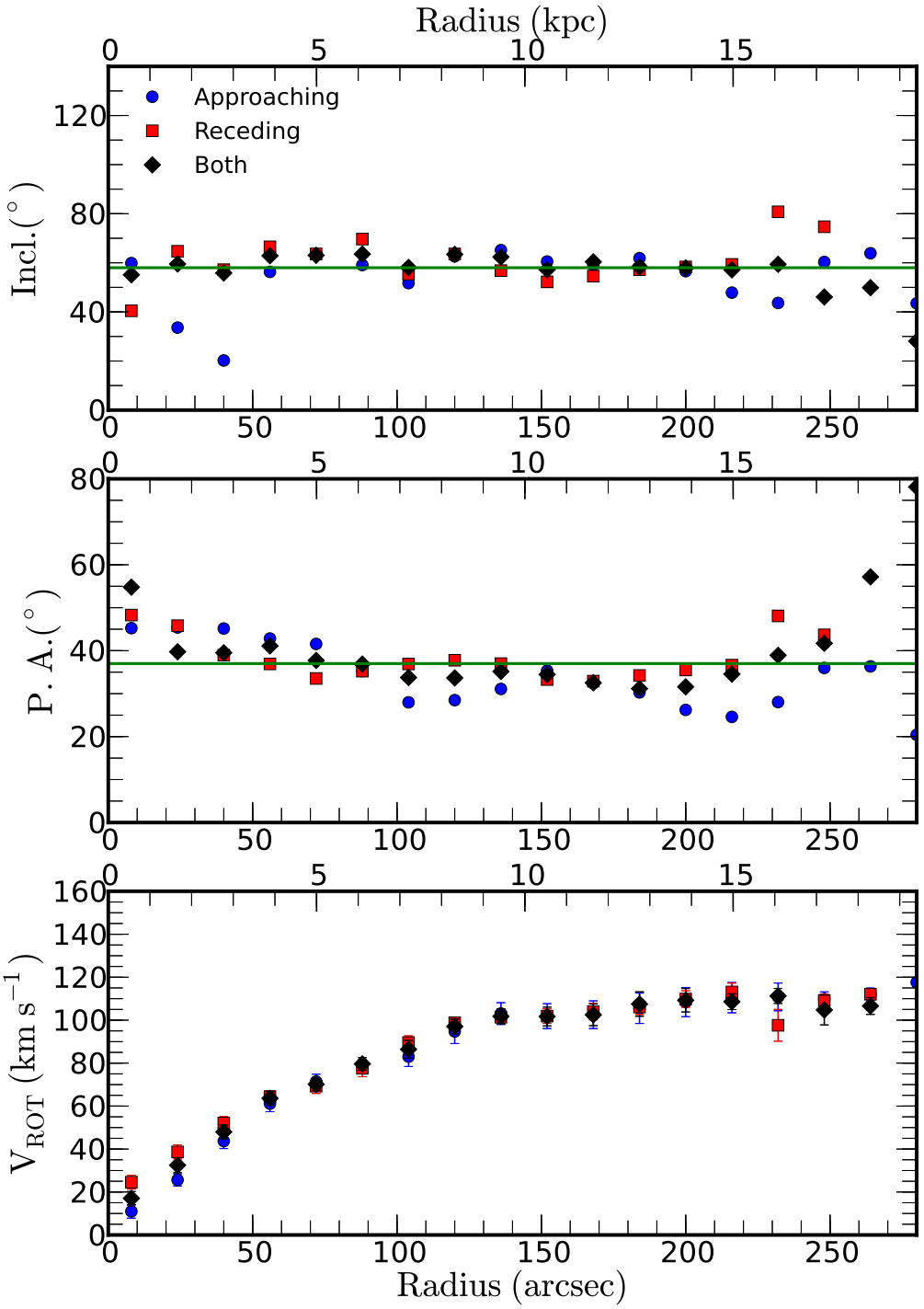

FIGURE 3.10: Tilted ring model results obtained with the GIPSY task ROTCUR. The variation of the inclination as a function of radius is shown in the top panel and the position angle (PA) variation in the middle panel. The RC presented in the bottom panel was obtained with all the kinematical parameters, including PA and the inclination, kept fixed to their average values. The results from the receding side are presented as red squares, those from the approaching side as blue circles and from both sides as black diamonds. The lines correspond to PA= 37º and i = 58º.

3.4.2 Model-based correction to the RC

As discussed in section 3.3, the RC is under-estimated when the bar is aligned with the major axis because of the gas streaming along the bar. Therefore, the effect of those non-circular motions need to be estimated, and a correction needs to be applied to the RC before it can be used for the mass models.

We introduce the following step to correct the RCs for the non-circular motion induced by the bar:

- The correction is derived from the differences between the expected RC of the model, which is calculated from the true gravitational potential of the modeled galaxy, and the observed RC measured using the tilted ring method (ROTCUR)
- The correction is scaled in terms of velocity using the V_{max} ratio, i.e. $(\frac{V_{max,object}}{V_{max,model}})$ and in terms of radius using the ratio between the disk scale lengths, i.e. $(\frac{R_{d,object}}{R_{d,model}})$ before being used to correct the RC of an actual galaxy.
- The modeled galaxy (model) and the actual galaxy (object) should have similar bar properties, the distance also have to be taken into account.

The correction is done using the following

$$V_{corrected} = V_{uncorrected} + correction \times \frac{V_{max,object}}{V_{max,model}} \tag{3.7}$$

where $\mathrm{correction} = \mathrm{V_{obs,model}} - \mathrm{V_{expected}}$, $V_{obs,model}$ is the observed velocities obtain from ROTCUR, $V_{expected}$ the expected circular velocites; $V_{corrected}$ and $V_{uncorrected}$ are the corrected and uncorrected rotation velocities of NGC 3319 respectively.

To apply the corrections, the data from the model were normalized by the optical scale length in radius and by the maximum velocity in velocities using the steps

described above. The data is then extrapolated to obtain the correction at a given radius. The distance of NGC 3319 is used to convert from angular scale into physical scale. Comparison between the corrected and uncorrected RC is shown in figure 3.11.

Despite the fact that NGC 3319 is classified as a SBcd galaxy, the gSb model presented at the bottom panel of figure 3.3 is used to derive the corrections. This is because the gSd model does not have a bulge component (see table 3.1) and that the bulge-to-disk (B/D) ratio of the gSb model obtained from the ratio between the bulge mass and disk mass given in table 3.1 $M_b/M_d = 0.239$ is very similar to the B/D = 0.24 of NGC 3319 estimated from the 3.6 micron surface brightness profile.

In this illustrated test case, we do not pretend to accurately correct for the non-circular motions induced by the bar. In the continuation of this work, we intend to match even more accurately the simulated galaxies to the actual galaxies. However, we think that the gSb simulation used is close enough to NGC 3319 to show clearly how not taking into account the effect of bars can lead to deriving very different parameters for the derived dark matter component. We still have to investigate if it is the best way to scale the model to the actual galaxies. However, this is surely close enough to serve the purpose of this study.

3.4.3 Mass model

3.4.3.1 Dark Matter Halo component

The distribution of DM is characterized by a density profile. The observationally motivated pseudo-isothermal halo (ISO) and the cosmologically motivated Navarro, Frenk and White (NFW) (Navarro, Frenk & White 1996) profiles are widely used. The mass model is done by comparing the observed RCs with the quadratic sum of the luminous and dark matter components using a chi-squared

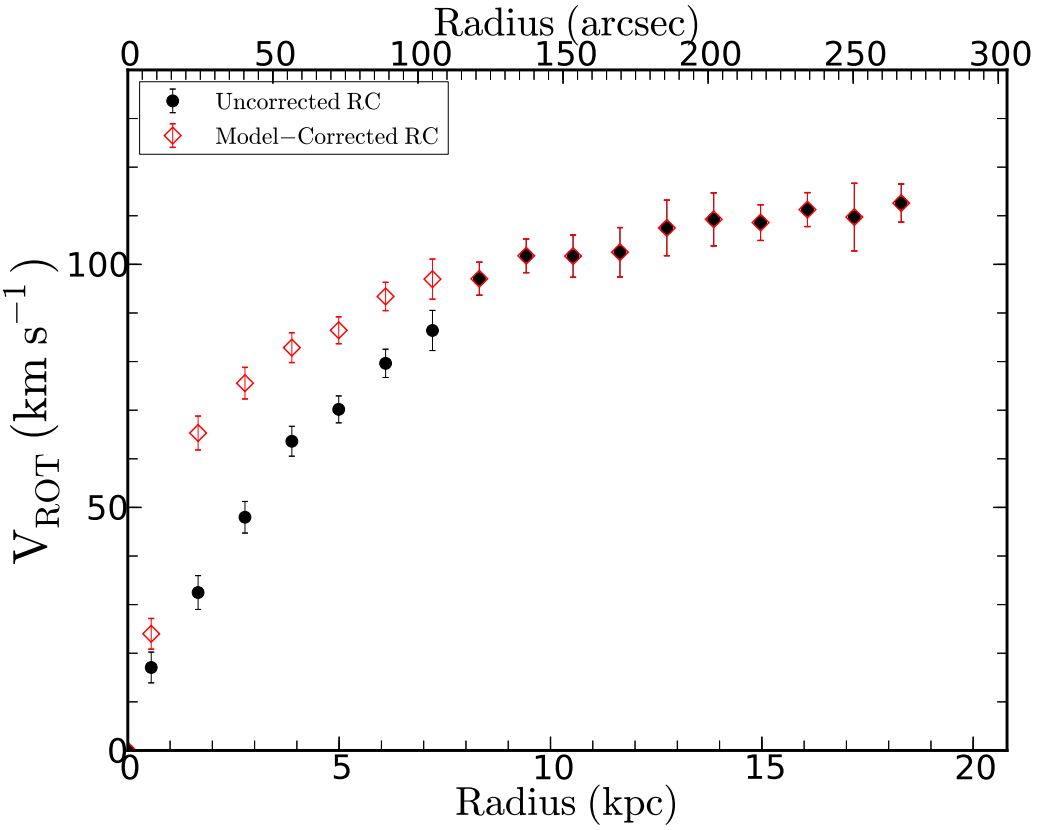

FIGURE 3.11: Comparison between the model-corrected and uncorrected RCs.

minimization technique. The mass models were carried out using the GIPSY tasks ROTMAS and ROTMOD.

The RC is given by:

$$V_{rot}^2 = V_{gas}^2 + V_*^2 + V_{halo}^2 \tag{3.8}$$

where V_{gas} is the gas contribution, V_* the stars contribution and V_{halo} the contribution of the dark matter component.

The pseudo-Isothermal (ISO) Dark Matter (DM) Halo Model

The pseudo-isothermal (ISO) dark matter halo is a core-dominated type of halo. The ISO density profile is given by:

$$\rho_{ISO}(R) = \frac{\rho_0}{1 + (\frac{R}{R_c})^2} \tag{3.9}$$

where ρ_0 is the central density and R_c the core radius of the halo. The velocity contribution of a ISO halo is given by:

$$V_{ISO}(R) = \sqrt{4\pi\ G\ \rho_0\ R_c^2(1 - \frac{R}{R_c}\ atan(\frac{R}{R_c}))} \tag{3.10}$$

We can describe the steepness of the inner slope of the mass density profile with a power law $\rho \sim r^{\alpha}$. In the case of the ISO halo, where the inner density is an almost constant density core, $\alpha = 0$.

The NFW DM Halo Model

The NFW DM halo profile was derived from cosmological simulations and it is commonly accepted in the ΛCDM framework. The NFW halo density profile is described by:

$$\rho_{\mathrm{NFW}}(\mathrm{R}) = \frac{\rho_{\mathrm{i}}}{\frac{\mathrm{R}}{\mathrm{R_S}}(1+\frac{\mathrm{R}}{\mathrm{R_S}})^2} \tag{3.11}$$

where $\rho_i \approx 3H_0^2/(8\pi G)$ is the critical density for closure of the universe and R_S is a scale radius. The velocity contribution corresponding to this halo is given by:

$$\mathrm{V_{NFW}(R)} = \mathrm{V_{200}}\ \sqrt{\frac{ln(1+cx) - cx/(1+cx)}{x(ln(1+c) - c/(1+c))]}} \tag{3.12}$$

where $\mathrm{V_{200}}$ is the velocity at the virial radius $\mathrm{R_{200}}$, $\mathrm{c} = \mathrm{R_{200}/R_S}$ gives the concentration parameter of the halo and x is defined as $\mathrm{R/R_S}$. The relation between $\mathrm{V_{200}}$ and $\mathrm{R_{200}}$ is given by:

$$\mathrm{V_{200}} = \frac{\mathrm{R_{200}} \times \mathrm{H_0}}{100} \tag{3.13}$$

where $\mathrm{H_0}$ is the Hubble constant taken as $\mathrm{H_0} = 72.0\ \mathrm{km\ s^{-1}\ Mpc^{-1}}$ (Hinshaw et al. 2009).

3.4.3.2 Luminous matter Components

Gas Contribution

The contribution from the gas is estimated from the moment0 maps. The task ELLINT is used to compute the HI gas density profile using the kinematic parameters obtained with ROTCUR. ELLINT divides the moment0 map into concentrated rings and estimates the density for each ring. The output from ELLINT is then used in ROTMOD to calculate the gas contribution in the mass model, assuming an infinitely thin disk. The profile was multiplied by 4/3 to take into account the primordial Helium contribution.

Stellar Contribution

The SPITZER 3.6 microns surface brightness profile is used to calculate the stellar contribution. Near-Infrared probes most of the emission from the old stellar disk population. It is also less affected by dust and therefore represents the bulk of the stellar mass. The data were retrieved from the SPITZER archive. After the foreground stars were removed, the images were fitted with concentric ellipses using the ELLINT task in GIPSY. The results were then converted into a surface brightness profile in mag/arcsec^2 using the method in Oh et al. (2008).

The surface brightness profile is corrected for inclination and galactic extinction before being converted into mass density. The method used by Oh et al. (2008) was also adopted to convert the luminosity profile into a mass density profile. The density profile is given by:

$$\Sigma[\mathrm{M_\odot pc^{-2}}] = \Upsilon_{*,3.6} \times 10^{-0.4\times(\mu_{3.6\mu} - \mathrm{C_{3.6}})} \tag{3.14}$$

where $\Upsilon_{*,3.6}$ is the stellar mass-to-light ratio in the 3.6 microns band, $\mu_{3.6}$ the surface brightness profile and $C_{3.6}$ is a constant used for the conversion from mag/arcsec^2 to $L_\odot$/pc^2. $C_{3.6}$ is given by:

$$\mathrm{C_{3.6}} = \mathrm{M_{\odot,3.6}} + 21.56 \tag{3.15}$$

where $M_{\odot,3.6}$ is the absolute magnitude of the Sun in the 3.6 microns band. Using the distance modulus formula and the distance to the Sun, Oh et al. (2008) found:

$$\mathrm{M_{\odot,3.6}} = \mathrm{m_{\odot,3.6}} + 31.53 = 3.24 \tag{3.16}$$

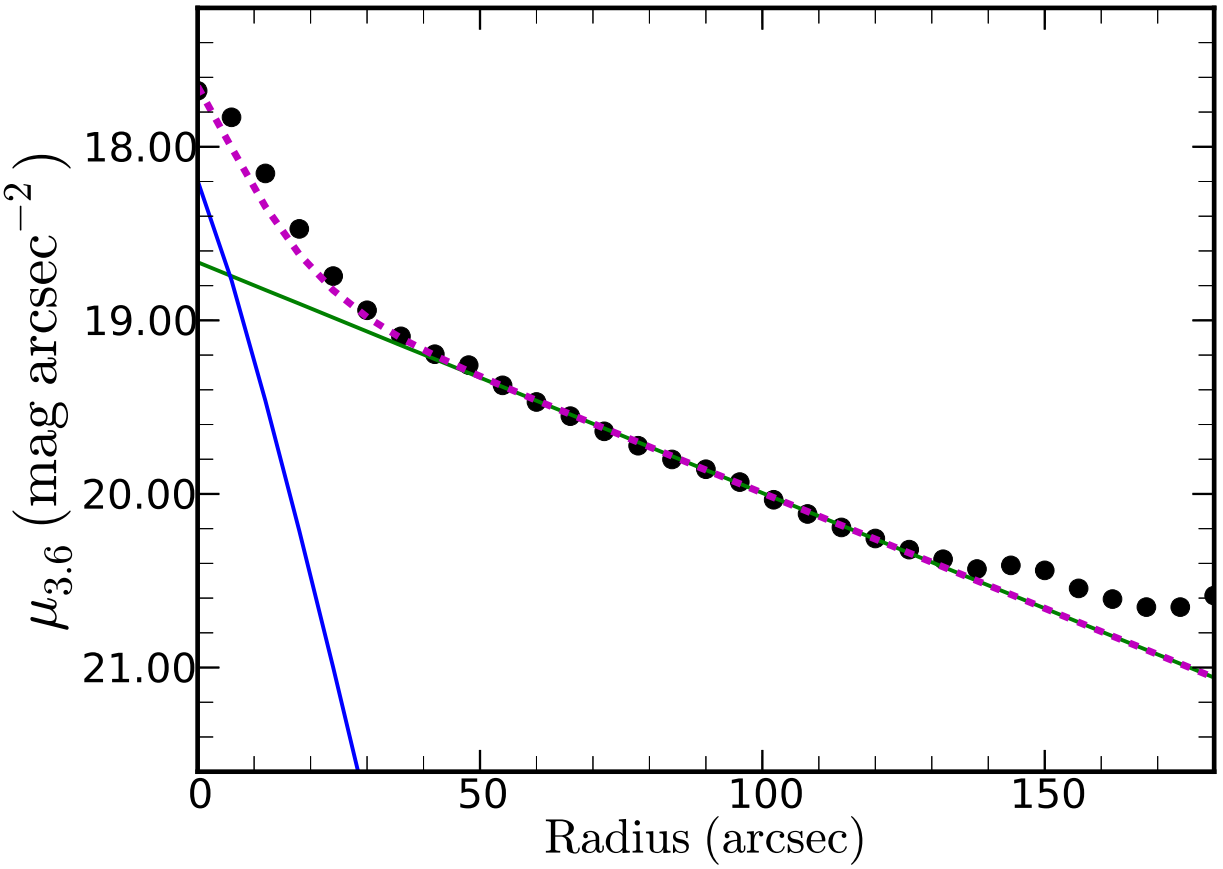

FIGURE 3.12: Bulge-disk decomposition, the green line is the best fit for the disk, the blue for the bulge and the dashed magenta line the sum of the contribution from both components.

The bulge-disk decomposition

The surface brightness profile in figure 3.12 clearly shows that this galaxy has a bulge in the center, thus a bulge-disk decomposition is needed to better constraint the contribution from the stellar component.

The disk component was fitted with an exponential disk using the following equation

$$\mu(r) = \mu_0 + 1.10857\frac{R}{R_d}, \tag{3.17}$$

where R_d is the disk scale length and μ_0 the central surface brightness. The remaining profile is fitted with a Sersic profile by letting the Sersic index n, the effective radius R_e and the effective surface brightness μ_e as free parameters. The bulge is therefore described by

$$\mu(r) = \mu_e + 2.5b_n[(\frac{R}{R_e})^{1/n} + 1], \tag{3.18}$$

where b_n = 1.9992n - 0.3271 for 0.5 < n < 10 (Capaccioli 1989) The best fit result shown in figure 3.12 gives R_d = 5.77 ± 0.06 kpc, μ_0 = 18.66 ± 0.02 mag for the disk and n = 0.87 ± 0.02, R_e = 2.04 ± 0.05 kpc and μ_e = 21.74 ± 0.31 mag for the bulge.

Mass-to-light ratio

The mass-to-light ratio (Υ_*) for the IRAC1 band is normally derived using the J-K color (see Oh et al. 2008, de Blok et al. 2008). However, this method gives a higher mass-to-light ratio for the disk component than the bulge component which is unphysical. de Denus-Baillargeon et al. (2013) uses chemo-spectrophotometric galactic evolution (CSPE) models to constrain the mass-to-light ratio of nearby galaxies as function of radius. We use their results to estimate the mass-to-light of NGC 3319. NGC 3319 and NGC 2403 have the same morphological type (SBcd) and similar maximum velocity but NGC 3319 has a larger bulge compared to NGC 2403. The values used for the mass model are given in table 3.3.

3.4.4 Results

The mass model results for the uncorrected and corrected RC s are presented in figure 3.13 for the ISO and NFW models. The observed RC is shown as filled black circles with error bars, the gas contribution as dashed green lines, the stellar disk contribution as dashed red lines, the stellar bulge contribution as long-dashed blue

lines and the contribution from the dark matter halos as dashed magenta lines. The continuous lines are the best-fit models to the RC. Table 3.3 summarizes the results for the ISO and NFW models. The columns are described as follows, the first column is the type of DM halo used, the second column gives the parameters of the fits, the third and fourth columns are the results. For the ISO models, the dark matter halo is much more centrally concentrated when the corrected RC is used with a $R_C \sim 1$ kpc compared to ~ 5 kpc for the uncorrected RC and a much larger ρ_0 (see table 3.3 for details). It is clear that the corrected and uncorrected RC give very different results for the dark matter parameters which shows the importance of those corrections for non-circular motions. The same is true for the NFW models where the concentration index c is five times larger when the corrected RC is used and R_{200} much smaller. Both the ISO and NFW models gives very good fits to the corrected RC with smaller χ^2_r. This confirms that the parameters of the dark matter halo are strongly affected by the non-circular motions induced by the bar, especially when the bar is aligned with the major axis. A large portion of the mass will be missed if the RC is not corrected and different conclusions could be drawn from the dark matter parameters. The difference between the uncorrected and corrected RC is still significant even after the bulge component has been taken into account. This is a clear demonstration that corrections must be applied to the observed RC so that it really represents the dynamical mass of barred systems.

3.5 Summary

We have presented the analysis of snapshot observations of N-body/hydrodynamic simulations of barred spiral galaxies with different bar strengths and orientations to quantify the non-circular motions induced by a bar. . In the simulations, the bar forms naturally due to gravitational instabilities. Therefore, snapshots of simulated galaxies spanning a wide range of bar strengths and bar orientations

Halo Model	Params	Uncorrected RC	Corrected RC
ISO	ρ_0	5.55±0.99	74.08±15.15
	R_c	6.91±1.11	1.34±0.16
	Υ_d	0.25	0.25
	Υ_b	0.40	0.40
	χ^2_r	1.35	0.75
NFW	c	0.43±0.01	5.18±0.73
	R_{200}	147.25±11.00	56.46±3.44
	Υ_d	0.25	0.25
	Υ_b	0.40	0.40
	χ^2_r	3.24	1.44

Notes: Υ_d is the mass-to-light ratio for the stellar disk and Υ_b for the bulge. The central DM density ρ_0 is given in units of 10^{-3} $M_\odot$ pc^{-3}; R_c and R_{200} are in kpc.

TABLE 3.3: Results for the ISO and NFW dark matter halo models using the uncorrected and corrected RCs.

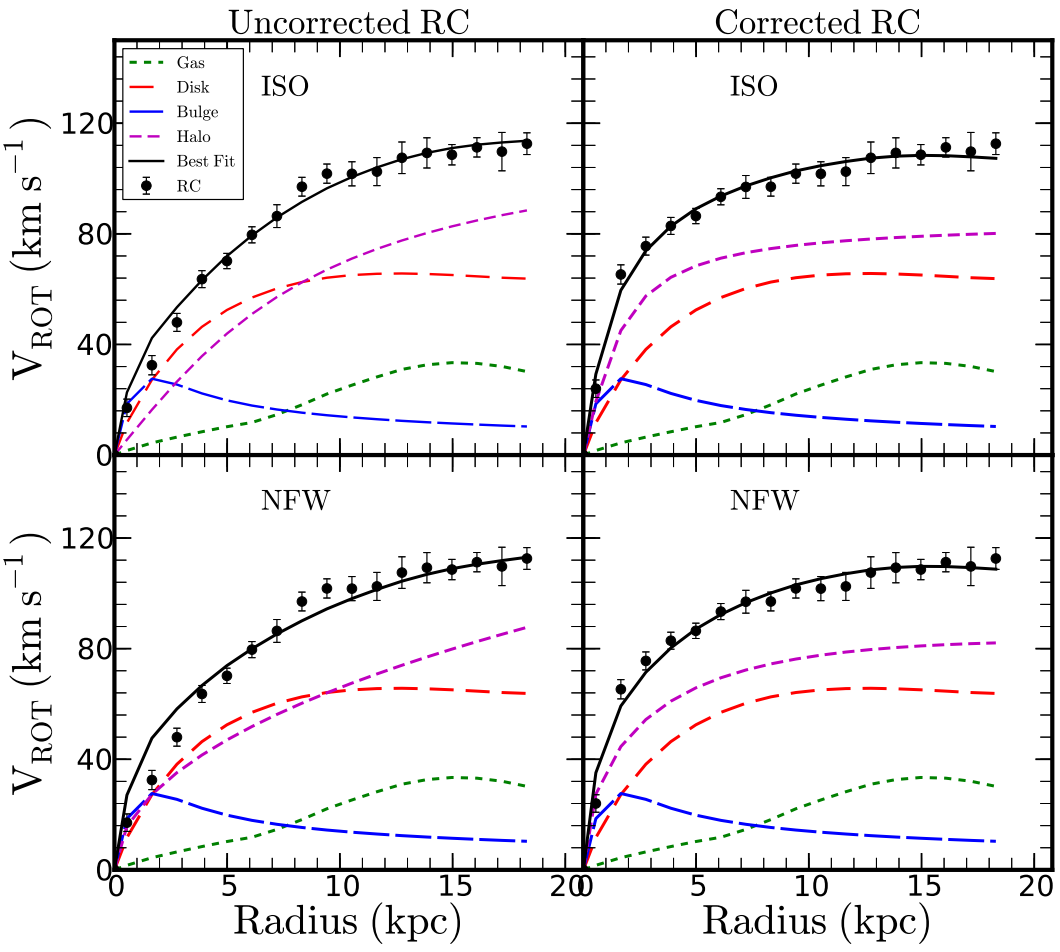

FIGURE 3.13: Mass models using ISO DM halo model (top) and NFW DM halo model (bottom) for the uncorrected (left) and model-corrected (right) RCs. Lines and symbols are shown on the top left corner of the first panel.

can be extracted and analyzed. Several models with different morphological types and dark matter halo distributions are analysed.

The results from the tilted ring method using ROTCUR show that the rotational velocities are largely under-estimated if the bar is parallel to the major axis and over-estimated if the bar is perpendicular except for an Sa galaxy which has an important central bulge for both simulations. This is consistent with Dicaire et al. (2008). This corresponds to the elongated orbits of the gas along the bar, which enhance the velocities at pericenter and reduce them at apocenter. Part of the gas and dust are moving alongside the bar which decreases the measured circular velocity when the bar is parallel to the major axis and increases it if the bar is aligned with the minor axis. The effect is smaller when the bar is in an intermediate position.

We also use DiskFit for our analysis. DiskFit is specifically designed to fit non-axisymmetric distortions from 2D velocity maps (Spekkens & Sellwood 2007). However, DiskFit works only when the bar is not aligned with the symmetry axes of the projected galaxy, and strong distortions are seen in the velocity field.

Sellwood & Sánchez (2010) noted that the circular velocity is biased low when the bar is parallel to the major axis (apocentre) since the gas follows an elliptical pattern and that the circular speed should be higher when the bar is aligned with the minor axis.

The test case in section 3.4 shows that the distribution of mass in NGC 3319 is very affected by the non-circular motions induced by the bar. For example, the central dark matter core is much more compact when the corrected RC is used. The ISO and NFW results are very different in all cases for the corrected and uncorrected RCs.

For future work, snapshot observations with different bar strengths and orientations will be studied to estimate the corrections that need to be applied to the observed rotation velocities of a sample of barred galaxies with a variety of bar

strength and bar orientation. A sample of barred galaxies with different bar sizes and orientations will be selected and modeled. This will help us to compare the results from the observations and the simulations for the individual galaxies.The main aim of this future work is to try to match as closely as possible the parameters of the model and the parameters of the galaxies, especially those of the bar. In particular, we will try to closely match the DM halo-to-luminous disk ratios.

Acknowledgments

We thank the anonymous referees for the comments and suggestions. CC's work is based upon research supported by the South African Research Chairs Initiative (SARChI) of the Department of Science and Technology (DST), the SKA SA and the National Research Foundation (NRF); ND and TR's work are supported by a SARChI's South African SKA Fellowship. We thank T. Jarrett for the Wise image.

3.6 APPENDIX

3.6.1 Numerical details about the simulations

The first simulation was done with a 3D Particle-Mesh code, based on FFT, with a useful grid of 128^3. The algorithm of James (1977) is used to suppress the Fourier images, and gain a factor 8 in memory. A total number of particles of 240 000 is distributed on the grid, and the density is computed with the cloud in cell algorithm (CIC). The gas is represented by sticky particles, colliding with inelastic collisions. At each encounter, the relative velocity of the clouds is multiplied by 0.65 in the radial direction, and 1 in the tangential direction, which keeps the angular momentum conserved.

The star formation is assumed to follow a Schmidt law, with exponent n=1.4, and a density threshold. It is calibrated for a gas consumption time-scale of 5 Gyr. We do not assume instantaneous recycling, but take into account a continuous mass loss, across Gyrs (Jungwiert et al. 2001). The mass loss by stars is distributed through gas on neighboring particles, with a velocity dispersion of 10km/s, to schematize the feedback energy.

The RCs are fitted to the observedtypical curves for these Hubble types. For these giant spiral galaxies, the total mass inside 35kpc is 2.4 10^{11} $M_\odot$, with 75% n DM and 25% baryons, for the standard model, and almost equality between baryons and DM for the disk-dominated (dmx) model. According to the Hubble types, Sa, Sb, Sd, the bulge to disk ratio is varied.

Similar simulations with TREE-SPH have also been run, with the same initial conditions (c.f. Di Matteo et al. 2007). In this code, gravitational forces are calculated using a hierarchical tree method (Barnes & Hut 1986) and gas evolution is followed by means of smoothed particle hydrodynamics (SPH, Lucy 1977; Gingold & Monaghan 1982). Gravitational forces are calculated using a tolerance

parameter $\theta = 0.7$ and include terms up to the quadrupole order in the multipole expansion. A Plummer potential is used to soften gravitational forces, with same softening lengths for all particle types, of 250pc. The code and the various validation tests were described in Semelin & Combes (2002). In the present study, we use the isothermal gas phase (gas temperature of 10^4K), adopted for the GalMer runs (Chilingarian et al. 2010). To capture shocks a conventional form of the artificial viscosity is used, with parameters $\alpha = 0.5$ and $\beta = 1.0$ (Hernquist & Katz 1989). Because of the short cooling time of disc gas, fluctuations in the gas temperature are quickly radiated away, so that simulations employing an isothermal equation of state are justified.

Star Formation and continuous stellar mass loss, together with supernovae feedback are taken into account. We parametrized the star formation efficiency for a SPH particle as $\frac{dM_{gas}}{dtM_{gas}} = C\rho^{1/2}$, with the constant C chosen such that the unperturbed giant disc galaxies form stars with a gas depletion time-scale of 2 Gyr. This is equivalent to a Kennicutt-Schmidt law of exponent 1.5.

To avoid to form too small stellar particles, we adopt the method of hybrid particles, where progressively the gas particles contain a stellar fraction for a certain time-scale, until the remaining gas fraction falls below 5%. Then the particle is transferred to the stellar component, and the gas is distributed over neighboring hybrid particles.

The stellar feedback is implemented both with stellar mass loss, and through supernovae. It is assumed that a percentage of 1% of the young stellar population is becoming a supernova, i.e. all stars more massive than 8 $M_\odot$, and the assumption of instantaneous recycling. The released mass also enriches the metallicity of the surrounding gas.

The stellar mass-loss at each time step, is accounted for by the method described by Jungwiert et al. (2001), and allows a more progressive metal enrichment of the interstellar medium.

3.6.2 Results from the SPH simulation

The dynamics of the gas in disk galaxies are very complex systems and difficult to reproduce in numerical simulations. Therefore, to test the influence of our assumptions on the gas treatment on our results, we have considered the same simulations, with the same initial conditions, but run with the TREE-SPH code, used in the GalMer data-base (cf Chilingarian et al. 2010). The main features of the SPH-tree code for this particular simulation and also our treatment of star formation and feedback, are described in the appendix 3.6.1. The gas, which was considered essentially as an ensemble of dense clouds, dissipating their kinetic energy in collisions, is now considered as a fluid with pressure forces and shocks. The simulations have twice more particles, and the softening length is twice smaller, so that the spatial resolution of the hydrodynamic is larger. The velocity maps and other results from the GalMer project is publicly available and can be downloaded from their website (`http://galmer.obspm.fr/`). Figures 3.14 and 3.15 display the results with the TREE-SPH code for the gSa and gSb galaxies, corresponding to figure 3.2 and 3.3 with the FFT-sticky particles code. The gas behaviour is different, as expected, but the global feature due to the bar, the perturbations of the RC, are similar. For the orientation where the bar is parallel to the line of sight, the discrepancy between the true circular velocity and the "observed" rotational velocity is even larger, since the spatial resolution is higher. In the FFT-sticky particles simulations, the high velocity gradient was a bit smoothed out. This is less visible, when the bar is perpendicular to the line of sight, which is a configuration reducing the "observed" velocity gradient. Therefore, this shows that using different simulation codes does not affect our results.

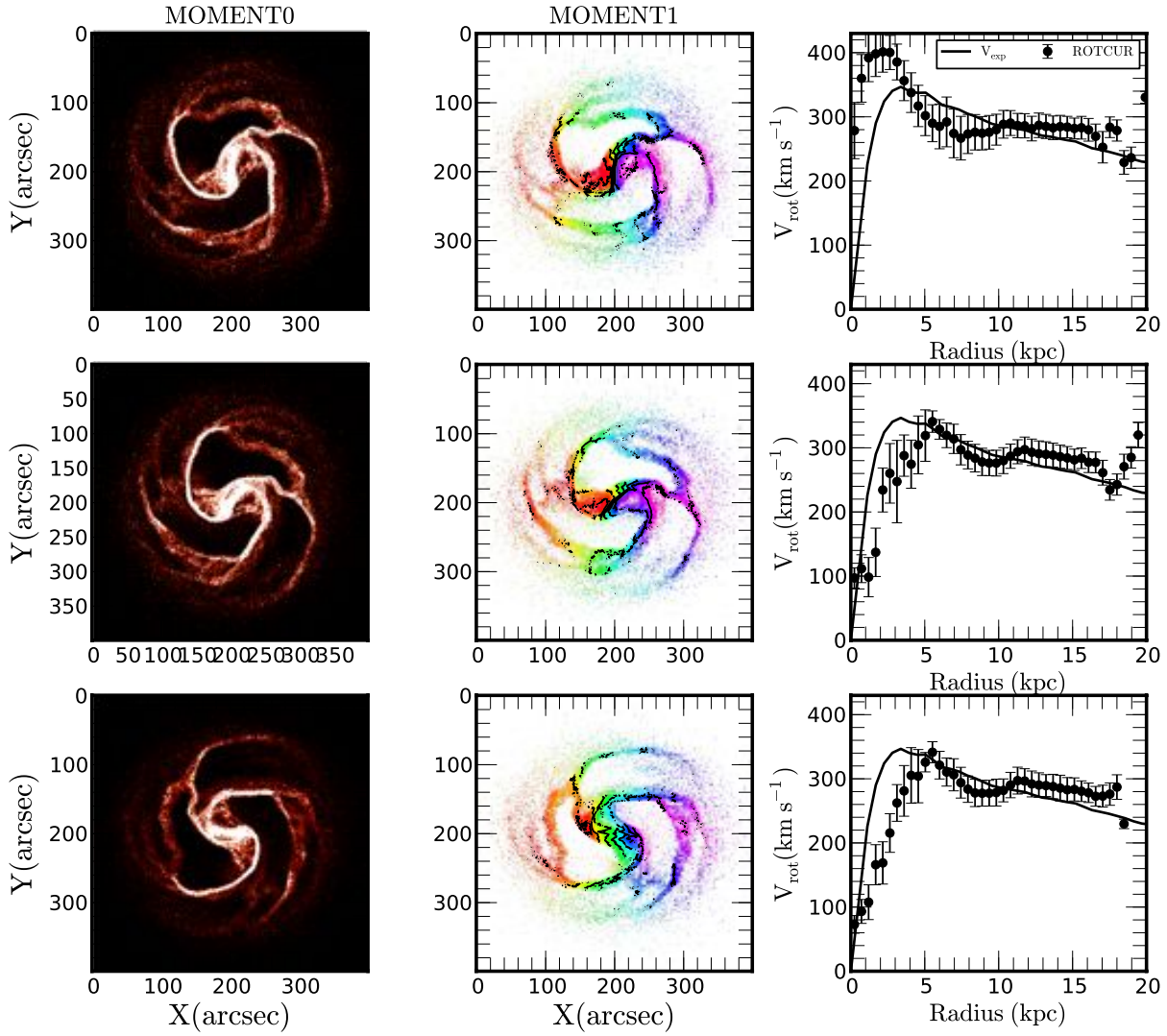

FIGURE 3.14: Three different bar positions for the model gSa (SPH simulation, T= 200 Myrs). Top panel: the bar is perpendicular to the major axis, middle panel: intermediate position and bottom panel: parallel to the major axis. The first column is the moment0 map, second column the moment 1 map superposed with the iso-velocity contours and the third column the comparison between the expected RCs shown as a continuous line and the measured rotational velocities derived using ROTCUR (black points).

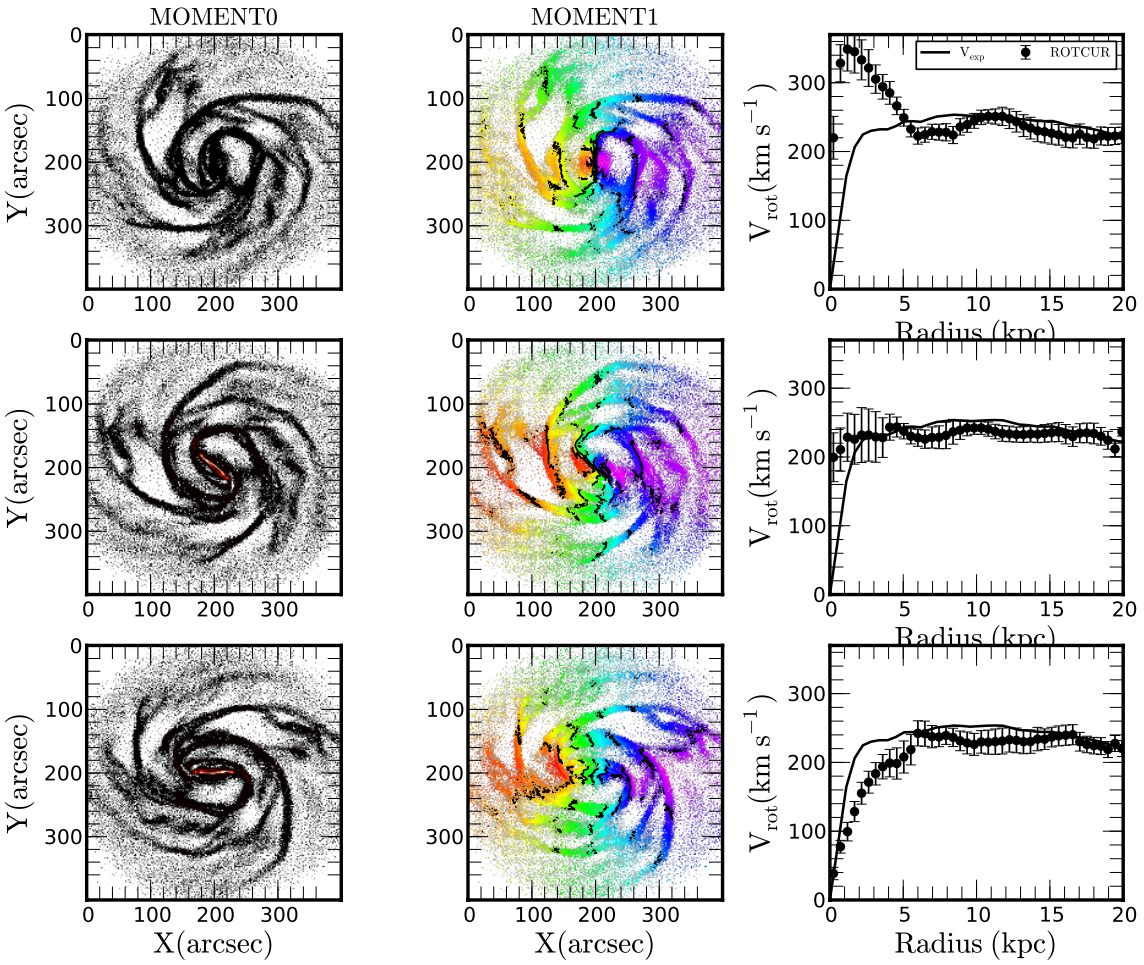

FIGURE 3.15: Three different bar positions for the model gSb (SPH simulation, T = 400 Myrs see figure 3.14 for details).

Bibliography

Allen, R. J., Ekers, R. D., Terlouw, J. P., & Vogelaar, M. G. R. 2011, Astrophysics Source Code Library, 9018

Aguerri, J. A. L., Méndez-Abreu, J., & Corsini, E. M. 2009, A&A, 495, 491

Athanassoula, E., & Misiriotis, A. 2002, MNRAS, 330, 35

Barazza, F. D., Jogee, S., & Marinova, I. 2008, Formation and Evolution of Galaxy Disks, 396, 351

Barnes, J., & Hut, P. 1986, nature, 324, 446

Begeman K. G., 1989, A&A, 223, 47

Blais-Ouellette, S., Amram, P., & Carignan, C. 2001, AJ, 121, 1952

Burkert, A. 1995, ApJL, 447, L25

Capaccioli, M. 1989, World of Galaxies (Le Monde des Galaxies), 208

Carignan, C. 1985, ApJ, 299, 59

Carignan C., Freeman K. C., 1985, ApJ, 294, 494

Chilingarian, I. V., Di Matteo, P., Combes, F., Melchior, A.-L., & Semelin, B. 2010, A&A, 518, A61

Combes, F. 2011, Memorie della Societa Astronomica Italiana Supplementi, 18, 53

Cote, S., Carignan, C., & Sancisi, R. 1991, AJ, 102, 904

de Blok W. J. G., Walter F., Brinks E., Trachternach C., Oh S.-H., Kennicutt, Jr. R. C., 2008, AJ, 136, 2648

de Denus-Baillargeon, M.-M., Hernandez, O., Boissier, S., Amram, P., & Carignan, C. 2013, ApJ, 773, 173

de Vaucouleurs G., de Vaucouleurs A., Corwin, Jr. H. G., Buta R. J., Paturel G., Fouqué P., 1991, Third Reference Catalogue of Bright Galaxies. Volume I: Explanations and references. Volume II: Data for galaxies between 0^h and 12^h. Volume III: Data for galaxies between 12^h and 24^h.

Dicaire, I., Carignan, C., Amram, P., et al. 2008, MNRAS, 385, 553

Di Matteo, P., Combes, F., Melchior, A.-L., & Semelin, B. 2007, A&A, 468, 61

Eskridge, P. B., Frogel, J. A., Pogge, R. W., et al. 2000, AJ, 119, 536

Einasto J., 1969, Astronomische Nachrichten, 291, 97

Gingold, R. A., & Monaghan, J. J. 1982, Journal of Computational Physics, 46, 429

Hernquist, L., & Katz, N. 1989, ApJS, 70, 419

Hinshaw, G., Weiland, J. L., Hill, R. S., et al. 2009, ApJS, 180, 225

Jungwiert, B., Combes, F., & Palouš, J. 2001, A&A, 376, 85

Jarrett, T. H., Masci, F., Tsai, C. W., et al. 2012, AJ, 144, 68

Jarrett, T. H., Chester, T., Cutri, R., Schneider, S. E., & Huchra, J. P. 2003, AJ, 125, 525

James, R.A. 1977: J. Comput. Phys. 25, 71

Knapen, J. H., Shlosman, I., & Peletier, R. F. 2000, ApJ, 529, 93

Kravtsov, A. V., Klypin, A. A., Bullock, J. S., & Primack, J. R. 1998, ApJ, 502, 48

Kuzio de Naray, R., Arsenault, C. A., Spekkens, K., et al. 2012, MNRAS, 427, 2523

Lucy, L. B. 1977, AJ, 82, 1013

Marinova, I., & Jogee, S. 2007, ApJ, 659, 1176

Marinova, I., Jogee, S., Barazza, F. D., et al. 2009, Galaxy Evolution: Emerging Insights and Future Challenges, 419, 138

Masters, K. L., Nichol, R. C., Hoyle, B., et al. 2011, MNRAS, 411, 2026

Menéndez-Delmestre, K., Sheth, K., Schinnerer, E., Jarrett, T. H., & Scoville, N. Z. 2007, ApJ, 657, 790

Méndez-Abreu, J., Sánchez-Janssen, R., & Aguerri, J. A. L. 2010, ApJL, 711, L61

Moore, E. M., & Gottesman, S. T. 1998, MNRAS, 294, 353

Milgrom M., 1983a, ApJ, 270, 371

Milgrom M., 1983b, ApJ, 270, 365

Milgrom M., 1983c, ApJ, 270, 384

Navarro J. F., Frenk C. S., & White S. D. M. 1996, ApJ, 462, 563

Oh, S.-H., de Blok, W. J. G., Walter, F., Brinks, E., & Kennicutt, R. C., Jr. 2008, AJ, 136, 2761

Sakai, S., Ferrarese, L., Kennicutt, R. C., et al. 1999, ApJ, 523, 540

Sellwood, J. A., & Sánchez, R. Z. 2010, MNRAS, 404, 1733

Semelin, B., & Combes, F. 2002, A&A, 388, 826

Spekkens, K., & Sellwood, J. A. 2007, ApJ, 664, 204

Randriamampandry, T. H., & Carignan, C. 2014, MNRAS, 439, 2132

Rogstad, D. H., Lockhart, I. A., & Wright, M. C. H. 1974, ApJ, 193, 309

van der Wel, A., Franx, M., van Dokkum, P. G., et al. 2014, ApJ, 788, 28

Whyte, L. F., Abraham, R. G., Merrifield, M. R., et al. 2002, MNRAS, 336, 1281

Chapter 4

Paper II: Exploring the GalMer database: bar properties and non-circular motions

This chapter have been published in the Astronomy and Astrophysics Journal; T. H. Randriamampandry, N. Deg, C. Carignan, F. Combes, and K. Spekkens A&A 594, A86 (2016)

Abstract

We use Tree-SPH simulations from the GalMer database to characterize and quantify the non-circular motions induced by the presence of bar-like structures on the observed rotation curve of barred galaxies derived from empirical models of their line-of-sight velocity maps. The GalMer database consists of SPH simulations of galaxies spanning a wide range of morphological types and sizes. The aim is to compare the intrinsic velocities and bar properties from the simulations with those derived from pseudo-observations. This allows us to estimate the amount of non-circularity and to test the various methods used to derive the bar properties and rotation curves. The intrinsic velocities in the simulations are calculated from the gravitational forces whereas the observed rotation velocities are derived by applying the ROTCUR and DiskFit algorithms to well-resolved observations of intermediate-inclination, strongly barred galaxies. Our results confirm that the tilted ring method implemented in ROTCUR systematically underestimates or overestimates the rotational velocities by up to 40 percent in the inner part of the galaxy when the bar is aligned with one of the symmetry axes for all the models. For the DiskFit analysis, we find that it produces unrealistic values for all the models used in this work when the bar is within approximately ten degrees of the major or minor axis.

4.1 Introduction

Bars are common features in disc galaxies, with nearly two thirds of nearby galaxies showing strong or weak bars (eg., de Vaucouleurs et al. 1991; Eskridge et al. 2000; Knapen et al. 2000; Marinova & Jogee 2007; Menéndez-Delmestre et al. 2007; Barazza et al. 2008; Aguerri et al. 2009; Marinova et al. 2009; Méndez-Abreu et al. 2010; Masters et al. 2011). These bars are dynamically important as they drive secular evolution by moving gas towards the galactic center (Athanassoula et al. 2013; Heller & Shlosman 1994; Shlosman & Noguchi 1993) and transfer angular momentum throughout the galaxy (Lynden-Bell & Kalnajs 1972; Weinberg 1985; Athanassoula & Misiriotis 2002; Marinova & Jogee 2007); thereby changing the kinematics of the gas and the properties of the galaxy in general.

Of particular importance is the effect of the bar on the velocity maps and rotation curves. Typically, the gas is assumed to be moving in circular orbits and its observed velocity is used to determine the mass distribution of galaxies (de Blok et al. 2008; Randriamampandry & Carignan 2014). This approximation works quite well for unbarred galaxies since the deviations from circular motion are small (Bosma 1978) but, in barred galaxies, the gas flows along the bar. Regan et al. (1999) using CO(1-0) emission-line observations found that the molecular gas in the inner part of barred galaxies is moving along the bar instead of in circular orbits. These flows are non-circular in nature and strongly affect rotation curves derived under the assumption of axisymmetry. Results from HI observations have also confirmed that the gas streaming along the bar produces large scale non-circular flows (Bosma 1978) on the observed rotation velocities. The precise effect of non-circular flows on the observed rotation curves depends on the orientation of the bar relative to the major axis of the observed disk (see e.g., Valenzuela et al. 2007; Spekkens & Sellwood 2007; Dicaire et al. 2008; Randriamampandry et al. 2015).

Hydrodynamic or N-body simulations are ideal to characterize and quantify these non-circular flows since the exact gravitational potential due to the mass is known for all the snapshots. In this work, a suite of N-Body simulations is used to quantify the size of the observed deviations and compare them to the intrinsic non-circularity found in the simulations. We have selected snapshots of isolated galaxies in the GalMer (Chilingarian et al. 2010) database that have the strongest bars in order to study the largest possible effects of the bar. In addition to the characterization and quantization of the non-circularity, we also test the ability of the DiskFit algorithm (Spekkens & Sellwood 2007) to recover the circular and non-circular components of the gaseous motion based on the observed velocity map.

The paper is organized as follows: a brief description of the GalMer database is given in Sect. 4.2. In Sect. 4.3, we describe the method used to measure the bar properties. In Sect. 4.4, we present the method used to characterize and quantify the non-circular motions, and the results are discussed in Sect. 4.5. Finally, in Sect. 4.6, we summarize the main results and highlight some possible future works.

4.2 The GalMer database

The GalMer database (Chilingarian et al. 2010) consists of a large set of Tree-SPH simulations of galaxies with different morphological types and sizes. The main objective of the GalMer project is to study galaxy evolution through mergers. It can also be used to study isolated galaxies by choosing the second galaxy pair as ”none”. The simulation results are publicly available and accessible online at `http://galmer.obspm.fr/`. The simulations are designed to cover a wide range of morphological types from giant ellipticals to dwarf spirals. The initial parameters of the GalMer models used are given in Table 1. The models used in this study are: the giant spirals (gSa, gSb and gSd) which are massive and large in size, the intermediate spirals (iSa, iSb and iSd) with medium sizes and masses and the

dwarf spirals (dSa, dSb and dSd) with low masses and small sizes. The models are classified as Sa, Sb and Sd galaxies depending on the importance of the bulge component and of the mass fraction (see Table 1). The Sa models have prominent bulge and lower gas fraction similar to early type spirals, the Sb models have smaller bulge but larger gas fraction than the Sa model and the Sd models are bulge-less with a gas fraction similar to late type spirals (See Chilingarian et al. 2010 for details). The snapshots with the strongest bars are shown in Fig. 4.1 for all nine models used in this work. The giants Sa, Sb and Sd are shown in the top panels, the intermediate or medium mass spirals in the middle panels and the dwarfs or low mass spiral in the bottom panels.

The GalMer database uses a go-on-the-fly algorithm which enables the user to obtain the masses, the velocity maps and other properties for every snapshot. The radial velocities maps are obtained by projecting the velocity components of each particle into a line-of sight (LOS) radial velocity assuming an infinite distance. The pixel size depends on the zoom that is chosen by the user on the online tool. The LOS radial velocity is given by:

$$V_r = V_X cos\varphi cos\theta + V_Y sin\varphi cos\theta + V_Z sin\theta, \tag{4.1}$$

where V_X, V_Y and V_Z are the velocity components for each particles, φ and θ are the azimuthal and polar angles respectively (Chilingarian et al. 2010).

The GalMer database does not provide the observed uncertainties for the mock velocity fields.

4.3 Bar properties

There are several methods used to determine the strength and size of a bar in the literature. The two most commonly used methods are ellipse fitting and Fourier

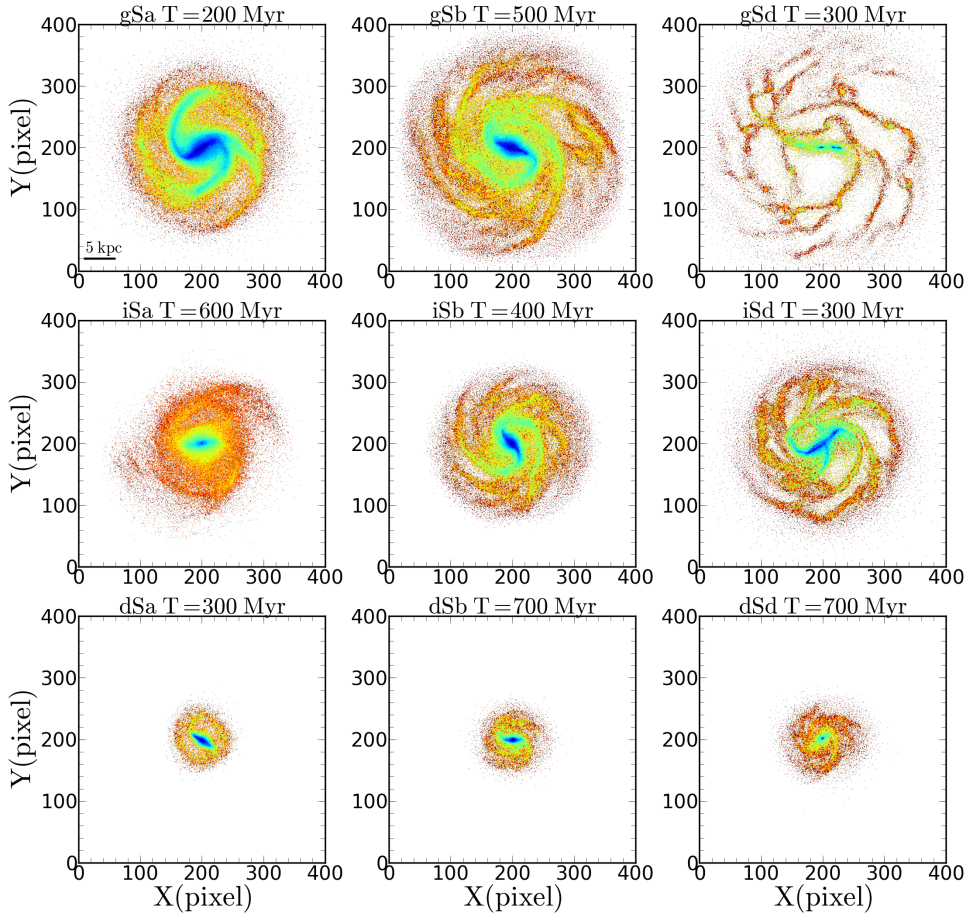

FIGURE 4.1: Gas and stellar distribution maps for the snapshots with the strongest bars as defined by their bar strengths and lengths. The giants Sa, Sb and Sd are shown on the top panels, the intermediate or medium mass on the middle panels and the dwarf or low mass spirals on the bottom panels. The pixel scale is 0.1 kpc using a zoom of 10 on the online tools (see `http://galmer.obspm.fr/`).

	M_{disc}	M_{bulge}	M_{gas}	M_{halo}	a_d	r_b	a_g	r_h	N. Stars	N. Gas	N. DM
Model	$10^9 M_\odot$	$10^9 M_\odot$	$10^9 M_\odot$	$10^9 M_\odot$	kpc	kpc	kpc	kpc			
1	2	3	4	5	6	7	8	9	10	11	12
gSa	92.0	23.0	9.4	115.0	4.0	2.0	5.0	10.0	80 000	240 000	160 000
gSb	46.0	11.5	9.4	172.5	5.0	1.0	6.0	12.0	160 000	160 000	160 000
gSd	57.5	-	7.5	172.5	6.0	-	7.0	15.0	60 000	20 000	40 000
iSa	46.0	11.5	4.6	57.5	2.8	1.4	3.5	7.0	40 000	120 000	80 000
iSb	23.0	5.7	4.6	86.2	3.5	0.7	4.2	8.5	80 000	80 000	80 000
iSd	28.7	-	8.6	86.2	4.2	-	5.0	10.6	120 000	40 000	80 000
dSa	9.2	2.3	0.9	11.5	1.3	0.3	1.6	3.8	8 000	24 000	16 000
dSb	4.6	1.2	0.9	17.2	1.6	0.3	1.9	3.8	16 000	16 000	16 000
dSd	5.7	-	1.7	17.2	1.9	-	2.2	4.7	24 000	8 000	16 000

TABLE 4.1: Initial parameters for the GalMer simulation from Chilingarian et al. (2010). The first column is the model, the second to fifth are the masses of the different components, followed by their scale lengths, and the last three columns are the number of particles for the stars, the gas and the dark matter halo components.

decomposition. Ellipse fitting is often used for observed galaxies, while Fourier decomposition is typically used for simulations.

Ellipse fitting consists of finding the set of iso-density (surface brightness) ellipses. The ellipticity of each ellipse is then used as a proxy for the bar strength as a function of radius. The largest value of the ellipticity, ϵ_{max}, is used to describe the overall bar strength while the bar length is taken to be the location of rapid changes in either the bar ellipticity of the surface brightness, or defined as the radius where there is a significant change of the position angle of the ellipses (eg., Díaz-García et al. 2016).

In Fourier decomposition, the image or density maps are modeled as a Fourier series (Salo et al. 2010):

$$a_m = \frac{1}{\pi} \int_0^{2\pi} \Sigma(r, \theta) cos(m\theta) d\theta, \tag{4.2}$$

$$b_m = \frac{1}{\pi} \int_0^{2\pi} \Sigma(r, \theta) sin(m\theta) d\theta. \tag{4.3}$$

The $m = 0$ and $m = 2$ components are calculated. Then the total second moment, A_2, is calculated as:

$$A_2(r) = \sqrt{a_2^2(r) + b_2^2(r)}. \tag{4.4}$$

The phase is found by :

$$\Phi_2(r) = arctan\left(\frac{a_2(r)}{b_2(r)}\right). \tag{4.5}$$

The total bar strength is given by the A_2/A_0 component and the bar length is found by either a large dip in surface brightness or a large change of phase (Laurikainen et al. 2004, 2005). This method has been applied to determine the bar length using the mass distributions of N-body simulations (e.g., Debattista & Sellwood 2000), and using images obtained from observations (e.g., Aguerri et al. 1998, 2003).

4.4 Characterization of non-circular motions

4.4.1 Different forms of non-circular motions

The amplitude of non-circular motions varies between galaxies. These motions complicate the study of the dynamics of gas in disc galaxies and diminish the usefulness of the rotation curves derived assuming axisymmetry. These motions are usually less than 20 $\mathrm{km\,s^{-1}}$ in magnitude (Bosma 1978) and vary in azimuthal phase relative to the disk major axis so that the overall impact on rotation curves is typically small. Other large scale deviations from circular motion can be divided into three types. The first is a kinematic warp: in this case, the PA and inclination changes with radius(see Christodoulou et al. 1993; Józsa 2007). The commonly used package ROTCUR (Begeman 1989) allows these parameters to vary as a function of radius which make it ideal to deal with this type of non-circular motion. The second type is large scale asymmetries due to tidal interactions with another galaxy. This produces an unusual shape of the outer part of the HI distribution that typically requires detailed simulation to decipher (eg, Gerhard & Fall 1983; Oh et al. 2015). The third type, which we are interested in, is the non-circular motion induced by a bar-like structure which is also known as oval or bar distortions (eg., Spekkens & Sellwood 2007). In this case, the deviation from circular flows is due to the gas streaming along the bar.

4.4.2 Non-circular motions within the simulations

The true rotation velocities (expected rotation curve) at a given radius can be obtained from the gravitational potential and its derivatives in the simulation by computing the average forces. The expected circular velocity is given by:

$$< V^2_{expected} >= r < \frac{\partial \Phi}{\partial r} >= r < F_r >, \tag{4.6}$$

where F_r is the radial force from the particles calculated azimuthally on a grid and Φ is the gravitational potential . A grid of concentric rings divided into angular bins is used in order to increase the force calculation speed.

The intrinsic non-circular components of the gas velocities can be determined a number of ways. A simple approach is to bin the gas particles in radial and angular bins and calculate the differences between the flow within a cell and the expected RC. These can then be used to calculate the rms for the tangential and radial velocities as a function of radius.

A slightly more elegant approach is to calculate the $m = 0$ and $m = 2$ Fourier moments for both the tangential and radial velocities. This allows a comparison between the strength and orientation of the velocity moments and the mass moments. It is also particularly useful because the DiskFit algorithm (see Sec. 4.3.2), breaks down the observed velocity map into non-circular radial and tangential components that are similar to the intrinsic Fourier moments.

The Fourier components are given by:

$$V_t(r,\theta) = A_{0,t}(r) + \sum_{m=1}^{\infty} A_{m,t}(r) cos[m\theta + \theta_{m,t}(r)], \tag{4.7}$$

$$V_r(r,\theta) = A_{0,r}(r) + \sum_{m=1}^{\infty} A_{m,r}(r) cos[m\theta + \theta_{m,r}(r)], \tag{4.8}$$

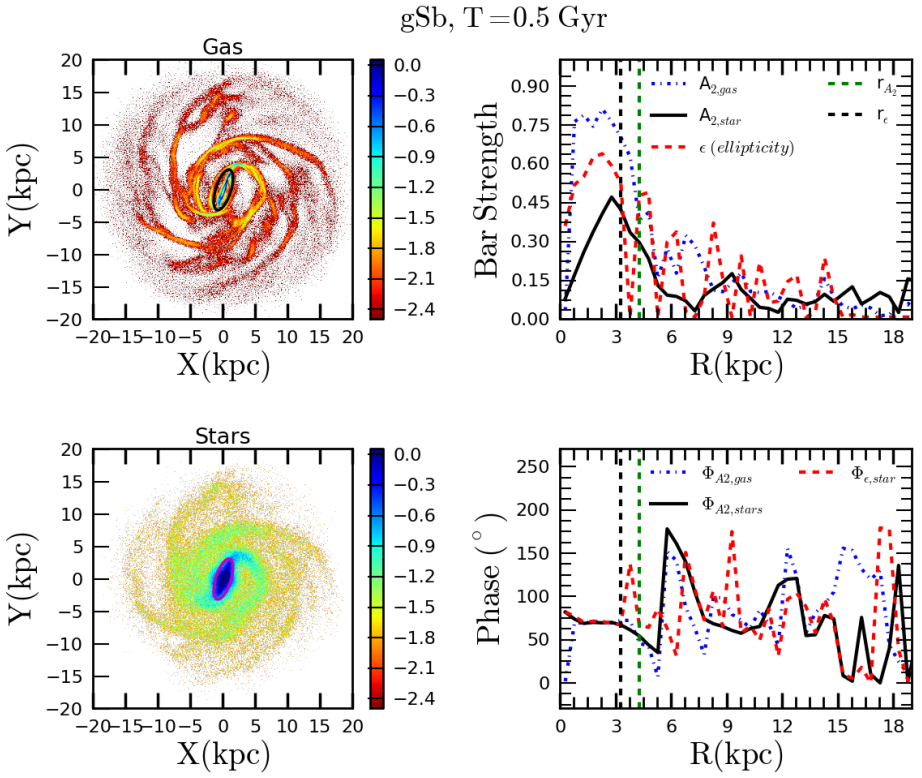

FIGURE 4.2: Example of bar properties calculation for the gSb model. The gas density map in arbitrary unit is shown in the top left panel and the stellar density map in the bottom panel. Comparison between the radial variation of the Fourier amplitudes A_2 derived from the gas density map (dotted blue line), the stellar density map (continuous black line) and the ellipticity obtained by fitting ellipses to the stellar map (dashed red line) are shown in the top right panel. The phases are shown in the bottom right panel, lines and symbols are the same in both panels. The vertical dashed green line is the bar length estimated from the Fourier amplitudes, r_{A2}, and the vertical black dashed line is the bar length estimated from the ellipticity, r_ϵ. The ellipse in the center of each map shows where the bar are located.

where $A_{m,t}(r)$ and $A_{m,r}(r)$ are the tangential and radial Fourier m^{th} velocity moments respectively, θ, $\theta_{m,t}(r)$ and $\theta_{m,r}(r)$ are the angular phases.

4.4.3 Non-circular motions from mock observations

4.4.3.1 Tilted ring analysis

Generally , the observed velocities are described as

$$V_{obs} = V_{sys} + V_c(r)sin(i), \tag{4.9}$$

where V_{sys} is the systemic velocity and i is the inclination angle. ROTCUR (Begeman 1989) is widely used to extract V_c from velocity maps.

The harmonic decomposition, pioneered by Franx et al. (1994), has been implemented into the GIPSY task RESWRI. This task is ideal for small scale departure from circular motions but not for large non-circular flows such as those induced by a bar. We do not include higher order harmonic components in the tilted ring analysis carried out in this work.

4.4.3.2 DiskFit analysis

Spekkens & Sellwood (2007) adopted a different approach when dealing with large scale non-circular motions induced by bars. Their method is based on modeling the tangential and radial components of the velocity at a given point as a Fourier series and by assuming that the non-circular flow is caused by a bar and that the non-axisymmetric distortion can be described by the m=2 radial and tangential Fourier moment.

The DiskFit algorithm is designed to account for non-circular flows such as bi-symmetric distortion, kinematic warp and lopsidedness (see Spekkens & Sellwood 2007 for details).

For a bi-symmetric flow from a bar the velocity map is modeled using:

$$\begin{aligned} V_{model} = V_{sys} + sin(i)[V_t cos(\theta) - V_{2,t} cos(2\theta_b) cos(\theta) \\ -V_{2,r} sin(2\theta_b) sin(\theta)] \ , \end{aligned} \tag{4.10}$$

where V_t is the circular velocity, $V_{2,t}$ and $V_{2,r}$ the amplitudes of the tangential and radial component of the noncircular motions for a bi-symmetric flow model, and θ and θ_b are the angle in the disk plane relative to the projected major axis and angle relative to the bar axis respectively (see Spekkens & Sellwood 2007).

DiskFit uses a bootstrap method to estimate the uncertainties on the parameters using χ^2 minimization technique:

$$\chi^2 = \sum_{n=1}^{N} \left(\frac{V_{obs}(x,y) - \sum_{k=1}^{K} \omega_{k,n} V_k}{\sigma_n}\right)^2, \tag{4.11}$$

where $V_{\rm obs}$(x,y) is the observed velocity at the position (x,y) on the sky, σ_n is the uncertainty, the K elements of V_k are the values of the tabulate velocity profiles in the model, $\omega_{k,n}$ is a weighting function which includes the trigonometric factors and also defines an interpolation scheme for the projected model (Spekkens & Sellwood 2007; Sellwood & Sánchez 2010).

4.5 Discussion of the results

The bar properties and the effect of the non-circular motion on the rotation curves are discussed in this section. The bar properties (bar strength and bar radius) obtained directly from the simulations and from the images are compared in section 4.5.1. In order to see the effect of the bar more clearly, we select the snapshot from each of the nine isolated galaxy runs that has the strongest bar (see Fig 4.1). We make mock observations of each snapshot with different bar orientations at a constant inclination of 60 degrees and a pixel size of 0.1 kpc. Each snapshot was then analyzed using both ROTCUR and DiskFit. DiskFit returns both the inferred circular and non-circular motions, while ROTCUR only returns the circular

component. Therefore, we define the non-circular motions from ROTCUR as:

$$V_{NCM} = V_{ROTCUR} - V_{expected} \tag{4.12}$$

The ROTCUR analysis is discussed in section 4.5.2.1 and the DiskFit analysis in section 4.5.2.2.

4.5.1 Bar properties: simulation vs observations

An example of the simulation analysis is shown in Fig. 4.2. The left-hand panels show the gas (upper) and stellar (lower) surface densities for the gSb snapshot. The right-hand panels show the intrinsic bar strengths and orientations using the Fourier and ellipse fitting methods. There **is** a number of interesting things to note in Fig. 4.2. Firstly, the gas and stellar bars are different. The gas bar is significantly stronger, but they both have similar bar lengths. This is most likely due to the gas' increased sensitivity to the bar's perturbations because of its lower velocity dispersion. Secondly, the ellipse fitting analysis gives a shorter bar. This is due to the Fourier method including similarly oriented spiral structure at larger radii. The ellipse method more accurately determines the switch from the bar to the spiral structure. Aguerri et al. (2009) argued that the ellipse fitting method could under-estimate the actual bar length, and the difference between the bar length estimated from the Fourier and ellipse fitting technique could also depend on the bar surface brightness profile. The shorter bar obtained from the ellipse fitting technique has also been noticed by other authors (e.g, Erwin 2005; Michel-Dansac & Wozniak 2006).

In addition, the value of ϵ is larger than A_2/A_0 for the stars across the extent of the bar. However, this does not indicate a disagreement regarding the bar strength, because the two quantities are determined using radically different methods. The

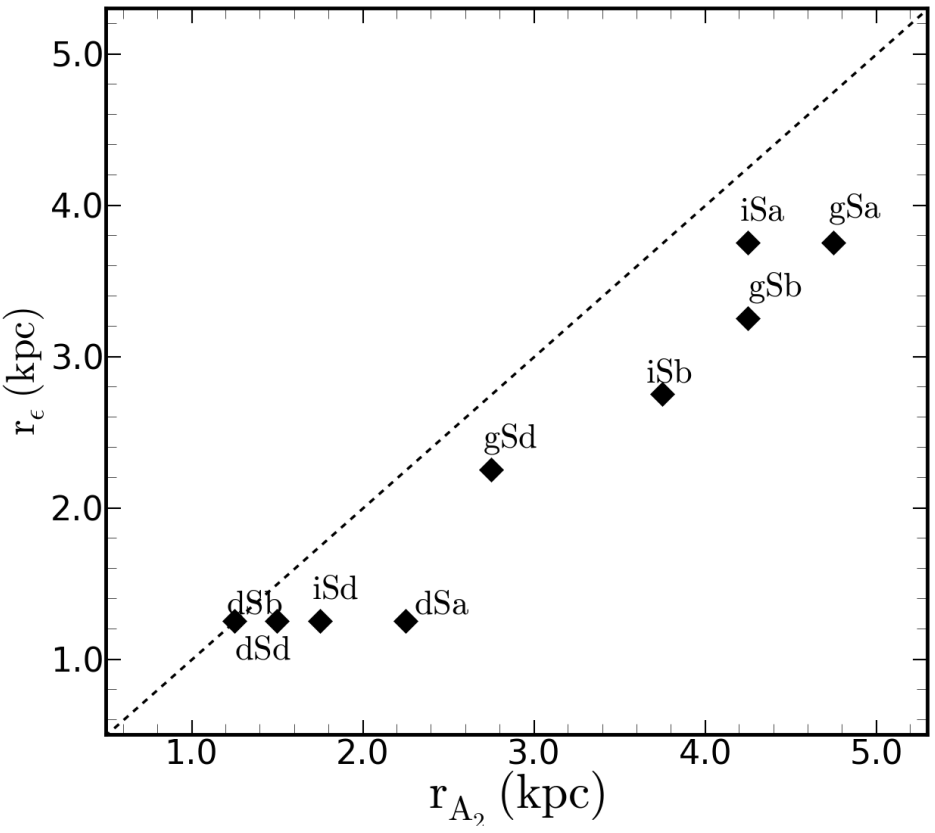

FIGURE 4.3: Comparison between the intrinsic bar radii obtained using the Fourier decomposition and the ellipses fitting methods estimated from the simulation. The dashed line is the one to one line.

Fourier method draws concentric circular rings and calculates the Fourier moments, while the ellipse fitting method attempts to draw iso-density ellipses. Fig. 4.3 shows comparison between the bar radii estimated from the ellipse fitting to those obtained from the Fourier decomposition for all the models. The bar radii estimated from the ellipse fitting are shorter than those obtained from the Fourier decomposition as illustrated in the example in Fig. 4.2.

Fig. 4.4 shows comparisons between the simulated and observed bar strengths and radii using the nine snapshots. This figure shows that the measured bar properties estimated within the simulation are similar to those obtained from pseudo-observations using stellar images.

4.5.2 Non-circular motions

A sample of the velocity flows found in the simulations is shown in Fig. 4.5. The upper left and middle panels show the binned velocity flows for the tangential and radial velocities respectively and the lower left and lower middle panels show the corresponding Fourier models. The upper right panel shows the expected rotation curve and compares it to the average tangential velocity flow and the $m = 0$ Fourier moment. This panel shows that the average velocity, the Fourier moment, and the expected rotation curve are all in agreement. The lower right panel shows the non-circular radial and tangential velocities calculated either using the rms method or the Fourier moments. In this case, the Fourier measure is slightly larger than the rms measurement. This result is easily understood through the method used. The $m = 2$ Fourier moments should equal the maximum deviation from circular motion, while the rms measure should be smaller as it averages the square of the deviations throughout the ring.

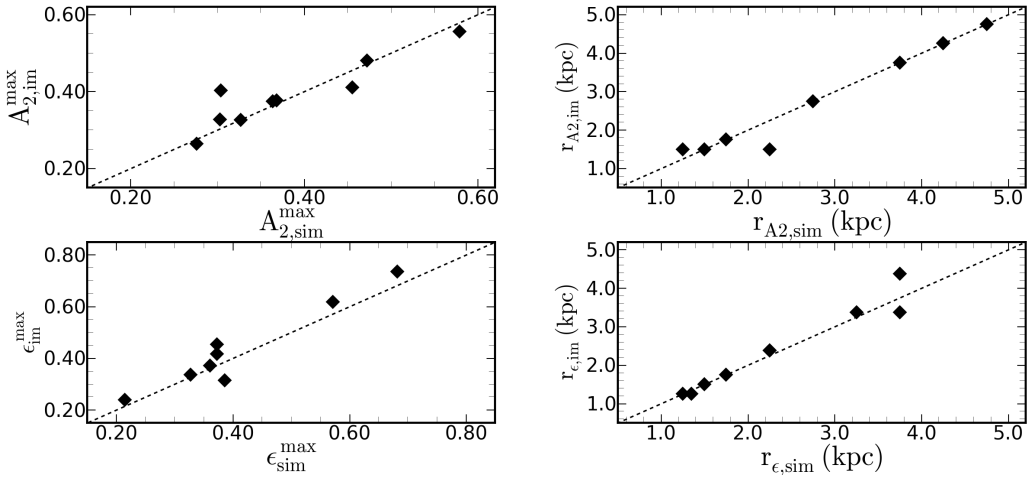

FIGURE 4.4: Comparison between the bar properties estimated within the simulation to those from images obtained from pseudo-observations. The maximum Fourier m=2 amplitude estimated within the simulation is plotted against those obtained from images on the top left panel. Comparison between the maximum ellipticity measured within the simulation and from images is shown on the bottom left panel. The right panels show comparison between the bar radius estimated within the simulation with those measured from images, the bar radius obtained using the Fourier method is on the top panel and those obtained using the ellipse fitting technique on the bottom panel.

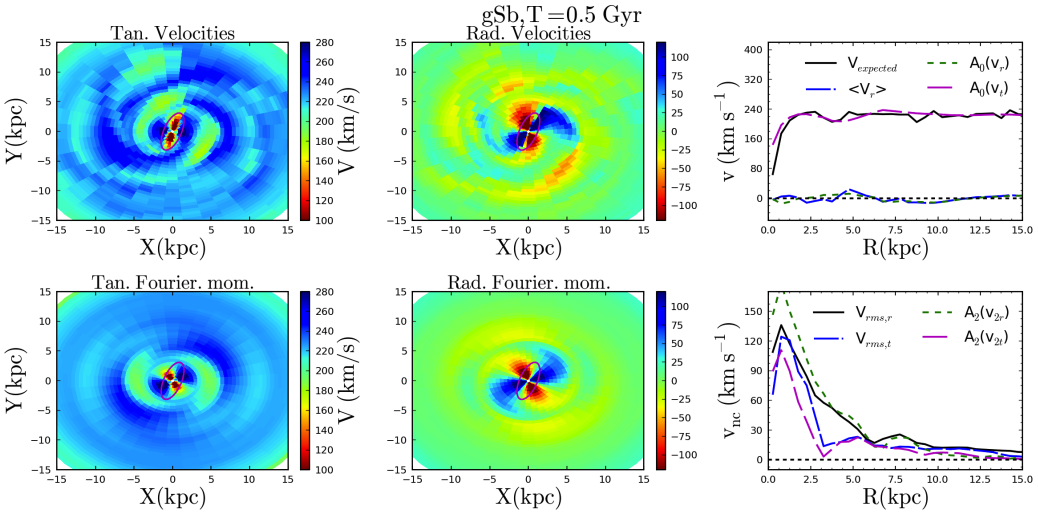

FIGURE 4.5: Example of the "intrinsic" rotation curve calculation for the gSb model. **First column:** the tangential velocities map is shown in the top panel and the tangential Fourier moments map in the bottom panel. **Second column**: the radial velocities map is shown in the top panel and the radial Fourier moment map in the bottom panel. **Third column**: the top panel shows the comparison between the expected circular velocities $V_{expected}$ calculated from the gravitational potential as a solid black line and the Fourier $A_0(V_t)$ as a long-dashed magenta line. The expected and Fourier axisymmetric radial velocities are shown as solid blue and dashed green lines, respectively. The non-circular velocities as a function of radius are plotted in the bottom panel. The continuous black line and the long-dashed blue line are the rms velocities estimated from the residual maps, and the dashed lines are the m=2 Fourier components. The ellipse in the center of each map shows the location and orientation of the bar.

4.5.2.1 ROTCUR analysis

The rotation curves are derived from the velocity maps downloaded from the GalMer database. The bar orientation angle was varied between 0° and 90° for each snapshot. Fig. 4.6 shows the deviations of the ROTCUR rotation curves from the expected rotation curve as a function of radius for the snapshots with the strongest bar for the gSb, iSb and dSb models. The ROTCUR rotation curves agree with the expected curve at approximatively 1 bar length, however they slightly increase between 1 and 2 bar lengths due to the perturbation caused by the spiral arm structures before returning to the true rotation curve at 2 bar lengths. Beyond 2 bar lengths, the curves all agree with the expected curve. The projected bar PA is shown in the top corner of each panel. The vertical dashed lines show 0.5, 1 and 2 bar radius. The Fig. 4.6 implies that the rotation curves measured using ROTCUR are smaller than the expected rotation curves inside the bar radius when the bar PA is less than 40° and larger than the expected velocities when the projected bar orientation is larger than 60°.

Fig. 4.7 shows the variation of the rotation curve error, which is the difference between the ROTCUR rotation curve and the expected rotation curve normalized by the expected rotation curve as a function of radius for nine different bar orientations. The velocity at R=0.5r_{bar} is used to estimate the rotation curve error. This often corresponds to the maximum ellipticity ϵ_{max}(Michel-Dansac & Wozniak 2006). The magnitude of the rotation curve error is zero or very small when the bar is oriented at 45° from the major axis. The velocity at half the bar length is more than 40% larger than the expected value when the bar is perpendicular to the major axis, and 40% smaller when the bar is parallel to the major axis. There seems to be a systematic increase or decrease of the velocities derived by ROTCUR at half the bar radius depending on the orientation of the bar. This has been previously investigated in the literature (see e.g., Spekkens & Sellwood 2007). The reason for ROTCUR under or over-estimating the velocities is that

when the bar is aligned with the major axis, most of the gas and stars are found at the apocenter of their elliptical orbits at each radius near the major axis. This gas is moving more slowly than it would if it was moving in circular orbits, and the rotation curve is under-estimated if this effect isn't taken into account. Conversely, bars that project along the minor axis place gas and stars close to the epicenter along the major axis, which implies that the rotation curve will be over-estimated if bar-like flows are ignored (Spekkens & Sellwood 2007). This shows the importance of using a specifically designed packages such as DiskFit when deriving the rotation curves of barred galaxies.

4.5.2.2 DiskFit analysis

DiskFit (Spekkens & Sellwood 2007) is specifically designed to account for non-circular motions induced by bars. However, it is well known that the DiskFit algorithm fails when the bar is parallel or perpendicular to the major axis of the galaxy (Sellwood & Sánchez 2010; Randriamampandry et al. 2015). This failure is due to a degeneracy in equation (10) for $\theta_b = 0$ or 90deg. The inclination, disk PA, disk kinematic center (xc, yc) and bar PA were allowed to vary during the fits. The systemic velocity V_{sys} is fixed to zero. A bi-symmetric distortion model (m=2) is considered up to R=2.5r$_{bar}$, then the non-axisymmetric flows are set to zero beyond this radius. The disk inclinations and PAs derived from DiskFit are in agreement with the expected values within the error bars. Fifty bootstraps were used to estimate the uncertainties on the parameters.

Fig. 4.8 shows a sample DiskFit analysis for the gSb snapshot with a bar angle of approximatively 45°. The observed velocity field is in the top left panel, the DiskFit bi-symmetric model is shown in the top right panel and the residual velocity (data-model) is in the bottom left panel. Only a few pixels in the innermost part of the residual map have values larger than 40 $\mathrm{km\,s^{-1}}$.

Comparisons between the Fourier amplitudes and the DiskFit velocities for the Sa, Sb and Sd models are shown in Figs. 4.9, 4.10 and 4.11 respectively. The ratio $\Delta V_t = (V_t - A_{0,t})/A_{0,t}$ is plotted in the top panel, $\Delta V_{2r} = (V_{2r} - A_{2,r})/A_{2,r}$ in the middle panel and $\Delta V_{2t} = (V_{2t} - A_{2,t})/A_{2,t}$ in the bottom panel. The shaded gray area shows where DiskFit fails to recover the bar orientation or velocities, or where the uncertainties on the returned parameters are large, which is about 10° from the symmetry axes. There is a number of interesting things to note in these figures. Firstly, DiskFit successfully recovers the rotation curve and the non-circular components for all the models for the bar orientations ranging between 10° and 80°. Unlike the ROTCUR analysis, there is no systematic under or over estimation of the velocities. There is a larger scatter in the inferred non-circular moments. However, the scatter may be due to the resolution of the velocity maps and more work is required before any definite conclusions are reached.

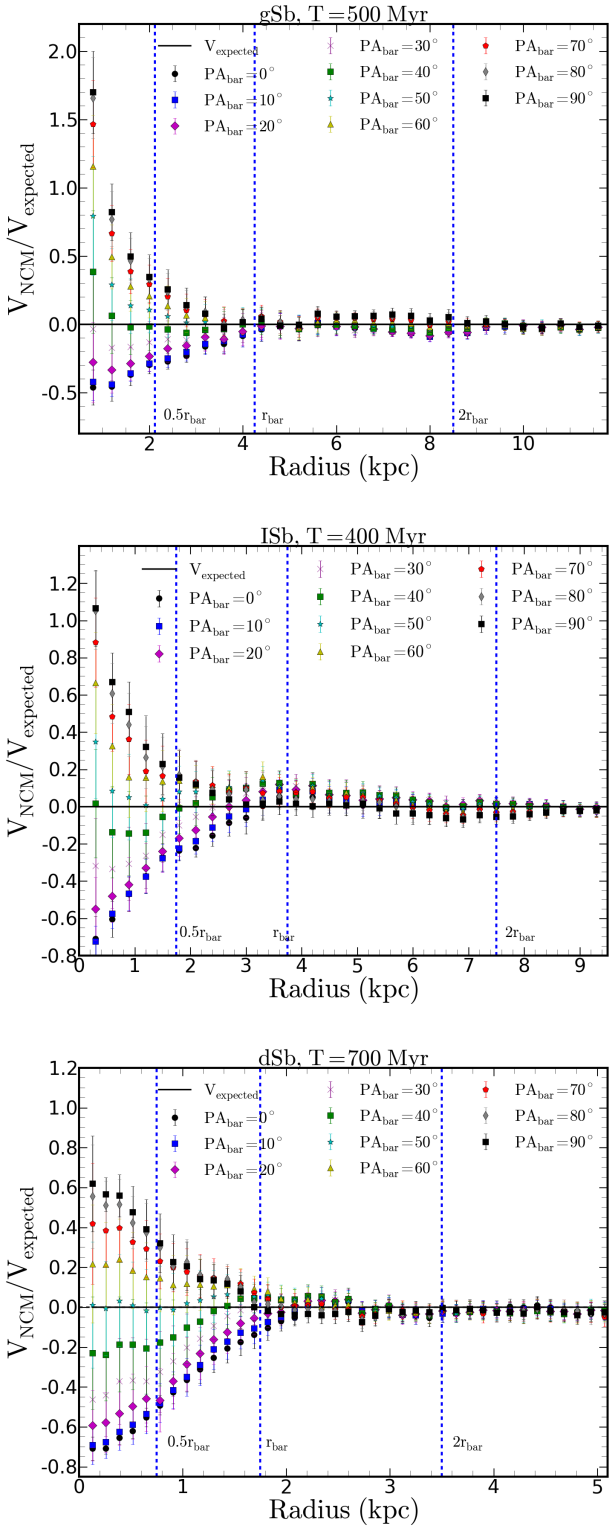

FIGURE 4.6: Ratio between V_{NCM} = V_{ROTCUR} - $V_{expected}$ and $V_{expected}$ as a function of radius for the gSb, iSb and dSb models. The vertical dashed lines show 0.5, 1 and 2r_{bar} estimated from the Fourier decomposition. Each rotation curve was derived from mock galaxies with projected bar orientation between 0 and 90 degrees. The projected bar PA are shown on top of each figure.

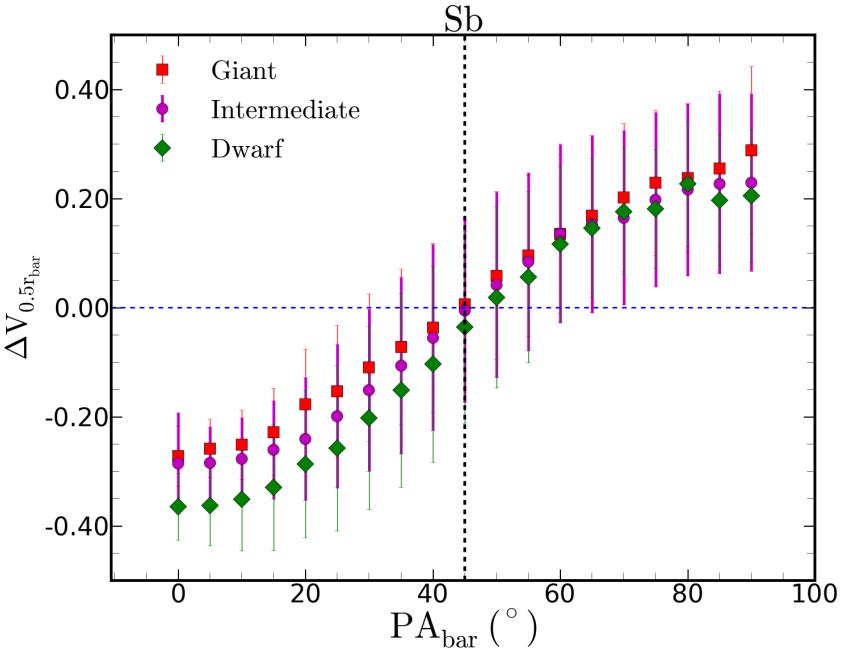

FIGURE 4.7: Rotation curve error Δ V = [V_{rotcur} - $V_{expected}$]/$V_{expected}$ at R=0.5r_{bar} where r_{bar} is the bar radius estimated from the Fourier decomposition for all the Sb models. The giant Sb model is presented as red squares, the intermediate Sb as magenta circles and the dwarf or low mass Sb as green diamonds.

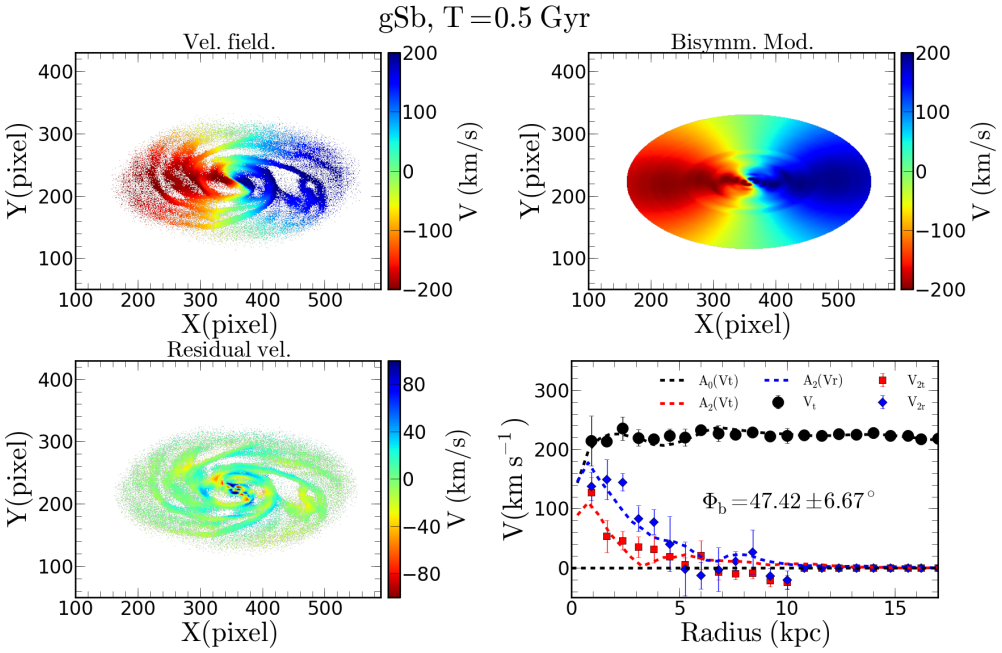

FIGURE 4.8: DiskFit results for a giant Sb model, Left panel: the observed velocities field (top) and the residual velocities (bottom). Right panel: the DiskFit model (top) and a comparison between V_t, V_{2t} and V_{2r} with the amplitude of the m=0 and m=2 Fourier mode A_0 and A_2 (bottom).

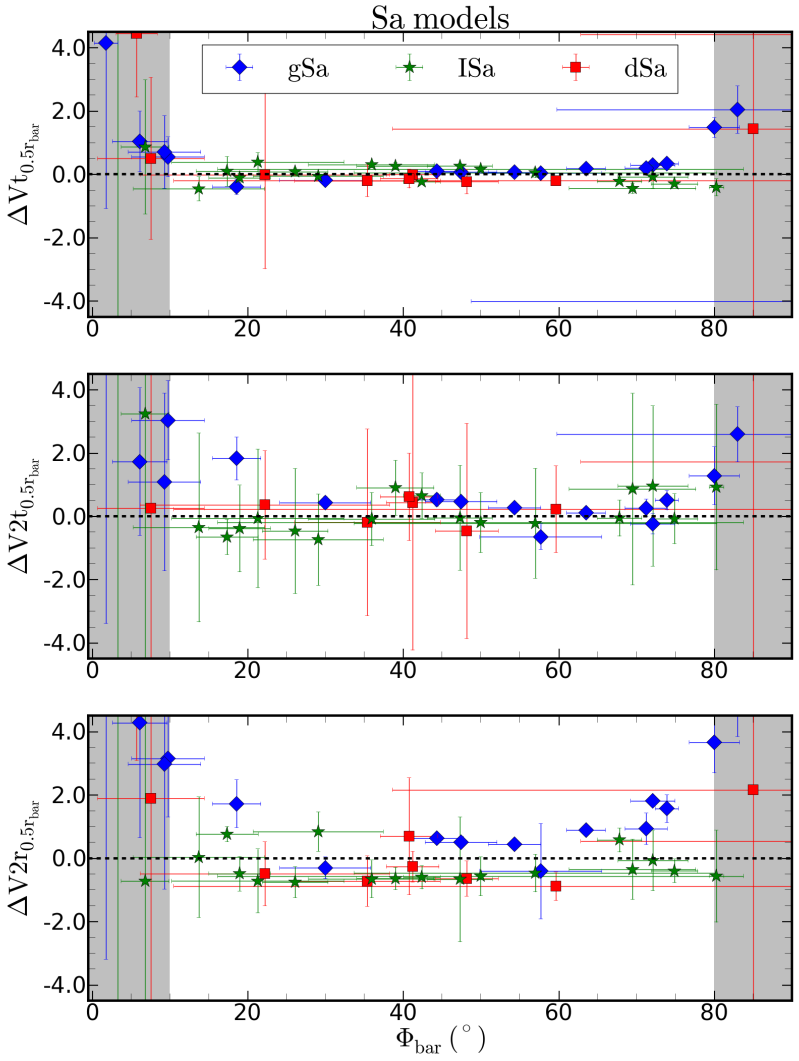

FIGURE 4.9: Ratio between the Fourier amplitudes and the DiskFit velocities at R=0.5r_{bar} (estimated from the Fourier decomposition of the stellar surface densities) for the spiral Sa models, giants (blue), intermediate (green) and dwarf (red). The ratio $\Delta V_t = (V_t - A_{0,t})/A_{0,t}$ is plotted in the top panel, $\Delta V_{2r} = (V_{2r} - A_{2,r})/A_{2,r}$ in the middle panel and $\Delta V_{2t} = (V_{2t} - A_{2,t})/A_{2,t}$ in the bottom panel. The shaded area shows the range of bar orientations where DiskFit fails to recover the bar orientation or velocities, or where the uncertainties on the returned parameters are large.

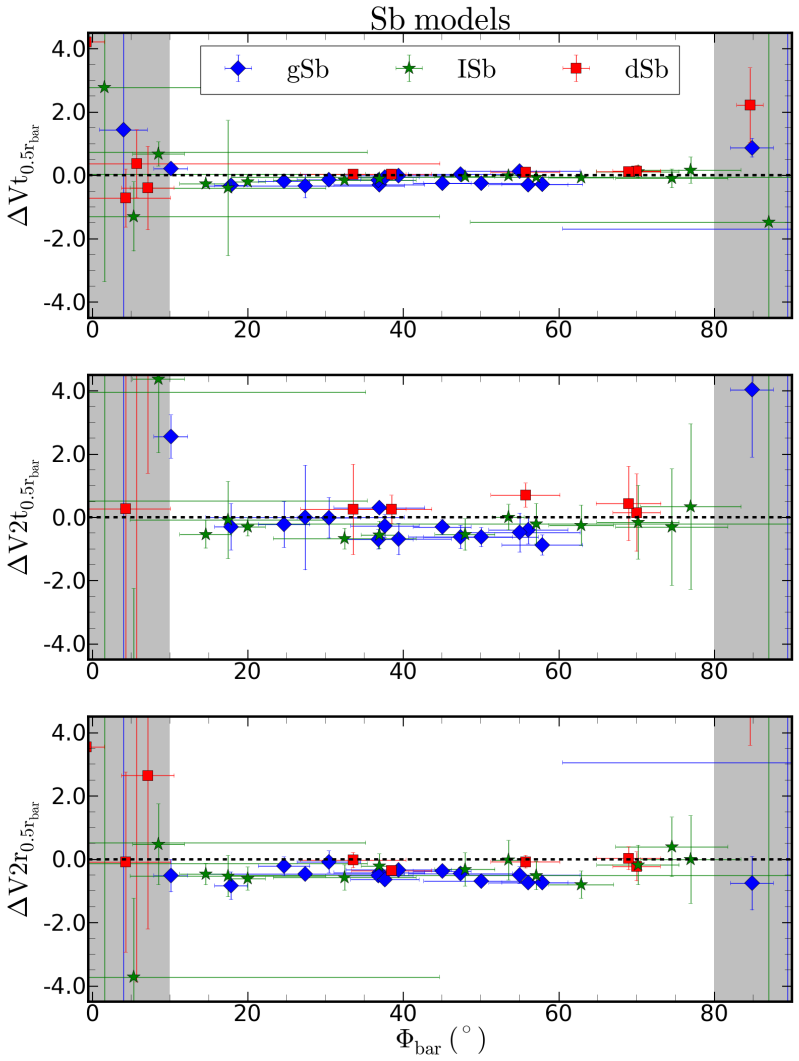

FIGURE 4.10: Same as Fig 5.9 but for the Sb models.

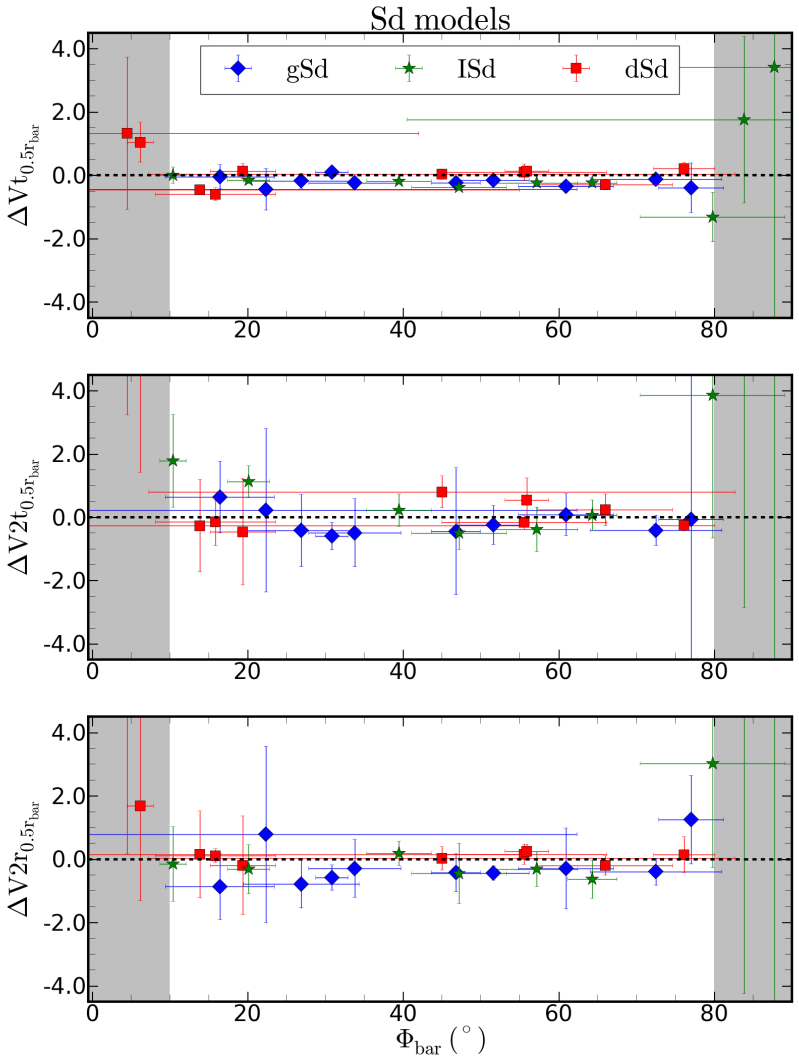

FIGURE 4.11: Same as Fig 5.9 but for the Sd models.

4.6 Summary

We present an analysis of the strongest barred snapshots of nine isolated GalMer simulations. We characterized the intrinsic bar strengths and non-circular motions and compared them to mock observations of the systems.

We found that:

1. The bar lengths estimated from ellipse fitting are shorter than those estimated from the Fourier decomposition technique which is consistent with previous studies (e.g., Erwin 2005; Aguerri et al. 2009).

2. The Fourier decomposition technique gives similar results for the bar properties when applied directly to the simulation or to the images obtained from mock observations.

3. ROTCUR systematically under-estimates the velocities when the bar is parallel to the major axis and overestimates them when the bar is perpendicular to the major axis for all the models. This shows the importance of properly accounting for the non-circular motions induced by the bar when deriving rotation curves (see Spekkens & Sellwood 2007; Dicaire et al. 2008; Randriamampandry et al. 2015).

4. The magnitude of the rotation curves error when ROTCUR is used depends only on the orientation of the bar and it is not correlated with either the bar strength or the bar length.

5. DiskFit is able to reproduce the amplitudes of the Fourier m=0 and m=2 components when the bar is at an intermediate PA.

6. Unlike ROTCUR, DiskFit does not show a systematic over-estimation or under-estimation of the inner part of the rotation curves.

7. DiskFit fails to recover the bar orientation or velocities, or return large parameter uncertainties when the bar is closer than 10 degrees to either the minor or the major axis (see also Sellwood & Sánchez 2010).

As future work, we will be using new simulations of a sample of four barred galaxies. This will allow us to perform a direct comparison between the simulation with the HI and ancillary data from observations, as well as putting a tighter constraint on the bar orientation range where DiskFit fails.

Acknowledgments

We thank the anonymous referee for the comments and suggestions. CC's work is based upon research supported by the South African Research Chairs Initiative (SARChI) of the Department of Science and Technology (DST), the SKA SA and the National Research Foundation (NRF). ND and TR's work is supported by a SARChI's South African SKA Fellowship. KS acknowledges support from the National Sciences and Engineering Research Council of Canada (NSERC).

Bibliography

Aguerri, J. A. L., Beckman, J. E., & Prieto, M. 1998, AJ, 116, 2136

Aguerri, J. A. L., Debattista, V. P., & Corsini, E. M. 2003, MNRAS, 338, 465

Aguerri, J. A. L., Méndez-Abreu, J., & Corsini, E. M. 2009, A&A, 495, 491

Athanassoula, E., & Misiriotis, A. 2002, MNRAS, 330, 35

Athanassoula, E., Machado, R. E. G., & Rodionov, S. A. 2013, MNRAS, 429, 1949

Barazza, F. D., Jogee, S., & Marinova, I. 2008, Formation and Evolution of Galaxy Disks, 396, 351

Begeman K. G., 1989, A&A, 223, 47

Bosma, A. 1978, Ph.D. Thesis,

Díaz-García, S., Salo, H., Laurikainen, E., & Herrera-Endoqui, M. 2016, A&A, 587, A160

Chapelon, S., Contini, T., & Davoust, E. 1999, A&A, 345, 81

Chilingarian, I. V., Di Matteo, P., Combes, F., Melchior, A.-L., & Semelin, B. 2010, A&A, 518, A61

Christodoulou, D. M., Tohline, J. E., & Steiman-Cameron, T. Y. 1993, ApJ, 416, 74

Debattista, V. P., & Sellwood, J. A. 2000, ApJ, 543, 704

de Blok W. J. G., Walter F., Brinks E., Trachternach C., Oh S.-H., Kennicutt, Jr. R. C., 2008, AJ, 136, 2648

de Vaucouleurs G., de Vaucouleurs A., Corwin, Jr. H. G., Buta R. J., Paturel G., Fouqué P., 1991, Third Reference Catalogue of Bright Galaxies. Volume I: Explanations and references. Volume II: Data for galaxies between 0^h and 12^h. Volume III: Data for galaxies between 12^h and 24^h.

Dicaire, I., Carignan, C., Amram, P., et al. 2008, MNRAS, 385, 553

Erwin, P. 2005, MNRAS, 364, 283

Eskridge, P. B., Frogel, J. A., Pogge, R. W., et al. 2000, AJ, 119, 536

Franx, M., van Gorkom, J. H., & de Zeeuw, T. 1994, ApJ, 436, 642

Gerhard, O. E., & Fall, S. M. 1983, MNRAS, 203, 1253

Heller, C. H., & Shlosman, I. 1994, ApJ, 424, 84

Józsa, G. I. G. 2007, A&A, 468, 903

Knapen, J. H., Shlosman, I., & Peletier, R. F. 2000, ApJ, 529, 93

Laurikainen, E., Salo, H., & Buta, R. 2005, MNRAS, 362, 1319

Laurikainen, E., Salo, H., Buta, R., & Vasylyev, S. 2004, MNRAS, 355, 1251

Lynden-Bell, D., & Kalnajs, A. J. 1972, MNRAS, 157, 1

Martin, P. 1995, AJ, 109, 2428

Marinova, I., & Jogee, S. 2007, ApJ, 659, 1176

Marinova, I., Jogee, S., Barazza, F. D., et al. 2009, Galaxy Evolution: Emerging Insights and Future Challenges, 419, 138

Masters, K. L., Nichol, R. C., Hoyle, B., et al. 2011, MNRAS, 411, 2026

Menéndez-Delmestre, K., Sheth, K., Schinnerer, E., Jarrett, T. H., & Scoville, N. Z. 2007, ApJ, 657, 790

Méndez-Abreu, J., Sánchez-Janssen, R., & Aguerri, J. A. L. 2010, ApJL, 711, L61

Michel-Dansac, L., & Wozniak, H. 2006, A&A, 452, 97

Oh, S. H., Kim, W.-T., & Lee, H. M. 2015, ApJ, 807, 73

Randriamampandry, T. H., & Carignan, C. 2014, MNRAS, 439, 2132

Randriamampandry, T. H., Combes, F., Carignan, C., & Deg, N. 2015, MNRAS, 454, 3743

Regan, M. W., Sheth, K., & Vogel, S. N. 1999, ApJ, 526, 97

Salo, H., Laurikainen, E., Buta, R., & Knapen, J. H. 2010, ApJL, 715, L56

Sellwood, J. A., & Sánchez, R. Z. 2010, MNRAS, 404, 1733

Shlosman, I., & Noguchi, M. 1993, ApJ, 414, 474

Spekkens, K., & Sellwood, J. A. 2007, ApJ, 664, 204

Valenzuela, O., Rhee, G., Klypin, A., et al. 2007, ApJ, 657, 773

Weinberg, M. D. 1985, MNRAS, 213, 451

Chapter 5

Paper III: Simulating non-axisymmetric flows in disc galaxies

Submitted to the Monthly Notices of the Royal Astronomical Society; T. H. Randriamampandry, N. Deg and L. Widrow, MNRAS, (2017)

Abstract

We present a method to simulate and study non-circular motions in strongly barred galaxies. We test our method on the unbarred galaxy NGC 3621 and the barred galaxies NGC 1300 and NGC 1530. NGC 3621 provides a validation of our method of generating initial conditions. NGC 1530 has an intermediate bar orientation that allows for a comparison to DiskFit. Finally NGC 1300 has a bar oriented parallel to the galaxy's major axis, where other algorithms tend to fail. The initial parameters are constrained using a Bayesian analysis of each galaxy azimuthally averaged rotation curve, the 3.6 μm surface brightness, and the gas surface density. Equilibrium models are then generated using the GalactICS code and evolved using GADGET-2. The bar strengths and mock velocity maps of the resulting snapshots are compared to observations in order to determine the best representation of the galaxy. We are able to reproduce the bar strength from the literature at peak bar strength. Our models for NGC 3621 and NGC 1530 are comparable to those obtained using commonly available algorithms. However, the mass distribution of NGC 1300, with a bar parallel with the major axis, can only be inferred from the model.

Keywords: N-body simulations, galaxies: dynamics and kinematics – structure, cosmology: dark matter

5.1 Introduction

Galaxy rotation curves (RCs) that are derived from spectroscopic observations of the gas content can be used to infer the distribution of dark matter in disk galaxies (e.g. de Blok et al. 2008). This inference relies on the assumption that the gas moves along circular orbits. However, in barred galaxies, the gas has significant non-circular flows that lead to systematic errors in the measured RCs (Oh et al. 2008). Two of the most well-known methods used when deriving RCs are ROTCUR (Begeman 1989) and DiskFit (Spekkens & Sellwood 2007). ROTCUR is an implementation of the tilted-ring method (Rogstad et al. 1974) and assumes axial symmetry. It is known to under/over-estimate the RC when the bar is parallel/perpendicular to the major axis of the observed galaxy (e.g. Randriamampandry et al. 2015; Dicaire et al. 2008). DiskFit is specifically designed to account for the non-circular motions mainly induced by bars (Spekkens & Sellwood 2007). It works quite well for bars with an intermediate orientation. However, when the bar orientation approaches the major or minor axis, a degeneracy in the fitting equation causes the algorithm to fail (Sellwood & Sánchez 2010). Quantitatively, that failure occurs when the bar is within $\pm$ 10° of the major or minor axis of the galaxy (Randriamampandry et al. 2016).

In this work, we use tailored hydrodynamical simulations to model galaxies. The initial condition are generated using a version of the GalactICs (Galaxy Initial Conditions) code (Widrow et al. 2008) that has been modified to include gas disks (Deg et al. 2017). The parameters for the bulge, stellar and gas disks and dark halo are determined for a particular galaxy from a Bayesian analysis of each galaxy's azimuthally averaged RC, 3.6 micron surface brightness profile,

and gas surface density. Though the initial conditions are axisymmetric, non-axisymmetric features such as bars and spiral arms may formed with time through disk instability. Each simulation is evolved for 5 Gyr using the GADGET-2 code (Springel 2005). We compare the pseudo-observations of velocity fields and bar properties of the simulations to those measured from the actual galaxies.

We consider three disk galaxies; NGC 3621, NGC 1530 and NGC 1300. NGC 3621 is an unbarred SAd galaxy (Walter et al. 2008), NGC 1530 is a strongly barred SBb galaxy with an intermediate bar orientation that allows our results to be compared with those from a DiskFit analysis and NGC 1300 is a strongly barred SBbc galaxy where the bar is parallel to the position angle. Our goal is to infer the mass distribution of NGC 1300 and correct its RC using numerical simulations.

In Section 5.2 we present the observations of NGC 3621, 1530, and 1300. Section 5.3 describes our algorithm in detail. In Section 5.4 we compare our simulations to the velocity fields of each galaxy. Finally, Section 5.5 contains our discussion and conclusions.

5.2 Data from observations

In this section, we present the galaxies in our sample and the data that are used to constrain the initial conditions. These observations comprise: the RC, the gas density profile and 3.6μm surface brightness profile.

The sample galaxies were selected depending on their bar properties and the availability of HI and near-infrared observations. Table 5.1 summarizes their properties. The sample includes two strongly barred galaxy NGC 1300 and NGC 1530 and the late-type unbarred spiral galaxy NGC 3621.

- NGC 3621 is included in the sample to test the basic methodology. NGC 3621 is a late type unbarred spiral galaxy located at a distance of 6.6 Mpc

(Freedman et al. 2001). This galaxy is part of The HI Nearby Galaxies Survey (THINGS, Walter et al. 2008). THINGS data products are publicly available and can be obtained from their webpage (`http://www.mpia.de/THINGS/Data.html`). The velocity map is derived from the natural weighted datacube using the GIPSY task MOMENTS. The velocity map is used to derive the RC using the GIPSY task ROTCUR. The gas density profile is obtained from the moment0 map using the ELLINT task and assuming the kinematic parameters from de Blok et al. (2008). The 3.6 μm surface brightness profiles are obtained from de Blok (private communication).

- NGC 1530 is a barred spiral galaxy, SBb, located at a distance of 18.5 Mpc. The HI observations were obtained using the DnC array configuration of the VLA (Condon et al. 1996) and reduced using standard AIPS packages. This galaxy has a strong bar with intermediate orientation, Φ_b = -25 degree (Menéndez-Delmestre et al. 2007). The 3.6 μm surface brightness profile was obtained from SPITZER images retrieved from the archive and derived using the IRAF task ELLIPSE. The image was first cleaned from foreground stars before being used in the ELLIPSE task. The profile was then corrected for inclination.

- NGC 1300 is a grand design barred spiral galaxy, SBbc, located at a distance of 17.1 Mpc. The bar is almost parallel with the major axis with a bar position angle of -2 degrees (Aguerri et al. 2000). The HI observations are obtained using the VLA C configuration. The data were firstly analyzed by England (1989) and later by Lindblad et al. (1997) whose reported different values for the inclination and position angle of the disc. We re-analyzed and re-reduced the data and found the same kinematic parameters as those reported by Lindblad et al. (1997). These kinematic parameters were then used to derive the RC and the gas density profile. The 3.6 μm surface brightness profile was derived using the same method as NGC1530.

Name	V_{sys} (km/s)	Morph. type	D (Mpc)	P. A. (◦)	Incl. (◦)	Bar strength (Q_b)	ϕ_{bar}(◦)	R_{bar}(arcsec)
1	2	3	4	5	6	7	8	9
NGC3621	729	SAd	6.6[F01]	345[dB08]	65[dB08]	-	-	-
NGC1350	2461	SBb	18.5	188	50	0.39[A98]	-25 [MD07]	37[A98]
NGC1300	1575	SBbc	17.1	267[Lin97]	35[Lin97]	0.537[L04]	-2 [L04]	87[L04]

Notes
A98: Aguerri et al. (1998), dB08: de Blok et al. (2008), L04: Laurikainen et al. (2004),
Lin97: Lindblad et al. (1997), MD07: Menéndez-Delmestre et al. (2007),FO1:Freedman et al. (2001).

TABLE 5.1: Summary of the properties of the galaxies in the sample.

5.3 Simulating disc galaxies

In this section, we outline the steps adopted to construct the models. The GalactICs code that is used to generate the initial conditions is briefly described in Section 5.3.1, the method used to estimate the model input parameters are outlined in Section 5.3.2 and details about the simulations are given in Section 5.3.3.

5.3.1 GalactICs models

We use a new version of the GalactICs code (Widrow et al. 2008; Deg et al. 2017) that includes a gas disk component to build our model galaxies. GalactICs constructs multi-component axisymmetric galaxy models (see Chequers et al. 2016 and references therein) based on distribution functions. In this work, we generate galaxies with a Sérsic bulge, an exponential stellar disk, an exponential gas disk, and a double-power law dark matter halo.

The density profile of the Sérsic bulge is (Puglielli et al. 2010)

$$\rho_{\rm bulge}(r) = \rho_b \left(\frac{r}{r_b}\right) e^{\left[-b\left(\frac{r}{r_b}\right)^{1/n}\right]}, \tag{5.1}$$

where r is the spherical radius and $p = 1 - 0.6097/n + 0.05563/n^2$ yields the Sérsic profile (Prugniel & Simien 1997). For simplicity, the bulge is characterized by a

scale velocity, σ_b, given by

$$\sigma_{\rm b} = [4\pi {\rm n} {\rm b}^{{\rm n}({\rm p}-2)}({\rm n}(2-{\rm p}))r_{\rm b}^2\rho_{\rm b}]^{1/2}. \tag{5.2}$$

GalactICs assumes an exponential-sech^2 (van der Kruit & Searle 1981) density distribution for the disk.

$$\rho_{\rm d}({\rm R},{\rm z}) = \frac{{\rm M_d}}{4\pi {\rm R_d^2 z_d}} {\rm e}^{(-{\rm R}/{\rm R_d})} {\rm sech}^2({\rm z}/{\rm z_d}), \tag{5.3}$$

where M_d is the disk mass, R_d is the disc scale length, and z_d is the disc scale height and R is the cylindrical radius. The radial velocity dispersion is given by

$$\sigma_{\rm R}^2({\rm R}) = \sigma_0^2 {\rm e}^{-({\rm R}/{\rm R}_\sigma)}, \tag{5.4}$$

where σ_0 and R_σ are the central dispersion and a scale radius respectively. For simplicity, R_σ is set equal to the scale length and σ_0 is fixed to 10 km/s. The disk is also truncated at R_t= 50 kpc for all models.

The gas disk has an exponential surface density. Following Wang et al. (2010), the disk is initially isothermal, which requires a scale height that increases with radius. A detailed discussion of the gas disk is found in Deg et al. (2017).

The double power-law halo is defined as (see Widrow et al. 2008)

$$\rho({\rm R}) = \frac{2^{2-\alpha}\sigma_{\rm h}^2}{4\pi r_{\rm h}^2} \frac{1}{{\rm u}^\alpha(1+{\rm u})^{\beta-\alpha}} {\rm C}({\rm r};{\rm r_t},\delta {\rm r_t}) \ , \tag{5.5}$$

where $u = r/r_h$, σ_h is a scale velocity, and r_h is the scale radius. The $C(r; r_t, \delta r_t)$ term is a truncation factor, given by

$${\rm C}({\rm r};{\rm r_t},\delta {\rm r_t}) = \frac{1}{2}{\rm erfc}\left(\frac{{\rm r}-{\rm r_t}}{\sqrt{2}\delta {\rm r_h}}\right). \tag{5.6}$$

In this work the truncation parameters are set to r_t = 200 kpc and δr_t=20 kpc

Parameter	Units	NGC3621		NGC1530		NGC1300	
		Min.	Max.	Min.	Max.	Min.	Max.
1	2	3	4	5	6	7	8
Halo scale velocity: σ_h	km s^{-1}	10	2000	10	1000	10	1000
Halo scale radius: R_h	kpc	5.0	20.0	2.0	20.0	1.0	20.0
Inner slope:α	-	0.01	5.0	0.1	5.0	0.1	5.0
Outer slope:β	-	0.01	10.0	0.1	10.0	0.1	10.0
Stellar disk mass:M_d	10^{10} $M_\odot$	0.08	11.8	0.05	10.5	0.05	16.5
Disk scale length: R_d	kpc	1.0	20.0	1.0	6.5	0.5	6.5
Gas mass:M_g	10^{10} $M_\odot$	0.02	3.5	0.01	3.5	0.02	3.5
Gas scale length: R_g	kpc	1.0	20.0	0.5	20.0	1.0	20.0
Bulge Sérsic index: n	-	0.01	5.0	0.01	5.0	0.01	5.0
Characteristic bulge velocity:σ_b	km s^{-1}	10	500	10	250	10	600
Bulge scale length:R_b	kpc	0.1	2.5	0.05	1.5	0.05	2.5

Notes
The parameters' name are in column 1, the units are given in column 2.
The lower and upper bounds are shown in columns 3, 5, 7 and 4, 6, 8 respectively.

TABLE 5.2: Summary of the model parameters.

Parameter	Units	Best fit	Model-A	Model-B	Model-C	THINGS-ISO	THINGS-NFW
1	2	3	4	5	6	7	8
σ_h	km s^{-1}	275 ± 32	280	265	275	-	-
R_h	kpc	15.26 ± 2.08	14.50	16.01	15.26	-	-
α	-	0.52 ± 0.22	0.50	0.12	0.52	0	1
β	-	2.80 ± 0.32	3.12	2.75	2.80	2	3
M_d	10^{10} $M_\odot$	1.90 ± 0.31	2.20	3.28	1.90	1.95	1.95
R_d	kpc	2.45 ± 0.25	2.60	2.62	2.45	2.61	2.61
M_g	10^{10} $M_\odot$	0.89 ± 0.05	0.94	1.11	0.89	0.70	0.70
R_g	kpc	14.89 ± 0.03	15.00	12.32	14.98	-	-
σ_b	km s^{-1}	62 ± 17	50	40	62	-	-
R_b	kpc	0.96 ± 0.22	0.60	1.01	0.96	-	-
ρ_0	10^{-3} M$_\odot$pc^{-3}	-	-	-	-	14.4	-
R_c	kpc	-	-	-	-	5.59	-
V_{200}	km s^{-1}	-	-	-	-	-	165
R_s	kpc	-	-	-	-	-	28.8
Q_d	-	-	4.89	4.48	3.10	-	-
X_d	-	-	1.75	1.57	1.26	-	-

Notes
The ISO and NFW THINGS best fit mass model results from Walter et al. (2008) are shown in column 7 and 8 for comparison
dB08: de Blok et al. (2008), W08: Walter et al. (2008).
Q_d and X_d are the disk stability parameters
R_c and R_s are the ISO and NFW scale radius respectively

TABLE 5.3: Comparison between the model input parameters and the THINGS mass model results for NGC 3621.

Parameter	Units	best fit	Model-A	Model-B	Model-C
1	2	3	4	5	6
σ_h	km s^{-1}	310 ± 19	325	310	310
R_h	kpc	16.79 ± 1.25	16.14	16.79	14.76
α	-	0.34 ± 0.09	0.33	0.34	0.24
β	-	2.42 ± 0.16	2.59	2.42	2.55
M_d	10^{10} $M_\odot$	3.53 ± 0.29	3.00	3.53	3.16
R_d	kpc	3.36 ± 0.29	3.88	3.56	3.48
M_g	10^{10} $M_\odot$	1.39 ± 0.02	1.33	1.34	1.33
R_g	kpc	6.19 ± 0.07	6.06	6.19	6.14
σ_b	km s^{-1}	446 ± 20	455	4.46	4.99
R_b	kpc	0.65 ± 0.06	0.72	0.64	0.59
Q_d	-	-	6.38	5.11	3.54
X_d	-	-	3.38	3.11	2.40

TABLE 5.4: NGC1530 Model input parameters.

Parameter	Units	best fit	Model-A	Model-B	Models-C
1	2	3	4	5	6
σ_h	km s^{-1}	159 ± 58	242	159	255
R_h	kpc	10.88 ± 3.31	13.45	10.88	13.65
α	-	0.76± 0.25	0.68	0.76	0.31
β	-	2.98 ± 0.56	3.54	2.98	3.42
M_d	10^{10} $M_\odot$	8.72 ± 1.34	7.37	8.72	8.82
R_d	kpc	5.59 ± 0.18	5.79	5.59	5.81
M_g	10^{10} $M_\odot$	0.52 ± 0.07	0.55	0.52	0.54
R_g	kpc	9.85 ± 0.85	9.71	9.85	10.68
σ_b	km s^{-1}	53 ± 18	70.0	53	43
R_b	kpc	2.59 ± 0.99	1.17	2.59	2.21
Q_d	-	-	3.45	2.61	2.20
X_d	-	-	1.45	1.15	1.02

Table 5.5: NGC1300 Model input parameters.

5.3.2 GalactICs input parameter estimations

In order to find plausible initial model parameters for the simulations, we first run a Bayesian analysis for each galaxy. For this analysis we utilize analytic approximations of axisymmetric GalactICs models. In this approximation, the gas disk is given a constant scale height, rather than the flaring profile built into GalactICs. The models are constrained by the RC, the azimuthally averaged 3.6 micron stellar surface brightness, and the gas surface density. In order to avoid any systematic errors caused by the presence of the bars, we fit only the portion of the RC beyond $\approx 2\ r_{bar}$ in cases of NGC 1530 and NGC 1300. We also avoid the outermost regions of the 3.6 μm surface brightness due to possible contaminations.

The likelihood for a particular model is

$$\mathcal{L}(\mathrm{D}|\Theta) = \Pi_{\mathrm{i}=1}^{\mathrm{N}} \frac{1}{\sqrt{2\pi\sigma_{D,i}^2}} \mathrm{e}^{\frac{-(\mathrm{D_i}-\mathrm{M}(\Theta)_\mathrm{i})^2}{2\sigma_{\mathrm{D,i}}^2}}, \tag{5.7}$$

where Θ are the model parameters, D are the observations, σ_D are the uncertainties in the observations, $M(\Theta)$ are the mock observations from the model and N is the number of observed data points. The posterior probability for a model is

$$\mathrm{p}(\Theta|\mathrm{D},\mathrm{I}) = \frac{\mathrm{p}(\Theta|\mathrm{I})\mathcal{L}(\mathrm{D}|\Theta)}{\mathrm{Z}}, \tag{5.8}$$

where $p(\Theta|I)$ is the prior probability for a model and Z is the evidence. Since we are performing a parameter estimate, the evidence is simply a normalization factor that is canceled out in the analysis.

To explore the parameter space we use the EMCEE algorithm (Foreman-Mackey et al. 2013). EMCEE is a parallel, affine-invarient Markov Chain Monte Carlo (MCMC) algorithm. It operates by initializing an ensemble of walkers randomly throughout the parameter space. The walkers move throughout the space by first proposing a new position using stretches along the vector to another randomly

selected walker. The posterior of the proposal is evaluated and compared to the current posterior in order to determine whether the walker will move or not. In this work, we use 200 walkers for 3500 steps, giving a total of 7×10^5 likelihood calls. For simplicity, the priors for each parameter are uniform. A list of the relevant parameters as well as their minimum and maximum values considered are given in Table 5.2.

The input parameters for the initial condition are selected based on the parameter PDFs and the disk stability parameters PDFs. We simulate three models for each galaxy. The first model uses the the peak parameter values in the parameter PDFs. The other two are models accepted by the Bayesian process with either low or high disk stability. We then select the model that best reproduce the observations.

The disk stability can be quantified using the Toomre Q (Toomre 1964) and X (Goldreich & Tremaine 1978, 1979) parameters. The Toomre Q parameter is given by

$$\mathrm{Q_d} = \frac{\sigma_\mathrm{r}\kappa}{3.36\mathrm{G}\Sigma_\mathrm{d}} \ , \tag{5.9}$$

for a stellar disk where σ_r is the radial velocity dispersion, κ is the epicyclic frequency, G is the gravitational constant and Σ_d is the stellar surface density. For the gas disk Q_g is

$$\mathrm{Q_g} = \frac{\mathrm{c_s}\kappa}{\pi\mathrm{G}\Sigma_\mathrm{g}} \ , \tag{5.10}$$

where c_s is the sound speed of the gas and Σ_g the gas surface density (Wang et al. 2010). The Q parameters are measures of a disk's stability against local perturbations. By contrast, the X parameter is a measure of a disk's self-gravity and it indicates the disk's stability against global perturbations. It is given by

$$X = \frac{V_t^2(2.2R_d)}{V_d^2(2.2R_d)} \ , \tag{5.11}$$

where V_t and V_d are the total circular velocity and the circular velocity due to the disk respectively. It is measured at $2.2R_d$ (as well as the Q parameters in this

work) as that is where the exponential disk's contribution peaks. Unstable disks have large values X and low Q, while those with low X and high Q are significantly more stable.

The formal errors obtained during the derivation of the gas surface density and the 3.6 μ surface brightness profiles do not reflect the true uncertainties in the measurement. In order to more accurately represent the uncertainties in these profiles we include two extra parameters; ϵ_{SD} for the gas surface density and ϵ_S for the stellar surface brightness profiles. These are added in quadrature to the formal errors during the Bayesian analysis. For those profiles we set:

$$\sigma_{\rm G}^2 = \epsilon_{\rm G}^2 + \epsilon_{\rm p,G}^2 \ , \tag{5.12}$$

for the gas density and

$$\sigma_{\rm S}^2 = \epsilon_{\rm S}^2 + \epsilon_{\rm p,S}^2 \ , \tag{5.13}$$

for the stellar surface brightness profile, where ϵ_G, ϵ_S are the measured uncertainty and $\epsilon_{p,G}$, $\epsilon_{p,G}$ are the error parameters.

5.3.3 The simulations

Armed with the GalactICs parameters for each galaxy, we generated our N-body realizations with 10^6 particles; 5×10^5 for the halo, 2×10^5 for the stellar disk, another 2×10^5 for the gas disk and 10^5 for the bulge. The models were evolved for 5 Gyr using the GADGET-2 code with a softening length of 50 pc. Snapshots were taken every 50 Myr in order to follow the evolution of the galaxy in detail. A mock velocity field was calculated for each snapshot and compared to the velocity fields obtained for the actual galaxies.

In detail, the velocity fields for each galaxy are obtained using HI observations of each galaxy combined with position angle, inclination, and systemic velocities

listed in Table 5.1. The mock velocity fields are obtained by rotating and shifting the simulation to the same distance, orientation, and systemic velocity as the actual galaxy. The N-body system was then "observed" with the same pixel resolution and beam as used in the HI observations, without any noise. This allows for a pixel-by-pixel comparison of the model and observed velocity maps. The snapshot that best represents each galaxy is selected based on both the bar strength and this velocity map comparison.

The bar strength of a galaxy can be defined by either the Fourier m=2 mode, or the maximum ellipticity of the iso-density contours (see Aguerri et al. 2009; Randriamampandry et al. 2016). The ellipse fitting method is usually used on optical and infrared images, while Fourier decomposition is typically used for N-body simulations. Therefore, we adopt A_2 as the estimate of the bar strength. The surface density of either the stellar or gas disks can be expressed as a Fourier series through

$$\Sigma(r, \phi) = \frac{a_0(r)}{2} + \sum_{n=1}^{\infty} (a_m(r)\cos(m\phi) + b_m(r)\sin(m\phi)) \ , \tag{5.14}$$

where $a_m(r)$ and $b_m(r)$ are the radial Fourier coefficients. The bar strength is the amplitude of the $m = 2$ moment, which is given by

$$A_2 = \sqrt{a_2^2 + b_2^2} \ . \tag{5.15}$$

We require that both the bar strength and the velocity map of the snapshot match the observations. For the velocity comparison, we first construct a residual map, defined as

$$V^i_{res} = V^i_{obs} - V^i_{mod} \ , \tag{5.16}$$

where V^i_{obs} and V^i_{mod} are the observed and modeled velocity at a given pixel i in the velocity map. The best-fitting snapshot is the one with the smallest standard deviation σ_{res} in the residuals. This quantity is given by

$$\sigma_{\rm res} = \sum_{\rm i=0}^{\rm N} \left(\frac{(\overline{\rm V^i_{res}} - \rm V^i_{res})^2}{\rm N} \right) , \tag{5.17}$$

where N is the number of pixel and $\overline{V^i_{res}}$ the mean of the residual velocities.

In addition to these quantities, we also calculate the 'expected' RC for each snapshot and a Fourier decomposition of the radial and tangential gas particle velocities. These quantities are used to compare our results to those obtained using ROTCUR and DiskFit.

The expected RC is defined as

$$\langle \rm V^2_{expected} \rangle = \rm r \left\langle \frac{\partial \Phi}{\partial r} \right\rangle = \langle \rm F_r \rangle , \tag{5.18}$$

where F_r is the radial force from the particles calculated azimuthally on an angular grid and Φ is the gravitational potential.

The Fourier velocity components are given by

$$\rm V_t(r,\theta) = A_{0,t}(r) + \sum_{m=1}^{\infty} A_{m,t}(r) cos[m\theta + \theta_{m,t}(r)] , \tag{5.19}$$

and

$$\rm V_r(r,\theta) = A_{0,r}(r) + \sum_{m=1}^{\infty} A_{m,r}(r) cos[m\theta + \theta_{m,r}(r)] , \tag{5.20}$$

where $A_{m,t}(r)$ and $A_{m,r}(r)$ are the tangential and radial Fourier m^{th} velocity moments respectively and θ, $\theta_{m,t}(r)$ and $\theta_{m,r}(r)$ are the angular phases.

5.4 Results and discussions

In this section, we compare the bar properties derived from the simulations and the model velocity maps with the observations. The results for NGC 3621, NGC 1530 and NGC 1300 are presented and discussed in Section 5.4.1, Section 5.4.2 and Section 5.4.3 respectively.

5.4.1 NGC 3621 model

The Bayesian analysis of the RC, 3.6μ surface brightness, and gas surface density of NGC 3621 gives the posterior distribution function (PDF) for the full model parameter space. The best fit GalactICs parameters are given in Table 5.3, the uncertainties are the 1-sigma error obtained from the PDFs. Using the parameter PDFs we obtained the PDFs of the RC, surface density, and surface brightness profiles shown in Fig. 5.1, as well as PDFs of the stability parameters.

In Table 5.3 we also give the mass models found by the THINGS analysis for comparison. Our Bayesian analysis of the disk agrees with the THINGS disk model. However, both pure cored (ISO-type) and cuspy (NFW-type) models are excluded in our analysis. Our analysis prefers an inner slope of 0.5, which is midway between the THINGS models. In addition, our inferred gas mass is slightly larger than the THINGS gas mass, but this difference is largely due to the different methodologies adopted. The THINGS analysis sums up the mass of all visible gas, while we fit an exponential surface density where M_g is the total integrated mass of that exponential. However, Figure 5.1 shows that our models provide good fits to the data.

While NGC 3621 is classified as an unbarred galaxy, it is unclear which models will form bars a priori. Therefore we selected three models with different disk stability parameters. This selection allows for a brief exploration of the parameter space. These models are called Model-A,B and C and the values for the input parameters

are listed in Table 5.3 and plotted in Fig. 5.1. Model-A has the smallest disk/halo ratio, which should give it the most stability against bar formation. Model B correspond to the peak of the parameters PDFs and Model-C is the least stable. After evolving the model for 5 Gyr, we extract the stellar surface density and gaseous velocity maps for every snapshot. At each time-step we calculated both the bar strength and the standard deviation of the difference between the simulated and observed velocity maps, which are shown in Fig. 5.2. The standard deviation is obtained first by re-centering and re-aligning the model and observe velocity fields using the GIPSY task TRANSFORM. Then a pixel-by-pixel comparison is perform using the GIPSY utility task SUB. Fig. 5.2 shows that model-A has the weakest bar and, at T= 2 Gyr, the lowest standard deviation. Fig. 5.3 shows comparison of this snapshot with the observed maps. It is interesting to note that Model-A is a high stability model, not the model found at the peak of the parameter PDFs. This results emphasizes the importance of running numerical simulations as the Bayesian PDFs include model that rapidly form moderate bars. While these initial conditions are acceptable for the axisymmetric Bayesian analysis, they must be rejected based on the simulations.

Fig. 5.4 shows a comparison of the ROTCUR RC with the THINGS model RCs and the expected RC calculated from the best fitting snapshot. These RCs are all consistent with the ROTCUR RC. Interestingly, the simulated RC seems to fit the inner 5 kpc slightly better than the THINGS RCs.

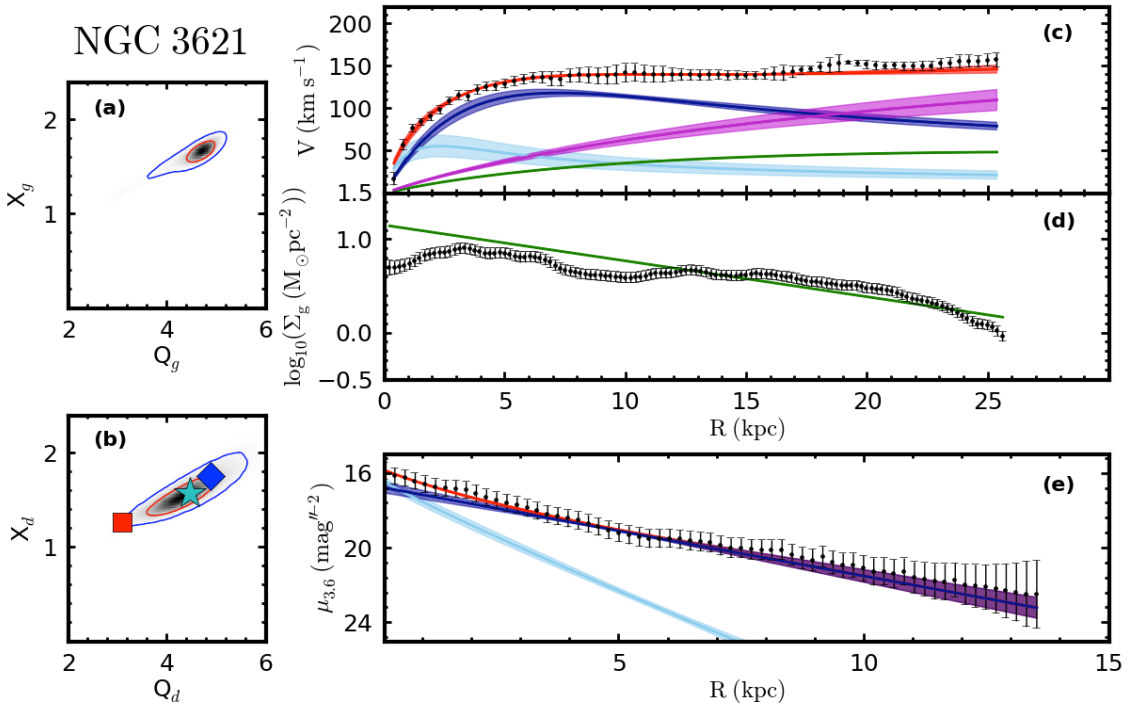

FIGURE 5.1: The PDFs of the disk stability parameters, Q and X, are shown in the left panels. The upper left panel is for the gas disk (*a*), while the lower left panel (*b*) is for the stellar disk. The stability parameters for the selected models are plotted on top of panel (*b*) where Model-A is shown as blue diamond, Model-B as cyan star and Model-C as red square. The right panels shows the PDFs of the RCs on top (*c*), the gas surface density on the middle panel (*d*) and the 3.6 μ surface brightness profile on the bottom panel (*e*). The best fit to the data is shown as red lines, the stellar disk is shown as dark blue, the green lines are the gas disk contribution, the magenta line is the halo contribution and the light blue lines are the bulge component. The shaded area shows the 1-sigma error and the data are shown as black points.

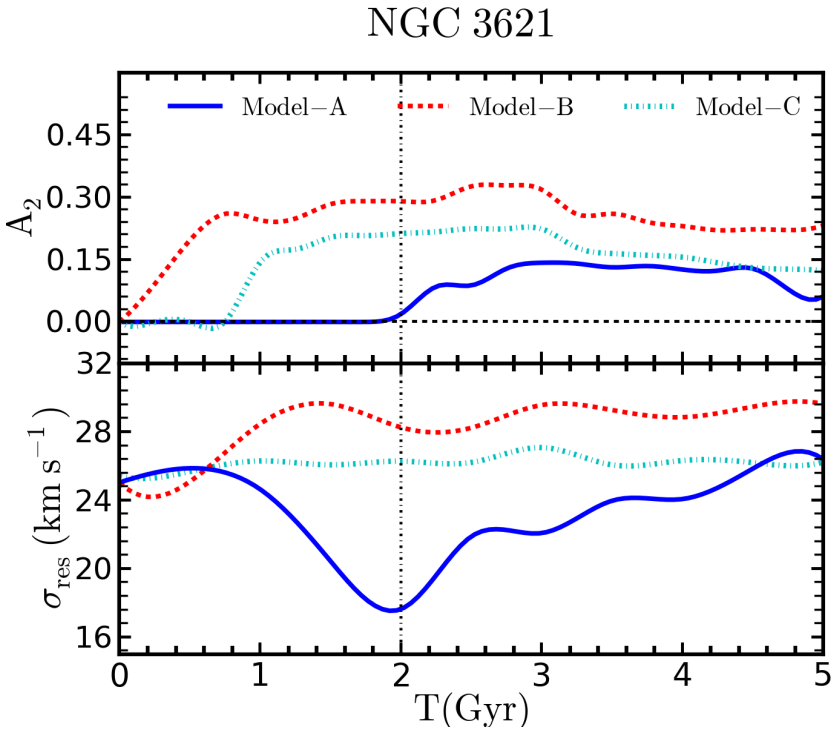

FIGURE 5.2: The variation of the bar strength A_2 (top) and the standard deviation of the difference between the observed and the modeled velocity field σ_{res} (bottom) as function of the epoch. The horizontal dashed line is the expected A_2 and and the vertical dashed line indicate the epoch of the selected snapshot.

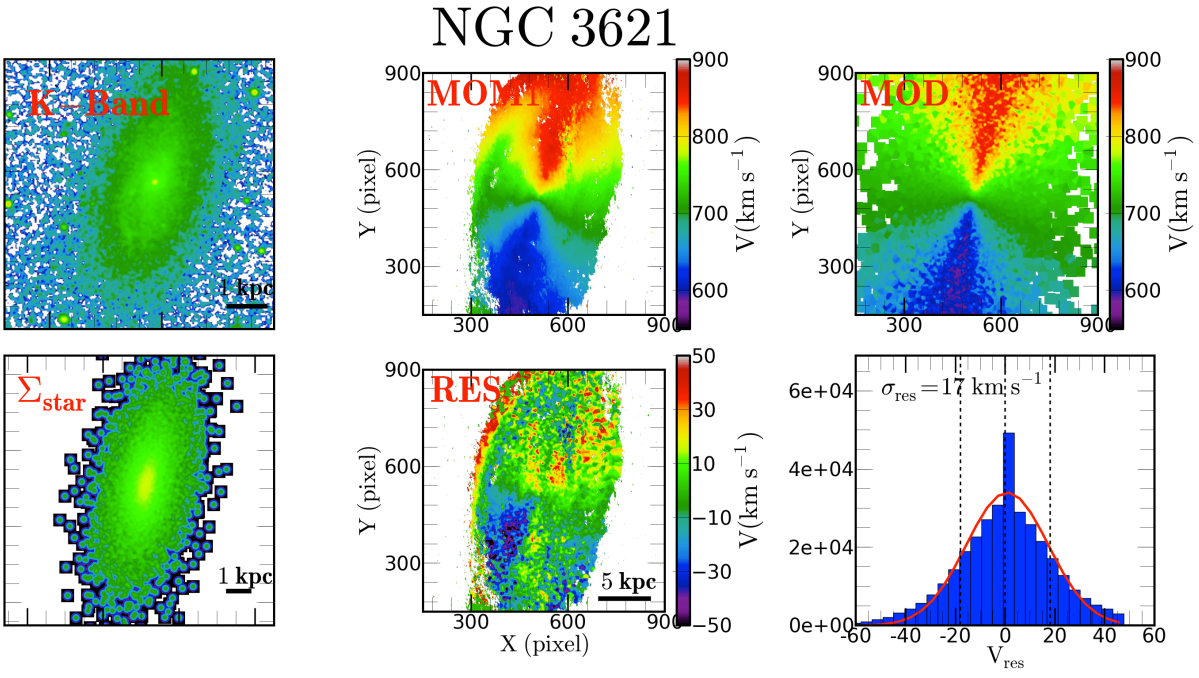

FIGURE 5.3: Model-A at T=2 Gyr, the optical K-band image from Jarrett et al. (2003) is compared with the stellar density on the first column, the second column shows the moment1 map on top and the residual map on the bottom panel. The last column displays the model velocity field on the top panel of and the histogram of the residual on the bottom panel, where the dotted vertical lines are the mean and standard deviation, the red curve is the best fit.

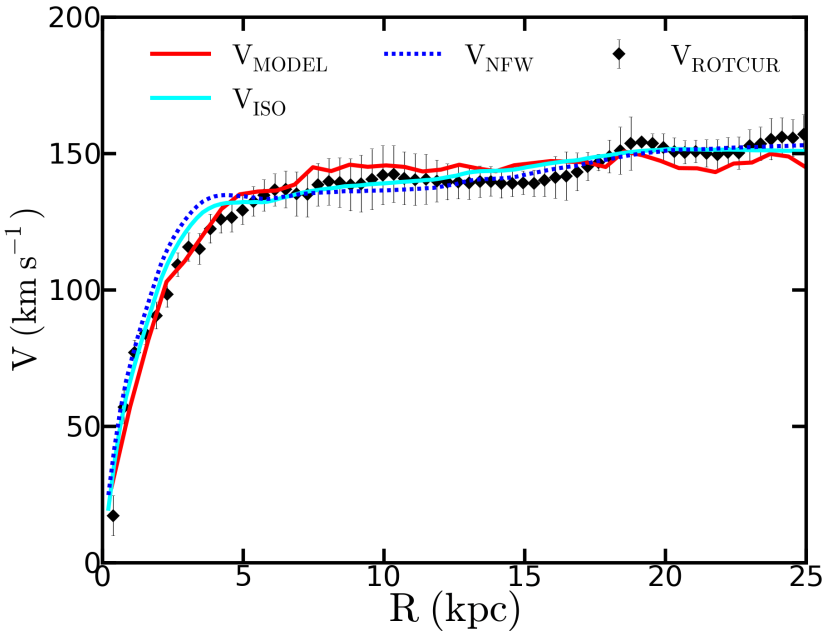

FIGURE 5.4: Comparison between the observed RC, the RC calculated from the gravitational potential with the ISO and NFW mass model results from (de Blok et al. 2008) for the NGC3621-A at T = 2.0 Gyr.

5.4.2 NGC 1530 model

NGC 1530 provides an excellent test case for comparing our method with DiskFit as it has a strong bar at an intermediate angle. The best fit results from the initial Bayesian analysis are presented in Table 5.4 while Fig. 5.5 shows the model stability and the comparison to the observations. In this case we avoid the barred regions of the galaxy for the Bayesian analysis in the RC and surface density fits while we avoid the outer regions of the 3.6 μm surface profile due to possible contamination.

As with NGC 3621, we simulated three models that represent the parameter space namely Model-A,B and C. These models correspond to low and high disk stabilities (model-A and C) and the peak of the parameter PDFs (model-B). The initial conditions for the simulation are listed in Table 5.4. We analyzed each snapshot, comparing both the bar strength and standard deviation of the velocity residuals for each model, which is shown in Fig. 5.6. We then select the model and snapshot that not only reproduce the bar strength but also has the lowest standard deviation of the residual. The evolution of the bar strength and residuals shown in Figure 6 demonstrates a number of interesting points. Model-C shows rapid bar growth until it buckles at T $\sim$ 0.8 Gyr and decreases to a constant value. Interestingly the minima of Model B does not occur when it has the correct bar strength. On the other hand, Model A never grows a bar that is as strong as the observed bar of NGC 1530. Only Model-B has a minima when it matches the bar strength. However, this minima is the global minima so we compare the snapshot of Model-B at T=2.4 Gyr to the observations. This corresponds to a standard deviation of $\sim$15 km/s.

Fig. 5.7 shows the comparison of this snapshot to observations of the system. In this case, the largest residuals occur in the middle of the disk, near holes in the observed velocity maps. This may be due to our simulation not quite matching the spiral structure present in the galaxy.

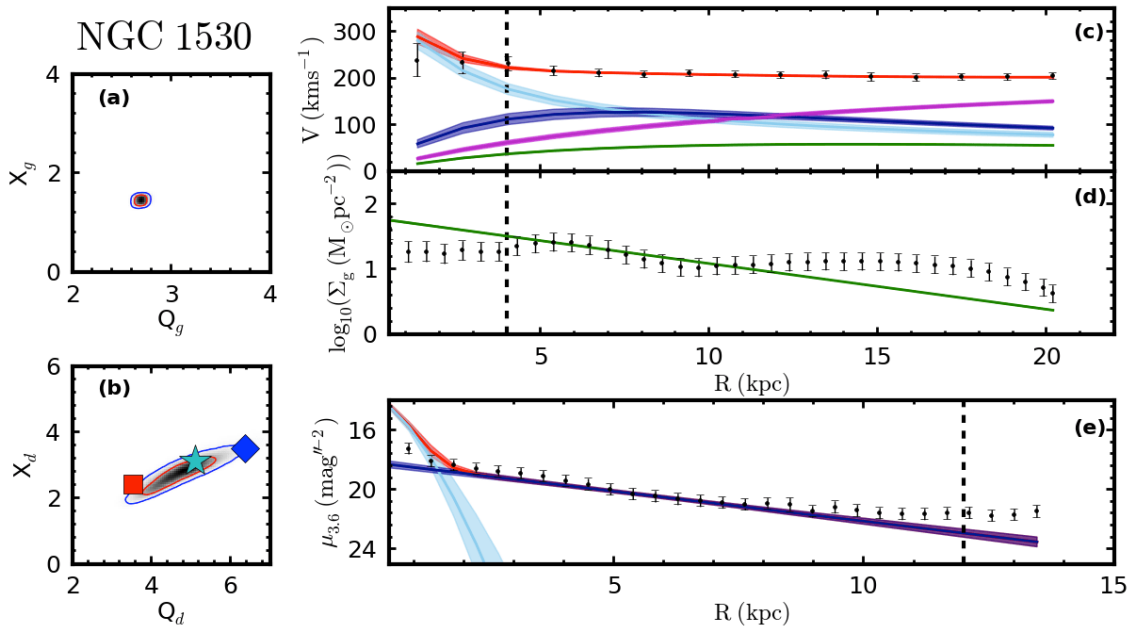

FIGURE 5.5: Same as in Fig. 5.1 but for NGC 1530. The vertical dashed lines indicate regions that are excluded from our analysis due to the presence of the bar (RC and gas SD) or possible contamination (surface brightness).

Figure 5.8 shows a DiskFit model result of the same velocity map. The residuals from this fit are smaller than our method with a standard deviation of 9 km/s. This is unsurprising as DiskFit is explicitly designed to match velocity maps. However, our standard deviation is not too much larger and, as shown in the lower left panel, our inferred RC and non-axisymmetric motions agree with those obtained by the DiskFit analysis. While DiskFit is better at reproducing the velocity maps for NGC 1530, our results are comparable. Moreover, we can apply our method to galaxies like NGC 1300 and our method returns a full mass model as well as non-circular motions.

5.4.3 NGC 1300 model

NGC 1300 is the perfect galaxy for this method of tailored numerical simulations. It has a strong bar aligned with the major axis, which means that ROTCUR will underestimate the RC of this galaxy (see Randriamampandry et al. 2016) and,

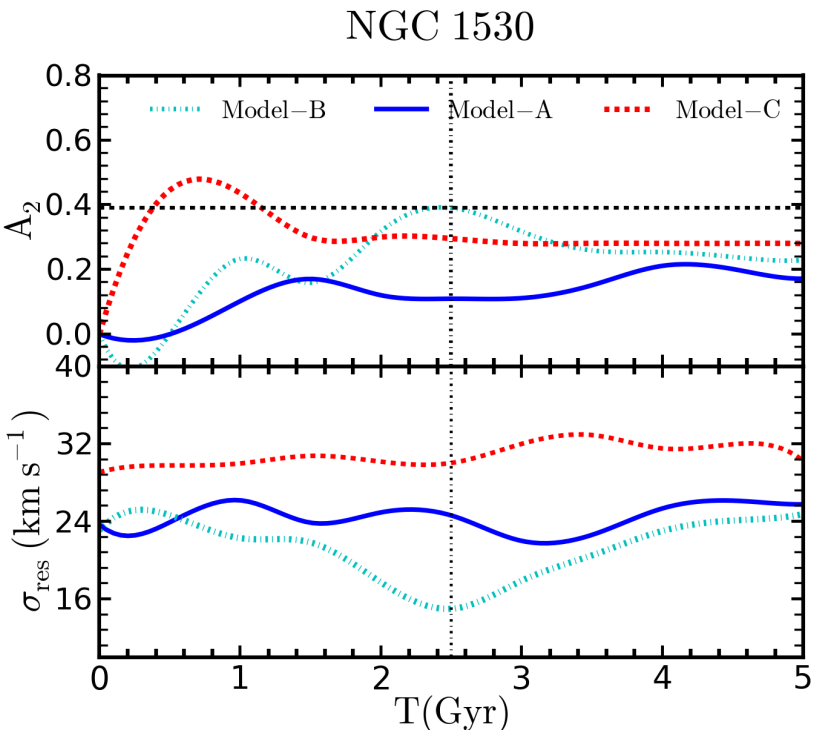

FIGURE 5.6: Same as Fig 5.2. The dashed horizontal line is the A_2 from Aguerri et al. (1998). The vertical dashed line indicates the location of the selected snapshot.

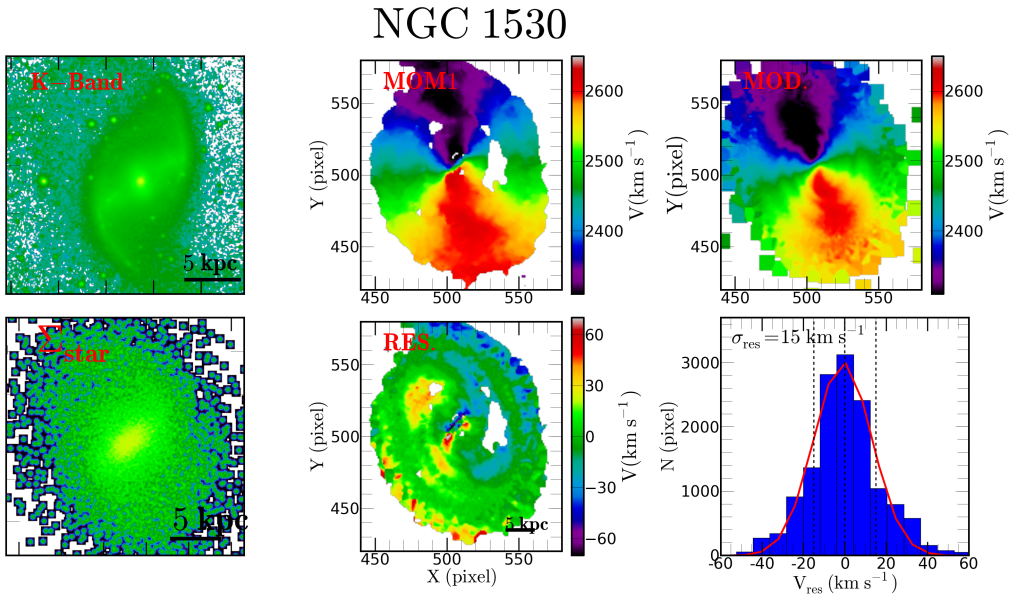

FIGURE 5.7: The panels are the same as in Fig. 5.7, the optical K-band image is taken from Regan et al. (1995).

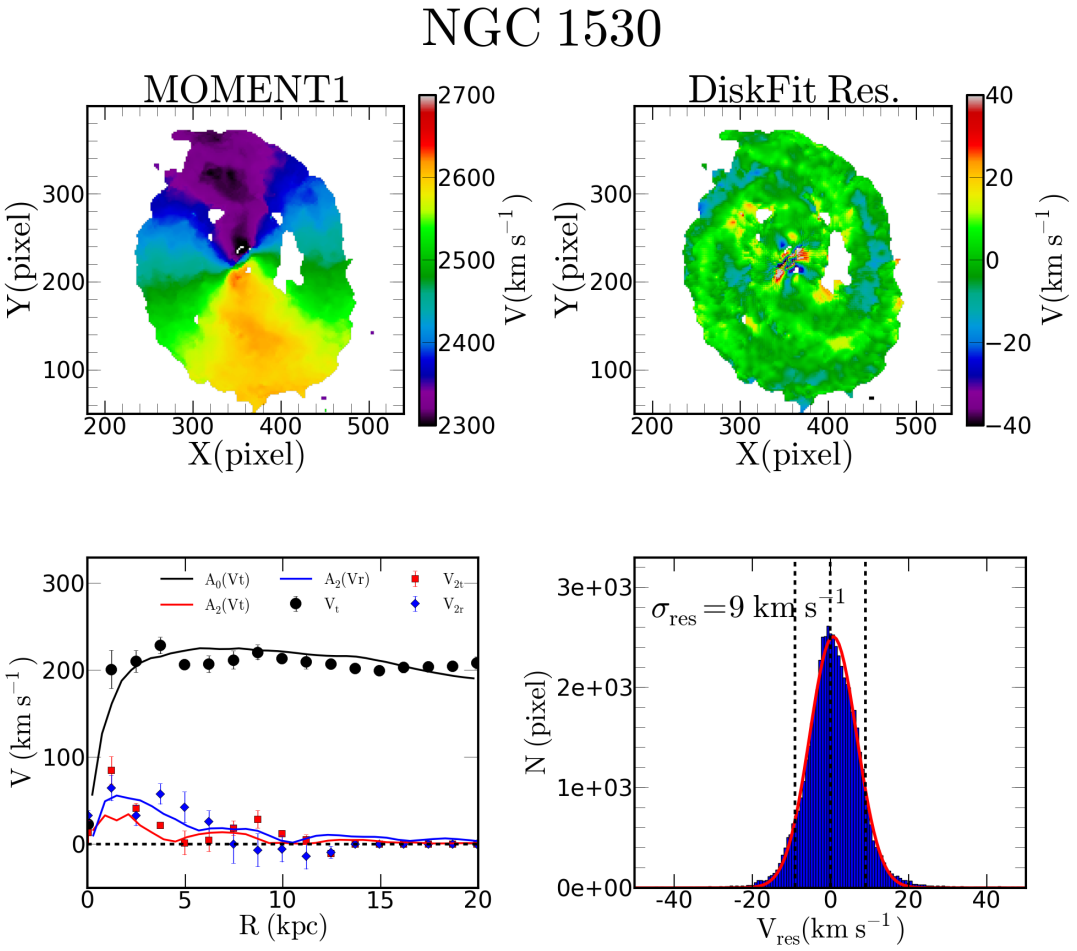

FIGURE 5.8: DiskFit results for NGC1530. The moment1 map is on the top left panel and the residual map is displayed on the top right panel. A histogram of the residual is presented on the bottom right panel and a comparison between V_t, V_{2t} and V_{2r} with the amplitude of the m=0 and m=2 Fourier mode A_0 and A_2 on the left panel.

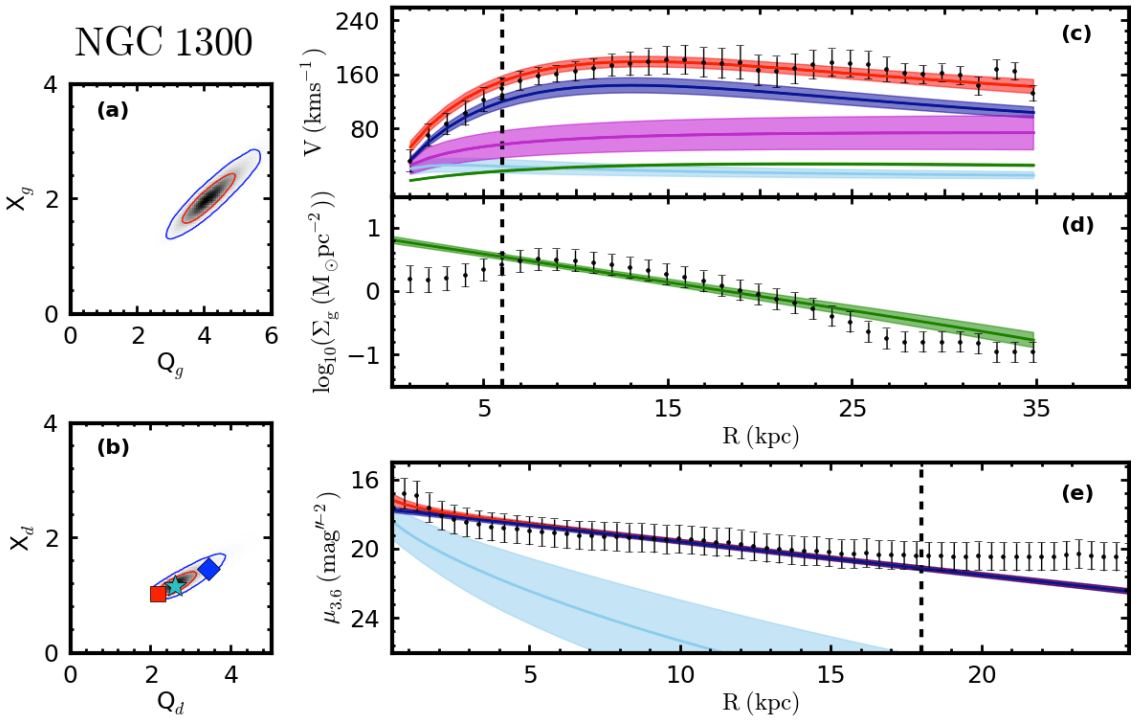

FIGURE 5.9: Same as in Fig. 5.1, the vertical dashed delineate the part of data used in the fit.

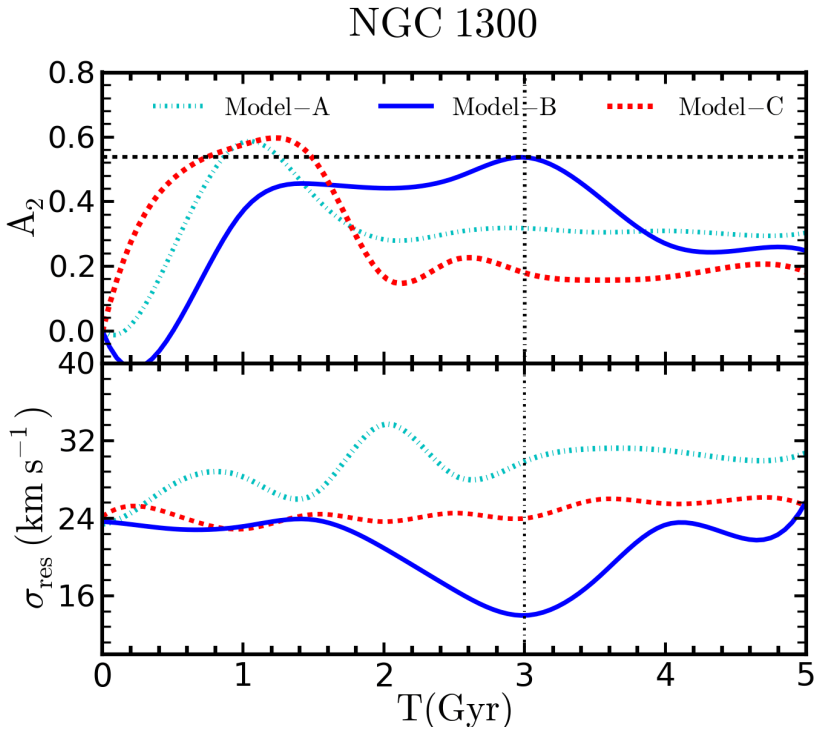

FIGURE 5.10: Same as Fig 5.2. The dashed horizontal line is the A_2 from Díaz-García et al. (2016). The vertical dashed line indicates the location of the selected snapshot.

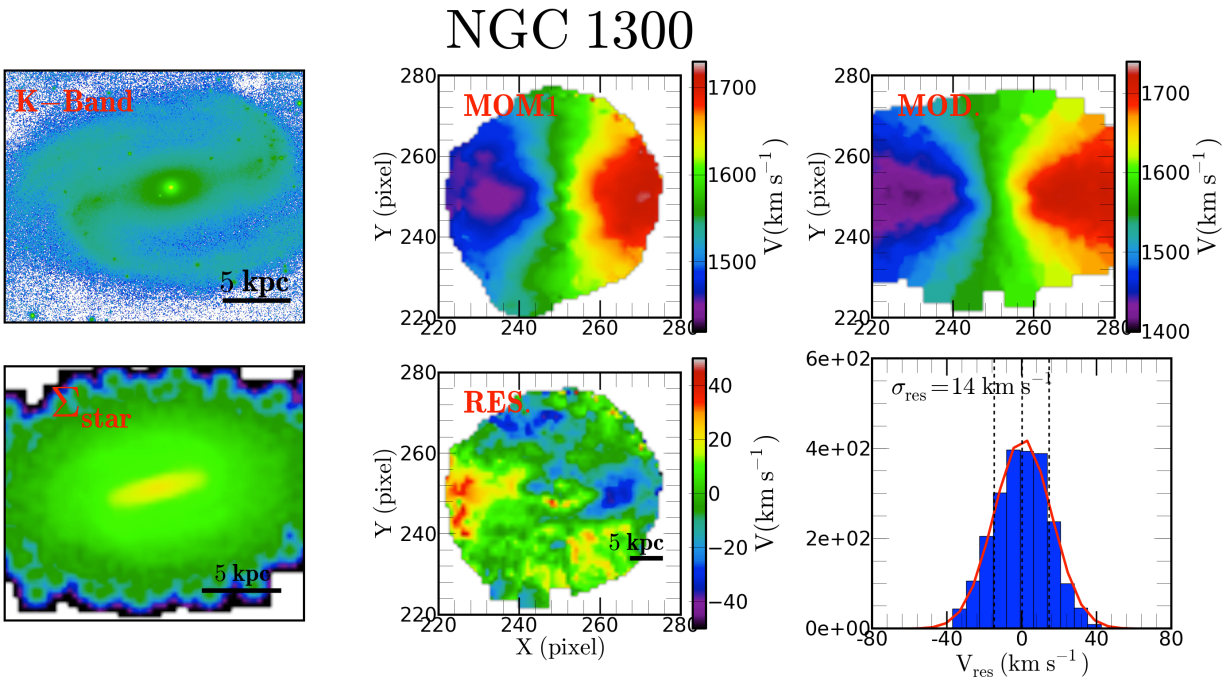

FIGURE 5.11: The optical K-band image is taken from Jarrett et al. (2003). The panels are the same as in Fig. 5.7.

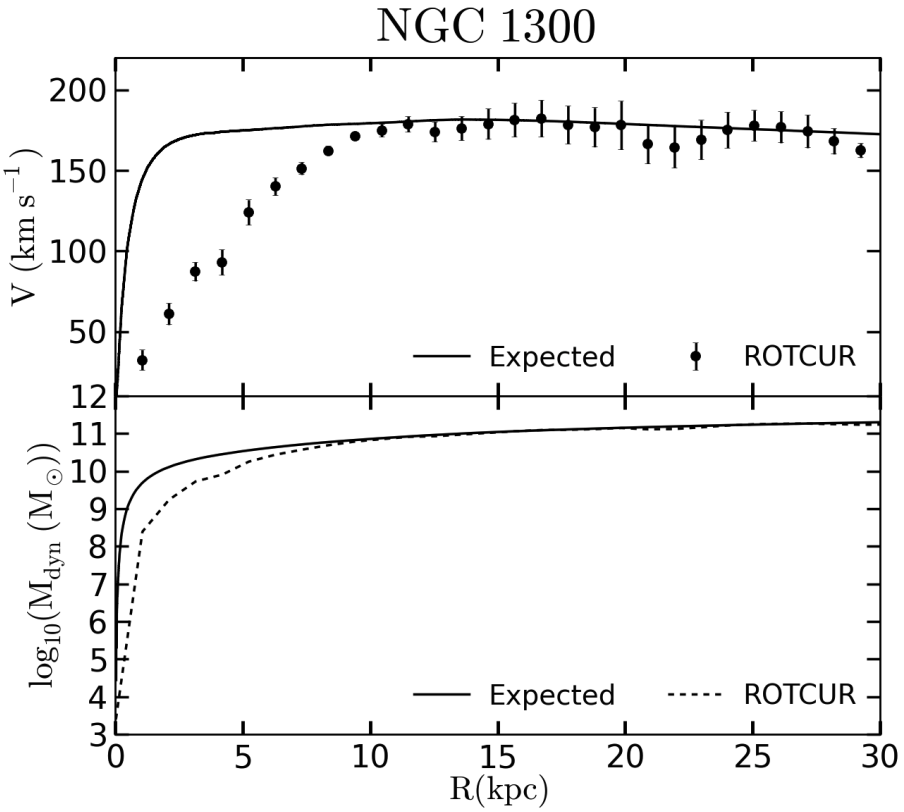

FIGURE 5.12: Mass profile of NGC 1300: the rotation curve measured with ROTCUR is compared with the expected velocities from the gravitational force. The mass profile inferred from the ROTCUR RC and the expected mass from the snapshot are presented on the bottom panel.

due to degeneracies in the fitting formula, DiskFit will fail (Sellwood & Sánchez 2010).

As with the other galaxies, we begin with a Bayesian analysis of the RC, 3.6 micron surface brightness, and surface density. To avoid complications due to the bar, we exclude data from the RC and the gas surface density from the inner 6 kpc. The best fit parameters are given in Table 5.5. The stability PDFs and observation comparisons are shown in Fig. 5.9. This analysis suggests that NGC 1300 has a halo that is more cuspy than cored.

Following our general methodology, the input parameters for the three model namely Model-A, B and C are selected based on their disk stability and listed in Table 5.5. We examine the snapshots from our simulations that have the same bar strength as reported in Díaz-García et al. (2016) and the minimum residual velocity standard deviation. Fig. 5.10 shows that each of the simulations reach the desired bar strength over different time scales. However, when Model B reaches the target bar strength at T=3 Gyr it also has the smallest residual standard deviation. The comparison of the best-fitting snapshot to the actual observations is shown in Fig. 5.11. We measured a standard deviation $\sigma_{res} \sim 14$ km/s for the selected snapshot. It is clear from the velocity maps shown in Fig. 5.11 that there are still some discrepancies between our model and the actual galaxy. Resolving these discrepancies will require both better data and more simulations. Nonetheless, it is also clear that our methodology can be applied to bars that are parallel/perpendicular to the major axis of the galaxy. And, for the first time, we have produced one of the first mass models for NGC 1300. To illustrate the strength of our method, we compared the RC derived by ROTCUR to the expected RC from the simulation. As shown in the upper panel of Fig. 5.12, there is a significant difference between these two RCs, with the ROTCUR curve underestimating the velocity in the inner 10 kpc. The lower panel of Fig. 5.12 shows the mass profile inferred from the ROTCUR RC compared to the true mass profile of the galaxy. There is a significant difference between these two mass profiles, which

will lead to radically different inferences of the DM content of NGC 1300. This galaxy has a much more concentrated mass profile than what is inferred from the ROTCUR RC.

5.5 Summary and Conclusions

We have presented a new method to study the mass distribution of strongly barred galaxies using numerical simulations. An initial Bayesian analysis is performed on the azimuthally averaged RC, 3.6 μm surface brightness, and gas surface density. The PDFs from the Bayesian analysis are combined with an examination of the resulting disk stability to determine the initial conditions.

The N-body systems are initialized using a new version of the GalactICS code (Widrow et al. 2008; Deg et al. 2017) and evolved for 5 Gyrs using the GADGET-2 code (Springel 2005). The best fitting snapshot is found by comparing the bar properties and velocity maps of the simulation to observations of the galaxy..

We applied this algorithm to NGC 3621, 1530, and 1300. For NGC 3621 we found that our model is consistent with the ISO and NFW results from de Blok et al. (2008). It also reproduces the overall shape of the observed RC especially in the inner 5 kpc of the RC. Our result showed that the peak of the parameter PDFs does not always reproduce the actual galaxy. This is why simulations are necessary in addition to the Bayesian analysis. The Bayesian analysis allows us to find plausible axisymmetric models to use for the simulation initial conditions. But it is the simulations that tell us whether those models will produce bars and 2D velocity maps like those observed.

We were able to reproduce the bar strength from Aguerri et al. (1998) and the major kinematic structure of NGC 1530. DiskFit does provide a better fit to the velocity map, but our azimuthally averaged velocities as well as the radial and tangential velocity moments agree with the results from DiskFit. DiskFit is

clearly the better choice for modeling galaxies with intermediately oriented bars. However, our method still recovers the overall mass profile and can be applied to galaxies like NGC 1300.

Since NGC 1300 is a strongly barred galaxy where the bar is parallel to its position angle, algorithms like DiskFit cannot recover the RC from the velocity map (Sellwood & Sánchez 2010; Randriamampandry et al. 2016). Similarly, ROTCUR underestimates the RC for galaxies with such a bar orientation (Randriamampandry et al. 2015). Our method is not subject to these same restrictions. We have produced one of the first mass models of NGC 1300 and find that the DM halo is more cuspy than cored.

Tailored simulations provide an effective method of investigating non-axisymmetric flows in disc galaxies. They can be used to model galaxies where other algorithms fail and give greater information on the structure of the galaxy than velocity modeling. In the future we plan on extending this method to utilize data cubes rather than velocity maps. We also plan on running grids of simulations rather than individual runs in order to test the uniqueness of our solutions. Nonetheless, this method allows us to investigate a greater variety of galaxies than ever before, which can only help improve our understanding of galactic bars, non-circular flows, and galaxy evolution.

Acknowledgments

CC's work is based upon research supported by the South African Research Chairs Initiative (SARChI) of the Department of Science and Technology (DST), the SKA SA and the National Research Foundation (NRF). ND and TR's work is supported by a SARChI's South African SKA Fellowship. We thank Dr Kristine Spekkens for the discussions. We would also like to acknowledge the Center for high Performance Computing (CHPC) and its staff, in particular Dr. Sean February and Prof. Catherine Cress for allowing us to use this facility under the program ASTR0858.

Bibliography

Aguerri, J. A. L., Beckman, J. E., & Prieto, M. 1998, AJ, 116, 2136

Aguerri, J. A. L., Muñoz-Tuñón, C., Varela, A. M., & Prieto, M. 2000, A&A, 361, 841

Aguerri, J. A. L., Méndez-Abreu, J., & Corsini, E. M. 2009, A&A, 495, 491

Begeman K. G., 1989, A&A, 223, 47

Chequers, M. H., Spekkens, K., Widrow, L. M., & Gilhuly, C. 2016, MNRAS,

Condon, J. J., Helou, G., Sanders, D. B., & Soifer, B. T. 1996, ApJS, 103, 81

de Blok W. J. G., Walter F., Brinks E., Trachternach C., Oh S.-H., Kennicutt, Jr. R. C., 2008, AJ, 136, 2648

Deg, N., Widrow, L, Randriamampandry, T. H., & Carignan, C., 2017 in prep

Díaz-García, S., Salo, H., Laurikainen, E., & Herrera-Endoqui, M. 2016, A&A, 587, A160

Dicaire, I., Carignan, C., Amram, P., et al. 2008, MNRAS, 385, 553

England, M. N. 1989, ApJ, 337, 191

Freedman, W. L., Madore, B. F., Gibson, B. K., et al. 2001, ApJ, 553, 47

Foreman-Mackey, D., Hogg, D. W., Lang, D., & Goodman, J. 2013, PASP, 125, 306

Gentile, G., Famaey, B., & de Blok, W. J. G. 2011, A&A, 527, A76

Goldreich, P., & Tremaine, S. 1978, ApJ, 222, 850

Goldreich, P., & Tremaine, S. 1979, ApJ, 233, 857

Jarrett, T. H., Chester, T., Cutri, R., Schneider, S. E., & Huchra, J. P. 2003, AJ, 125, 525

Laurikainen, E., Salo, H., & Buta, R. 2004, ApJ, 607, 103

Lindblad, P. A. B., Kristen, H., Joersaeter, S., & Hoegbom, J. 1997, A&A, 317, 36

Toomre, A. 1964, ApJ, 139, 1217

Menéndez-Delmestre, K., Sheth, K., Schinnerer, E., Jarrett, T. H., & Scoville, N. Z. 2007, ApJ, 657, 790

Oh, S.-H., de Blok, W. J. G., Walter, F., Brinks, E., & Kennicutt, R. C., Jr. 2008, AJ, 136, 2761-2781

Prugniel, P., & Simien, F. 1997, A&A, 321, 111

Puglielli, D., Widrow, L. M., & Courteau, S. 2010, ApJ, 715, 1152

Randriamampandry, T. H., Combes, F., Carignan, C., & Deg, N. 2015, MNRAS, 454, 3743

Randriamampandry, T. H., Deg, N., Carignan, C., Combes, F., & Spekkens, K. 2016, A&A, 594, A86

Regan, M. W., Vogel, S. N., & Teuben, P. J. 1995, ApJ, 449, 576

Rogstad, D. H., Lockhart, I. A., & Wright, M. C. H. 1974, ApJ, 193, 309

Sellwood, J. A., & Sánchez, R. Z. 2010, MNRAS, 404, 1733

Spekkens, K., & Sellwood, J. A. 2007, ApJ, 664, 204

Springel, V. 2005, MNRAS, 364, 1105

Wang, H.-H., Klessen, R. S., Dullemond, C. P., van den Bosch, F. C., & Fuchs, B. 2010, MNRAS, 407, 705

Walter, F., Brinks, E., de Blok, W. J. G., et al. 2008, AJ, 136, 2563-2647

Widrow L. M., Pym B., Dubinski J., 2008, ApJ, 679, 1239

van der Kruit, P. C., & Searle, L. 1981, A&A, 95, 105

A PDF of the model parameters

The one and two dimensional PDFs for nine of the free parameters are shown in Figs. A1, A2 and A3 for NGC 3621, NGC 1530 and NGC 1300 respectively. We do not show the scale heights for the stellar and gas disks, as the stellar scale height is poorly constrained, and the GalactICS gas disk has a varying scale height determined by the kinematic gas temperature. These figures show that the gas parameters are more tightly constrained than the bulge, disk, and halo parameters. There are a number of correlations apparent between the parameters. Galaxies with larger sigma prefer smaller alpha and larger beta. Additionally, there is a correlation between σ_h and M_d that shows the classic disk-halo degeneracy.

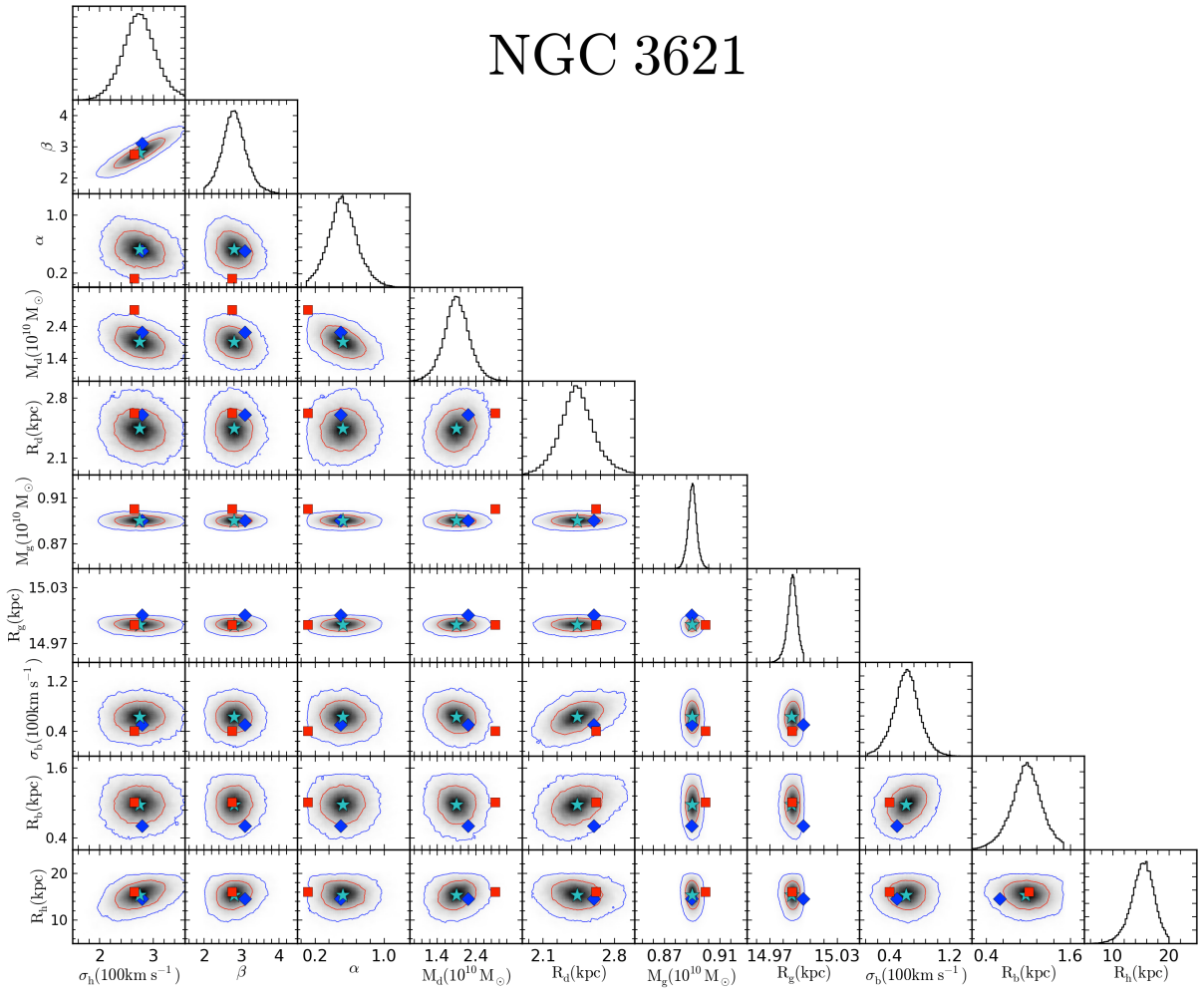

FIGURE A1: Two-dimensional and one-dimensional PDFs of the model parameter for NGC 3621: the two-dimensional PDFs are shown on the lower triangular of the matrix and the one-dimensional PDFs on the principal diagonals. The red and blue contour in each panel delineates the 68% and 95% confidence levels. The cyan stars correspond to Model-C, the blue diamonds to Model-A and the red square to Model-B.

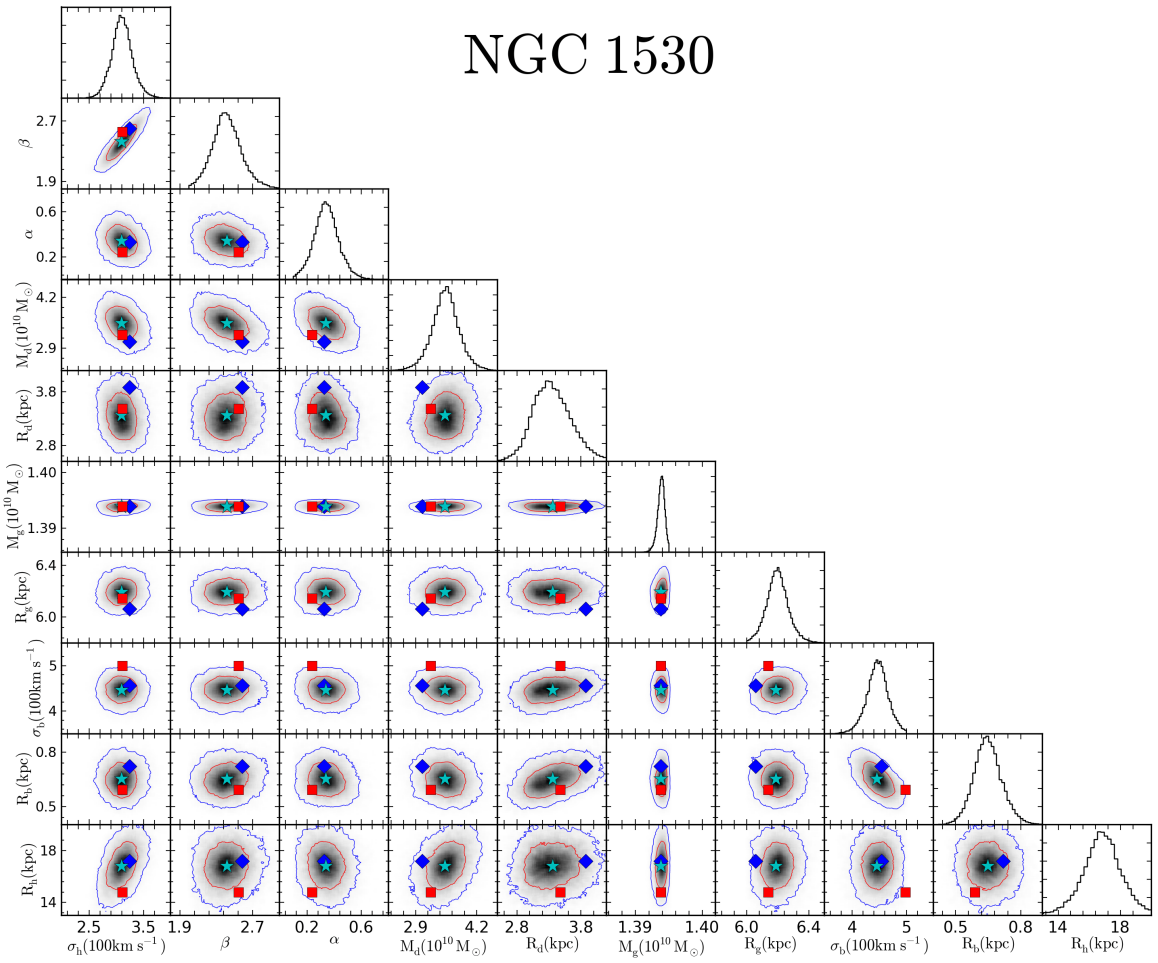

FIGURE A2: Two-dimensional and one-dimensional PDFs of the model parameter for NGC 1530. Lines and symbols are the same as in Fig. A1.

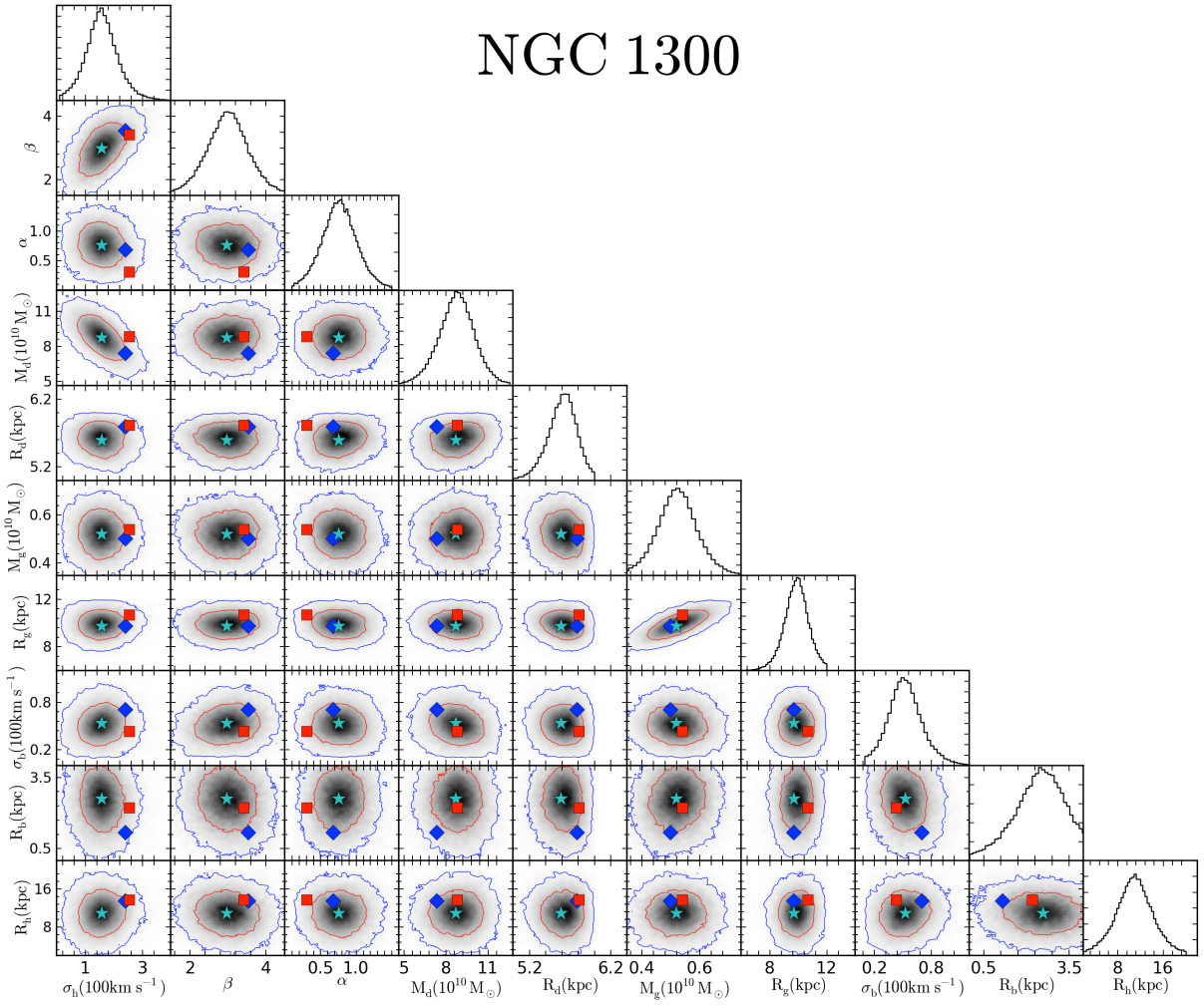

FIGURE A3: Two-dimensional and one-dimensional PDFs of the model parameter for NGC 1300. Lines and symbols are the same as in Fig. A1

Chapter 6

General summary and future work

We have presented a method to correct the rotation curves of nearby barred spiral galaxies from the non-circular motions induced by a bar. Rotation curves are used to infer the mass distribution of the luminous and dark matter content of disk galaxies. This is accomplished by comparing the observed rotation curve to the quadratic sum of the different components of the galaxy: the stars, gas and dark matter halo (de Blok et al. 2008) and by assuming that the gas is moving in circular orbit and that the galaxy is axisymmetric. While this is largely the case, part of the observed velocities may be due to noncircular motions such as those induced by the presence of bars. The so-called tilted ring method (Rogstad et al. 1974) is commonly used when deriving rotation curves of galaxies. However, this method does not correct for non-circular motions. The GIPSY task RESWRI uses higher harmonics to estimate the magnitude of the non-circular motions (Schoenmakers et al. 1997). While this method addresses the issue to some extent, it is limited to galaxies with small scale deviations from circular motions. (Spekkens & Sellwood 2007) created a new tool called DiskFit to correct for large scale on-circular motions such as those induced by bars.

However, previous studies (e.g. Sellwood & Sánchez 2010; Randriamampandry et al. 2015, 2016) have shown that DiskFit is restricted by the orientation of bar. We used the results of numerical simulations to investigate and quantify the non-circular motions. We also tested current methods that are used to estimate the bar properties and to derive rotation curves. We tested the limitation of the DiskFit algorithm, which is designed specifically for barred galaxies.

In chapter II, we have use SPH/N-body simulations to estimate the effect of the bar orientation on the derived rotation curves. Our results show that the tilted ring method implemented in ROTCUR overestimates/underestimates the rotation curve when the bar is perpendicular/parallel with the minor/major axis of the disk. This is because when the bar is aligned closely with the major axis, we find gas and stars preferentially at the apocentres of their elliptical orbits at each radius near the major axis. Most of the gas follow elliptical orbit, which drive the model since the line-of-sight velocities and ring widths are larger, therefore, moves more slowly than it would if it were moving in circular orbits. This leads to an under-estimation of the rotation curve if not taken into account. Conversely, bars that project along the minor axis place gas and stars close to the pericenter along the major axis, which implies that the RC will be over-estimated if bar-like flows are ignored (see Spekkens & Sellwood 2007).

In chapter III, we use all the galaxy types from the GalMer database (Chilingarian et al. 2010) to characterize and quantify the non-circular motions, and compare the bar properties and non-circular motions derived from the simulations with those from mock observations. We also tested ROTCUR and DiskFit using mock velocity fields obtained from the GalMer database. We found that ROTCUR systematically under/over-estimates the inner part of the rotation curve if the bar is parallel/perpendicular to the major axis. The rotation curve errors produced by ROTCUR go up to 40% of the circular velocity for some cases. We found also that DiskFit fails when the bar is oriented less than 10 degrees from the major/minor axes.

In Chapter IV, we performed tailored simulations of NGC 3621, NGC 1530 and NGC 1300 and compared the results with observations. Our objective was to create more realistic simulated galaxies that replicate the bar properties and velocity fields of these three galaxies. The initial conditions were determined through a Bayesian analysis of the azimuthally averaged rotation curve, the stellar surface brightness, and the gas surface density. We used the probability distribution functions of the model parameters combined with the stability parameters as the criterion to select our models. The velocities of the gas particles were transformed into velocity maps and compared with the observed galaxies. We were able to reproduce the bar properties and kinematics of the NGC 3621, NGC 1530 and NGC 1300. The NGC 3621 results are compared to those of de Blok et al. (2008). We found that DiskFit is the preferred software to derive the rotation curve of NGC 1530, which hosts a bar that is oriented at an intermediate angle between the major and minor axes. The simulation was then used to construct a mass model for NGC 1300, since it host a bar that is parallel to the major axis, which cannot be handled by DiskFit.. We were able to produce a mass model of NGC 1300 that represents the true gravitational potential. This result shows that a tailored simulation is an effective way of investigating non-circular flows and deriving the mass models of barred galaxies when the bar is aligned with one of the symmetry axes.

As for future work, we will be running a series of simulations of galaxies spanning a wide range of morphological types and masses. This will help us test our method and the uniqueness of the solutions. We will investigate the effect of spatial and velocity resolutions of the data on the results. We will compare the data-cube directly with the model instead of velocity maps and explore global correlations between the non-circular motions and the spatial resolution and the sensitivity by varying the number of particles and changing the pixel scale when mock-observing the simulated data. Our ultimate goal is to derive a grid of corrections which can be used for future observations and implemented in software packages dedicated

to rotation curve analyses of large samples, as those that will be produced by MeerKAT and, subsequently, by the SKA..

Bibliography

Begeman, K. G. 1989, A&A, 223, 47

Bosma, A. 1981, AJ, 86, 1825

Carignan, C., & Freeman, K. C. 1985, ApJ, 294, 494

Carignan, C., Frank, B. S., Hess, K. M., et al. 2013, AJ, 146, 48

Carignan, C., Libert, Y., Lucero, D. M., et al. 2016, A&A, 587, L3

Chilingarian, I. V., Di Matteo, P., Combes, F., Melchior, A.-L., & Semelin, B. 2010, A&A, 518, A61

de Blok, W. J. G., McGaugh, S. S., Bosma, A., & Rubin, V. C. 2001, ApJL, 552, L23

de Blok, W. J. G., Walter, F., Brinks, E., et al. 2008, AJ, 136, 2648-2719

Dicaire, I., Carignan, C., Amram, P., et al. 2008, MNRAS, 385, 553

Epinat, B., Amram, P., Marcelin, M., et al. 2008, MNRAS, 388, 500

Heald, G., de Blok, W. J. G., Lucero, D., et al. 2016, arXiv:1607.03365

Lucero, D. M., Carignan, C., Elson, E. C., et al. 2015, MNRAS, 450, 3935

Navarro, J. F., Frenk, C. S., & White, S. D. M. 1996, ApJ, 462, 563

Randriamampandry, T. H., & Carignan, C. 2014, MNRAS, 439, 2132

Randriamampandry, T. H., Combes, F., Carignan, C., & Deg, N. 2015, MNRAS, 454, 3743

Randriamampandry, T. H., Deg, N., Carignan, C., Combes, F., & Spekkens, K. 2016, A&A, 594, A86

Rogstad, D. H., Lockhart, I. A., & Wright, M. C. H. 1974, ApJ, 193, 309

Schoenmakers, R. H. M., Franx, M., & de Zeeuw, P. T. 1997, MNRAS, 292, 349

Sellwood, J. A., & Sánchez, R. Z. 2010, MNRAS, 404, 1733

Spekkens, K., & Sellwood, J. A. 2007, ApJ, 664, 204